2015

GEOMETRY INDUCED MAGNETO-OPTIC EFFECTS IN LPE GROWN MAGNETIC GARNET FILMS

Ashim Chakravarty
Michigan Technological University

GEOMETRY INDUCED MAGNETO-OPTIC EFFECTS IN LPE GROWN MAGNETIC GARNET FILMS

By

Ashim Chakravarty

A DISSERTATION

Submitted in partial fulfillment of the requirements for the degree of

DOCTOR OF PHILOSOPHY

In Engineering Physics

MICHIGAN TECHNOLOGICAL UNIVERSITY

2015

This dissertation has been approved in partial fulfillment of the requirements for the Degree of DOCTOR OF PHILOSOPHY in Engineering Physics.

Department of Physics

Dissertation Advisor:	*Dr. Miguel Levy*
Committee Member:	*Dr. Yoke Khin Yap*
Committee Member:	*Dr. Jae Yong Suh*
Committee Member:	*Dr. Durdu O. Guney*
Department Chair:	*Dr. Ravindra Pandey*

To My Mother

Table of Contents

List of Figures ..... **vi**

List of Tables ..... **xii**

Preface ..... **xiii**

Acknowledgements ..... **xvi**

Abbreviations ..... **xviii**

Abstract ..... **xix**

1. Introduction **1**

1.1. Literature review 1

1.2. Organization of Dissertation 5

2. Magnetic Garnets: Origin of Faraday rotation **6**

2.1. Magnetism in Materials 6

2.2. Crystal Structure of the Garnet Family 8

2.3. Polarized light and the Faraday Effect 11

2.3.1. Polarization of light 12

2.3.2. Magneto-optical Faraday Effect 14

2.3.3. Faraday rotation in YIG and Bi: YIG 16

2.4. Growth and characterization of iron garnet film 20

2.4.1. Liquid phase epitaxy (LPE) 20

2.4.2. Film characterization 21

3. Optical Waveguides and Bragg-Gratings **24**

3.1. Properties of Optical Waveguide 24

3.1.1. Waveguide Modes 25

3.1.2. Dispersion of modes in Asymmetric Waveguide 29

3.1.3. Mode and thickness measurement 30

3.2. Bragg-Gratings on Ridge Waveguide 31

3.2.1. Mode Coupling due to Dielectric Perturbation 33

3.2.2. Photonic Bandgap and Stop-band 35

3.3. Direct end coupling – Mode Excitation 37

4. Magneto-Optic Interactions in Ultra-thin Garnet Films **39**

4.1. Instruments and Garnet Thin Film Characterization 40
4.1.1. Ultra- Sensitive FR Measurement Setup 40
4.1.2. Thin and Ultra-Thin Film Preparation 43
4.1.3. Film Thickness Characterization 45
4.1.4. MCD measurement Setup 49
4.2. Measurements on Garnet Films 50
4.2.1. Specific FR from Hysteresis Loop Measurements 50
4.2.2. MCD and Kramers-Kronig Analysis 52
4.2.3. Compositional Analysis: RBS 55
4.2.4. Surface Measurements 58
4.2.5. Micro-Raman Measurements 59
4.2.6. Error Analysis 60
4.3. Theoretical Analysis of Iron Garnet Films 61
5. Magneto-Photonic Waveguide with Bragg Gratings 63
5.1. Theory of Elliptical Birefringent Periodic Medium: Stacked Model 64
5.2. PC Fabrication on the Magneto-Optic Waveguide 72
5.3. Optics for the MPC waveguide characterization 76
5.3.1. Elliptical beam preparation 78
5.4. Stop-Bands of normal modes from 1D MPCs 80
5.4.1. Normal mode response to a ridge waveguide 81
5.4.2. Impact of magnetization reversal on the normal mode stopband 83
5.5. Bloch mode reconfiguration 87
6. Conclusions and Future Work 90
6.1. Conclusion 90
6.2. Future work 91
Reference List 93
Publications & Achievements 100
Appendix 1 101
Appendix 2 108
Appendix 3 110
Appendix 4 114

List of Figures

Figure 2.1 (a) Unit-cell dipole moments in iron garnets form domain structures and (b) an applied magnetic field align these moments for magneto-optic activities in such garnets....8

Figure 2.2 YIG crystal with a black arrow pointing the magnetic moment of the cell. Inset shows spin-down tetrahedral and spin-up octahedral Fe3+ ions (brown) with Y3+ ions (faded blue) in dodecahedron....10

Figure 2.3 Electric field vector end point rotation in the x-y plane and snapshot of its trajectory in frozen time....13

Figure 2.4 (a) 45° and (b) -45° linear and (c) right- and (d) left-circular polarization states of an optical beam....14

Figure 2.5 In Faraday Effect, a linearly polarized input optical wave breaks down into RCP and LCP normal modes inside a lossless magnetized material and propagate with different phase speeds. These normal modes recombine again at the output and produces a rotated linear polarization state....16

Figure 2.6 Spin-orbit coupling between atomic quantum state and orbital angular momentum makes degeneracy lifting $\mathcal{L}z = \pm 1$ with Δ amount of energy to the ground state in (a) paramagnetic transition and by the same reason excited state splits into degenerate states for (b) diamagnetic transition. Faraday rotation is due to the distinctive absorption of RCP (red) or LCP (green) photons which assists for optical transition of electron either from the split ground state to singlet excited ((a) paramagnetic) or from the singlet ground state to the triplet excite state ((b) diamagnetic) in magneto-optic materials....17

Figure 2.7 In paramagnetic transition, spin-orbit split ground state depends on temperature to define the population densities for distinctive RCP and LCP absorption....18

Figure 2.8 Diamagnetic transitions at optical energies 2.6eV and 3.15 eV for tetrahedral and octahedral Bi: YIG crystal sublattices are majorly responsible for the observed magneto-optic effect in Bi: YIG....19

Figure 2.9 Ellipsometer measures sample reflected output elliptical polarization against the input linear polarization to determine certain optical parameters of the garnet films 22
Figure 2.10 RBS measurement uses two detectors to collect the energy spectrum for backscattered He^{2+} ions to determine the composition of a garnet film 23
Figure 3.1 (a) Basic step-index type waveguide with (b) refractive index profile of cladding (air), film and substrate layers for (c) guided wave propagation ...25
Figure 3.2 In different propagation constant regimes (a), (b), (c) and (d), propagation triangles (top), and corresponding mode profiles (middle)of different modes with β0, β1, β1- , β2- propagation constants in the step index type waveguide structure.....28
Figure 3.3 Calculated TE and TM modes for $Bi_{0.8}Gd_{0.2}Lu_2Fe_5O_{12}$ film/ GGG substrate at 1543nm wavelength 30
Figure 3.4 (a) Prism-coupler measures the (b) Intensity dips at various prism angles (θ_p) to determine the modes from a slab waveguide.....31
Figure 3.5 Ridge waveguide schematic.....32
Figure 3.6 Fabrication of ridge waveguide requires optical photolithography steps: (a) sample cleaning (b) photo-resist coating (c) Ultra-Violet ray exposure (d) photo-resist development. Following lithography, dry etching using plasma treatment produces (e) slab film with strip patterns and creates the (f) ridge waveguide structures.....32
Figure 3.7 Bragg gratings on a ridge waveguide structure.....33
Figure 3.8 Brillouin diagrams for (a) guided mode dispersion in a ridge waveguide structure and (b) optical bandgaps due to contra-directional coupling in ridge waveguide with 1D Bragg gratings.....36
Figure 3.9 Optical wave coupling Fiber to a ridge waveguide structure through Direct Coupling Method 37
Figure 4.1 In this ultra-sensitive Faraday-Rotation measurement setup, measured polarization rotation gets amplified 32 times, as the phase between two consecutive wheel grooves has an arc distance of 11.25°, whereas the same

phase is read as 360° by the lock in amplifier. Some of the components are not shown to keep the schematic clear.....41

Figure 4.2 Micro-controller based spin wet etching device used for fabricating thin and ultra-thin garnet films by reducing the thickness of a thicker film.....43

Figure 4.3 Ellipsometric model to determine the thickness of a $Bi_{0.8}Gd_{0.2}Lu_2Fe_5O_{12}$ film on GGG substrate. Film thickness value in this measurement reads 2717.79 ± 0.94 nm.....46

Figure 4.4 $Bi_{0.8}Gd_{0.2}Lu_2Fe_5O_{12}$ film thicknesses: (a) 1884.9 nm (b) 828.8nm (c) 376.7nm (d) 96.5nm, and (e) 31.3nm on GGG substrates measured by reflection ellipsometry method.....47

Figure 4.5 TEM sample is prepared by depositing (a) tungsten pad on targeted sample. FIB mills out (b), (c) a small piece of the sample by (d), (e), (f) engaging a tungsten microprobe and then attached to (g) TEM grid by welding method. Further the vertical walls of the sample are polished in FIB for electron transparency.....48

Figure 4.6 $Bi_{0.8}Gd_{0.2}Lu_2Fe_5O_{12}$ film thicknesses measured using TEM for (a) 23.4nm (b) 146nm and (c) 307nm films, respectively.....48

Figure 4.7 Modified V-Vase ellipsometer setup to produce pure circular polarization states in the wavelength range 260—800nm to perform MCD measurements from $Bi_{0.8}Gd_{0.2}Lu_2Fe_5O_{12}$ films.....49

Figure 4.8 Specific Faraday rotation θ versus film thickness for $Bi_{0.8}Gd_{0.2}Lu_2Fe_5O_{12}$ films (the substrate contribution has been folded out in this data set) at 532nm wavelength. Inset: Faraday rotation hysteresis loops measured on the $Bi_{0.8}Gd_{0.2}Lu_2Fe_5O_{12}$ films for different thicknesses and on the GGG substrate: (1) Substrate, (2) 60nm, (3) 590nm, (4) 1520nm and (5) 2720nm. The magnetic field is expressed in terms of the current in the electromagnet. Reprinted with permission from: ref. [1] Fig.1 51

Figure 4.9 Specific Faraday rotation calculated using ellipsometry-measured film thicknesses (blue curve) and the TEM-measured film thicknesses (red curve) show the same increasing trend with decreasing thickness 51

Figure 4.10 Magnetic circular dichroism on four $Bi_{0.8}Gd_{0.2}Lu_2Fe_5O_{12}$ films of different thicknesses: (A) Experimental results. (B) Theoretical analysis calculated from the permittivity tensors for iron garnets as explained in theoretical section 4.3. The curves correspond to the following film thicknesses: (1) 19nm, (2) 46nm, (3) 95nm, (4) 153nm. Reprinted with permission from: ref. [1] Fig. 2 53

Figure 4.11 The calculated specific Faraday rotation (red curve) at 532 nm from the MCD measurements increases with decreasing film thickness. For the purpose of comparison, the specific Faraday rotation (blue curve) for 200nm $Bi_{0.8}Gd_{0.2}Lu_2Fe_5O_{12}$ film thicknesses measured by ellipsometer is shown ..54

Figure 4.12 The RBS measurement shows a transient layer in between the 340nm thick $Bi_{0.8}Gd_{0.2}Lu_2Fe_5O_{12}$ film and the GGG substrate 56

Figure 4.13 AFM measurements on $Bi_{0.8}Gd_{0.2}Lu_2Fe_5O_{12}$ film of thicknesses (a) 21.6nm (b) 60.1nm (c) 171.8 nm, and on (d) GGG substrate 59

Figure 4.14 Raman shifts as a function of film thickness showing enhancement in intensity ratio and shifts in relative peak position. Reprinted with permission from: ref. [1] Fig. 3 60

Figure 5.1 (a) Horizontal and (b) vertical normal modes arises in an elliptical birefringent medium due to the combination of linear birefringence with the optical gyrotropy in such medium 66

Figure 5.2 Magnetization reversal in elliptically birefringent MO waveguide pushes elliptical normal modes to the equatorial plane reflected positions (pointed by the dashed arrow) in a Poincaré sphere. Reprinted figure with permission from**:** ref. [2] Fig. 2 67

Figure 5.3 Measured multiple TE and TM stop bands (normalized to waveguide transmittance) in the presence of a transverse magnetic field, from the magneto photonic crystals fabricated on the ridge waveguide in an iron garnet film. Reprinted figure with permission from**:** ref. [2] Fig. 2 68

Figure 5.4 Stack model with two periodically varying elliptical birefringent layers of thicknesses d_1 and d_2. In each layer, propagation of an optical wave can be expressed by the local normal modes of the layer. Based on this model, a

transfer matrix is formulated to calculate the transmittance from the full crystal. 69

Figure 5.5 SEM images of (a) ridge waveguide structures and (b) a mirror polished ridge waveguide facet fabricated on iron garnet film. With kind permission from Springer Science and Business: ref. [3] Fig. 6.1 73

Figure 5.6 (a) Photonic crystal structure, reprinted figure with permission from**:** ref. [2] Fig. 4 and (b) photonics crystals (white) with ridge waveguide structure fabricated on iron garnet film**.** 75

Figure 5.7 Optical transmittance spectra from a ridge waveguide structure is recorded using a digital power meter and a 1480 –1580nm laser source. Polarization output from the lensed fiber is prepared using rotating Glan-Thomson analyzer and a $\lambda/4$ plate in the absence of a sample. In the transmission measurement, these two components are removed but ridge waveguide sample is mounted in line with the lensed fiber for direct-end coupling..... 77

Figure 5.8 A 360° analyzer scans of TE (curve 1) and TM (curve 2) polarization states 78

Figure 5.9 A 360° analyzer scan of 26° ellipse with semi-major axis orientation in horizontal (curve 1) and vertical (curve 2) directions 80

Figure 5.10 A 360° analyzer scans show that the elliptical normal mode (curve 1) and its conjugate helicity mode (curve 2) have a semi-major axis orientation overlap at the input (a) of a plain ~1.2 mm long waveguide, however they differ significantly at the output (b). The normal mode (curve1) maintains its elliptical shape and orientation. Reprinted figure with permission from**:** ref. [2] Fig. 5 83

Figure 5.11 Forward fundamental to second order-mode back-reflected stop bands (normalized to the transmittance of a plain waveguide) for horizontally and vertically-oriented elliptical normal modes in a longitudinal magnetic field, (a) in beam propagation direction and (b) opposite to propagation direction. Magnetic field reversal converts the conjugate helicity modes to normal

modes. TE and TM stop bands are in the plots for comparison. With kind permission from Springer Science and Business: ref. [3] Fig. 6.10.....85

Figure 5.12 Forward fundamental to second order-mode back-reflected stop bands for elliptical normal-modes (black and blue curves) and their conjugate helicity modes (red and green curves), normalized to the transmittance of a plain waveguide. With kind permission from Springer Science and Business: ref. [3] Fig. 6.11.....86

Figure 5.13 Simultaneous reversal of helicity (and magnetization) reproduces the forward fundamental to second order-mode back-reflected stop bands spectra for vertical and horizontal normal modes. With kind permission from Springer Science and Business: ref. [3] Fig. 6.11.....86

Figure 5.14 Calculated fundamental forward to second order-mode back-reflected stop bands for opposite helicity elliptical normal modes along with the TE and TM modes. With kind permission from Springer Science and Business: ref. [3] Fig. 6.11 87

Figure 5.15 (a) The theoretical Bloch mode reconfiguration is tested by calculating a forward fundamental to second order-mode reflected stop band for a horizontal elliptical mode for two directions of a longitudinal magnetic field. Similarly (b) in experiment reconfiguration is tested for the same stop band by a normal mode and its conjugate helicity mode for a photonic crystal 10 μm away from the input side on the waveguide. With kind permission from Springer Science and Business: ref. [3] Fig. 6.11 88

Figure A2.1 Malus's law can be explained using the propagation of a monochromatic plane wave through a polarizer and an analyzer.....109

List of Tables

Table 2-1: Ion position in Yttrium Iron Garnet unit cell 11

Table 4-1: Compositional analysis done on film $Bi_{0.8}Gd_{0.2}Lu_2Fe_5O_{12}$ with GGG substrate by *EAG* 56

Table 4-2: Uncertainties in the film compositions calculation used by *EAG* 57

Table 4-3: Average atomic number density of garnet films 58

Table A3-1: Number density of different elements of $Bi_{0.8}Gd_{0.2}Lu_2Fe_5O_{12}$ film and $Gd_3Ga_5O_{12}$.....110

Table A3-2: Atomic number density of magnetic garnets calculated from the lattice constant 112

Preface

The present dissertation is based on my PhD research work in Engineering Physics at the Michigan Technological University conducted during the period August 2008-April 2015. This preface serves as an explanation of my role in the work that comprises each of the chapters that make up the body of this dissertation. The research studies conducted under this dissertation work include, in part, text and images published in the following three peer-reviewed journal articles and a book chapter.

1. Ashim Chakravarty, Miguel Levy, Amir A. Jalali, Zhuoyuan Wu, and Alexander M. Merzlikin, 'Elliptical normal modes and stop band reconfiguration in multimode birefringent one-dimensional magnetophotonic crystals', Phys. Rev. B 84, 094202 (2011).
2. Neluka Dissanayake, Miguel Levy, A. Chakravarty, P. A. Heiden, N. Chen, and V. J. Fratello, 'Magneto-photonic crystal optical sensors with sensitive covers', Appl. Phys. Lett. 99, 091112 (2011).
3. Miguel Levy, Ashim Chakravarty, Pradeep Kumar and Xiaoyue Huang, 'Magnetophotonic Bragg Waveguides, Waveguide Arrays and Nonreciprocal Bloch Oscillations', Publisher: Springer (April 2013).
4. Miguel Levy, A. Chakravarty, H.-C. Huang, and R. M. Osgood Jr., 'Large magneto-optic enhancement in ultra-thin liquid-phase-epitaxy iron garnet films', Appl. Phys. Lett. 107, 011104 (2015).

I (Ashim Chakravarty) have coauthored the above listed published journals in the "Physical Review B" and "Applied Physics Letters" journals of the American Physical Society (APS), American Institute of Physics (AIP) and book chapter by Springer publication, respectively. I have the necessary copyright permission from APS and AIP (see Appendix 1) to reproduce, text and images, from the above listed journal articles in the present dissertation titled:

"GEOMETRY INDUCED MAGNETO-OPTIC EFFECTS IN LPE GROWN MAGNETIC GARNET FILMS".

Chapter 1, Chapter 2, and Chapter 3 do not include any collaborative or published work.

Chapter 4 includes my recent study on enhancement of specific Faraday rotation in ultra-thin magnetic garnet films. This work is published recently in the journal of Applied Physics Letters and it is at 4 from aforementioned publication lists. This work was initiated by me and Professor Miguel Levy at MTU and the central ideas and key experimental measurements were conducted by us at MTU. Professor Richard M. Osgood and his student Hsu-Cheng (Stan) Huang from Colombia University, joined this effort at a later stage, contributing the Raman spectroscopy of samples prepared in our laboratory. Professor Hassaram Bakhru and his student Girish Malladi at the State University Of New York at Albany also joined at a later stage to supplement our data with Rutherford back-scattering analysis on these same samples. I have contributed to this work by developing an ultra-sensitive Faraday rotation set-up, spin-wet etching set up, and magnetic circular dichroism measurement set up for studying ultra-thin magnetic garnet films. In this study, I have done all optical measurements and analysis of the enhancement in Faraday rotation in magnetic garnet films.

Chapter 5 in the dissertation is based on the results published journal at 1 and the book chapter at 3 in aforementioned publication lists. Chapter 5 addresses an important technological need, namely the development of on-chip optical switch and optical sensor devices for optical communications and sensing. Professor Miguel Levy and I initiated the idea and I did numerical calculations, and conducted experiments on ridge waveguides. Amir A. Jalali helped formulating the theory and Alexander M. Merzlikin reviewed the results in that journal. In that journal, Zhuoyuan Wu prepared some samples for optical testing. This work is reproduced in a Springer book chapter along with the work on nonreciprocal Bloch oscillations. Pradeep Kumar and Professor Miguel levy performed numerical calculations to see nonreciprocal Bloch oscillations form ridge waveguide structures and published their work in other journals as well. In the book chapter, Xiaoyue Huang is a co-author as because he initially setup the waveguide testing lab at MTU and optimized waveguide sample preparation processes. Some of his data and images are used in that book chapter. In this dissertation, I included only my part of work from those two aforementioned publications.

Chapter 6 summarizes the important findings of this dissertation and provides directions for the future work.

Research work conducted for journal at 2 from aforementioned publication lists is not included in this dissertation.

Acknowledgements

This work would not have been a success without the love and support of two great personalities: Prof Miguel Levy and my recently deceased mother. First, I would like to express my sincere gratitude to Professor Miguel Levy for giving me the opportunity to work in his supervision. His constant encouragement, guidance and support help me doing my PhD research in the field of experimental optics. I would like to thank Professor Levy sincerely and graciously for always being available to help me inside or outside academic whenever I needed it.

It would have not been possible for me to come this far without the tremendous love and support from my mother. From my childhood, she always pushed me to do well in my studies and it was her strong determination which helped me a lot to step in to this university and perform this research work. I cannot return her anything but I will remember always her for giving me this educated life. Here, I would also like to thank all my family members for their moral support and encouragement throughout.

In the meantime, I also like to take names of my former teachers back from my High-School and Bachelor studies here. In my childhood, I learnt science and math from Ajit Kalita sir and he showed me the way to do scientific things analytically. I am very much thankful to him for providing me this knowledge. Paban Sahariah sir from Cotton College, Guwahati actually was the main motivator to my journey to Michigan Technological University, USA. He inclined me to love physics during his teaching in my Bachelor studies. I always remember him for being a good mentor in my studies as well as providing me moral support always.

My work would not be successful without the collaboration with the group of Professor Richard M. Osgood and Hsu-Cheng (Stan) Huang at Columbia University, New York, and Professor Hassaram Bakhru and Girish Malladi at SUNY-Albany. Special thanks to Hsu-Cheng (Stan) Huang for carrying out micro-Raman measurements, and Girish Malladi for the RBS measurements and fruitful discussions.

I take this opportunity to acknowledge the help from my colleagues. Dr. Zhuoyuan Wu, Dr. Pradeep Kumar and Dr. Neluka Dissanayake introduced me to various experimental

methods at the beginning of my PhD career. Thanks to Dr. Colin Gurganus for helping me in developing a LabVIEW program for Faraday rotation experiment. I am grateful to Patrick Bowen for receiving immense help not only in atomic force microscopy measurement and correcting this document but also discussing issues related outside the academic endeavors. Thanks to my friends Niraj Dhittal, Abhay Pratap Singh and Dolendra Karki for their help while pursuing their own graduate studies.

I am grateful to Professor Ravindra Pandey; staffs, specially Jesse J. Nordeng, and fellow graduate students in the Department of Physics. I appreciate Dr. Ramy El-Ganainy for his insightful remarks while pursuing experimental works for this dissertation. I would like to thank Owen P. Mills and William Knudsen from the Material Science and Engineering Department for their help on characterization equipment. (Summer 2010) I am also thankful to the National Science Foundation and to MTU's Department of Physics for financial support. Last but not the least, I would like to thank my advisory committee members: Dr. Yoke Khin Yap, Dr. Jae Yong Suh, and Dr. Durdu Guney for having spent time providing me with valuable suggestions in my dissertation work.

Abbreviations

AFM	Atomic Force Microscope
Bi: YIG	Bismuth-substituted Yttrium Iron Garnet $(Bi, Y)_3Fe_5O_{12}$
CAIBE	Chemically Assisted Ion Beam Etching
FR	Faraday rotation
FIB	Focused Ion Beam
GGG	Gadolinium Gallium Garnet ($Gd_3Ga_5O_{12}$)
LCP	Left Circularly Polarized
LPE	Liquid Phase Epitaxy
MCD	Magnetic Circular Dichroism
MO	Magneto-Optical
MPC	Magneto photonic crystal
NPGS	Nano Pattern Generation System
PC	Photonic Crystal
PBG	Photonic Band Gap
PSB	Photonic Stop Band
RBS	Rutherford backscattering Spectrometry
RCP	Right Circularly Polarized
SEM	Scanning Electron Microscope
TE	Transverse Electric
TM	Transverse Magnetic
TEM	Transmission Electron Microscopy
XRD	X-Ray Diffraction
YIG	Yttrium Iron Garnet $Y_3Fe_5O_{12}$

Abstract

This dissertation addresses dimensionality-induced magneto-optic effects in liquid-phase-epitaxy magnetic garnet thin films. It is found that the Faraday rotation (FR) per unit length evinces a marked and steady enhancement as the film thickness is reduced below ~100 nm in $Bi_{0.8}Gd_{0.2}Lu_2Fe_5O_{12}$, although it remains constant in the micron- and most of the sub-micron-regime. The reported specific FR change in such reduced dimensions is due to size-dependent modifications in diamagnetic transition processes in the garnet film. These processes correspond to the electronic transitions from the singlet ^6S ground state to spin-orbit split excited states of the Fe^{3+} ions in the garnet. A measurable reduction in the corresponding ferrimagnetic resonance linewidths is found, thus pointing to an increase in electronic relaxation times and longer lived excitations at reduced thicknesses than in the bulk. These changes together with a shift in vibrational frequency of the Bi-O bonds in the garnet at reduced thicknesses result in magneto-optical enhancement in ultra-thin garnet films.

This dissertation also studies optical transmittance control through multimode elliptically birefringent waveguides achieved by one-dimensional magneto-photonic crystals (MPCs) and the tuning of longitudinal magnetic bias in such waveguides, together with the tuning of the helicity of the input elliptical beam. Magnetization reversal is found to strongly reconfigure the stop band spectrum, through hybridization of the elliptically-polarized states due to normal mode symmetry breaking.

Chapter 1

Introduction

Unique optical and magneto-optical properties of magnetic garnet films motivates to explore the fundamental physics and practical use of such films. The capability of tuning the electronic band structure of the material by external magnetic fields makes the study of these films highly interesting. In magneto-optic materials, the spin-orbit interaction arises at inter- and intra-band optical transitions due to the applied magnetic field. This induces additional off-diagonal components in the effective permittivity tensor and drastically impacts optical and transport properties of the propagating light through the material by making the media gyrotropic in nature. In the presence of gyrotropy, these films become non-reciprocal in character. Intrinsic non-reciprocity makes such films a highly demand candidate for commercial applications.

Recent advances in fabrication techniques and the development of sophisticated characterization tools has led to the study of micro-nano structures fabricated in magnetic garnet films. Artificial optical bands can be created in such media by fabricating periodic structures on it. Such periodic structures, namely magneto-photonic crystals (MPC), facilitate the molding of the flow of light in various media. In the MPC, an external magnetic field plays a crucial role as an extra degree of freedom to manipulate the photonic band structure, diffraction patterns, and the polarization state of light. As the MPC dispersion relation mimics a semiconductor band diagram and controls the flow of electromagnetic wave through it, a connection is created between two major fields of physics very well, namely solid state physics and electrodynamics. For this reason study of MPCs is of great significance.

1.1 Literature Review

This dissertation presents a study on magneto-optic properties of magnetic garnet films. The study has been spurred by the central role played by magneto-optic non-reciprocity in technologically important optical devices such as isolators and circulators [4-18]. Film-

growth processes and elemental substitutions in these materials have been extensively investigated [9-12, 15, 17-19]. Enhancing the specific FR and reducing optical absorption losses are strong motivators to improve the optical performance of nonreciprocal devices. Early on, interest in magnetic memory applications of iron garnets (bubble memory) has also played a role in the development of better materials [18].

The origins of Faraday rotation in magnetic garnet media are well addressed by S. Wittekoek and co-workers [11], Dionne [20], Allen and Dionne [21], and F. Hansteen et al. [22]. Methods like bismuth- and cerium-substitution in rare-earth iron garnets have been found to enhance the specific Faraday rotation in these materials and are discussed in numerous publications [9, 11, 17, 18, 20, 22, 23]. Also, the enhancement in Faraday rotation is tested by fabricating micro or nano structures on the garnet films [24-27]. Dimensional effects on magneto-optic properties in garnets films have revealed changes in specific Faraday rotation [23]. However, the reported changes are not monotonic, unlike the findings discussed in the present dissertation. No clear-cut enhancement in gyrotropic response is reported in other works and the effect is ascribed to a transition between the ferrimagnetic phases. Sputter-deposited films of various thicknesses determined from sputter-deposition rates are used in those studies. A key difference with the reported work here is that use of monocrystalline LPE-grown films, and that all the films come from the same wafer, thus guaranteeing no compositional variations due to random changes in growth conditions.

Primary interest of this dissertation work is to investigate dimensional effects in the magneto-optic response of ultra-thin liquid-phase-epitaxially (LPE)-grown monocrystalline films by studying the FR effect and circular dichroism. Monocrystalline samples of $Bi_{0.8}Gd_{0.2}Lu_2Fe_5O_{12}$ are used in this investigation. These single-layer bismuth-substituted-rare-earth iron-garnet films are grown by liquid-phase-epitaxy on (100) gadolinium gallium garnet ($Gd_3Ga_5O_{12}$) substrates (GGG). They exhibit planar magnetic anisotropy and an extrapolated perpendicular saturating field similar to their saturation magnetization of $4\pi M_s \approx 1800G$. The film composition chosen for the sample films yields lattice parameter matching with that of the substrate to within ± 0.001Å. Special emphasis

is given on precise thickness and compositional characterization of the films, as described in chapter 4. Along with the other studies, micro-Raman study is also performed to these films. Detected vibrational peaks from these ultra-thin films reveal that lattice vibration changes impact the specific Faraday rotation of magneto-optic film. The Faraday rotation enhancement in ultra-thin magnetic garnet films presented here is expected to find applications in magneto-optic imaging [28-31] and quantum telecommunication devices [32-35].

Second major study, this dissertation, addresses optical wave propagation through a periodic media. Optical waves are inherently periodic in nature and thus interact with a periodic media in a unique way. Šolc folded filters (ŠFF) are one such type of periodic media which demonstrates a new type of optical phenomena by introducing optical wave interaction with tunable periodic structures decades ago [36]. Through intentional misalignments of the optic axes of the two constituent materials, ŠFFs constitute a pure representation of one-dimensional photonic crystals (PC), exhibiting photonic band gaps (PBG) within the Brillouin zone [37]. PCs are used in many applications, including as waveguides [38, 39], waveguide resonators [40-42], spectral filters [43-45], optical sensors [46, 47], optical switches [48, 49], multichannel nano-filters [50, 51], low-threshold nano-lasers [52, 53] and many others. Most of these applications are mainly due to the presence of PBGs in periodic media. Dynamic tuning of the PBGs is highly considered to achieve parametric control of the optical properties of the PCs in most of these PCs based applications. PBGs induce severe attenuation of the light wave propagating through the PCs and this is extended over a finite range of spectral bands. In a spectral band, the constituent layers of the PCs create destructive interference among the forward propagating waves and block their transmission. Such spectral bands through the PBGs are called photonic stop bands (PSB). Tunability of the PCs to tune the PBGs and control the stop band has been explored through variety of ways. Among different mechanism to control the PSB, through variations in the angle of incidence of the optical beam [54], electrical [55-60], magnetic [61-64], thermal [64, 65], and mechanical control [66] are well known. Immersion of PCs in coherent atomic gases and control the PSBs also have been studied [67]. Another example of magnetic tunability of PSB has been recently addressed through

one-dimensional MPCs [2, 3, 27, 68]. In 1D MPCs, one of the two constituent materials are made of ferromagnetic garnet and therefore optical gyrotropy can be triggered in such PCs by impressing magnetic field externally. Other studies on such MPCs consisted of theoretical band gap analysis focusing on dielectric permittivity or magnetic permeability, local normal mode coupling and Bloch states in elliptically birefringent periodic stack [2, 69-71]. Through magneto-photonic stop band manipulation in MPCs, fast magneto-optical switching of 40fs magnetization switching effects has been achieved, which is very appealing for magneto-optic based technology [72].

This dissertation addresses a different mechanism of stop band tuning through magnetic bias particularly suitable to multimode magneto-optic waveguides. Due to the presence of higher order waveguide modes in such waveguide system, fundamental waveguide modes couple differently to these modes, generating multiple stop band spectra through inter-modal back-reflection processes. Along with the back reflection of higher order modes, mode helicity plays a crucial role in the transmittance of optical waves propagating through such waveguide. In the presence of longitudinal magnetization, TE modes couple to the TM modes due to the activation of optical gyrotropy in a magneto-optic waveguide. Hence, the optical gyrotropy prevents the TE and TM modes from functioning as eigen-modes of the wave equation. After coupling of TE and TM modes, normal modes in such waveguides become elliptically polarized. Shape anisotropy and lattice mismatch strain facilitate the generation of elliptical polarization states as normal modes in the longitudinally magnetized ridge waveguide structure. The experimental work presented here shows that elliptically polarized inputs propagate with small change to their polarization state in such waveguides and hence can be regarded as fundamental normal modes in such structures. The PSB tuning in elliptically-birefringent multimode waveguides is dependent on to these normal modes and applied longitudinal direction of the magnetic bias. Here, the spectral shape of the PSB is based on the hybridized coupling between different forward and back reflected elliptically-polarized waveguide modes. The change of magnetic bias in the reverse longitudinal direction affects the PSB shape as this changes the helicity of the waveguide normal modes. Reversal of the magnetic bias converts the elliptical polarization states from normal to hybrid modes and thus impacts on PSB magnetic tuning. This study

also addresses actual PBG tuning by Bloch mode reconfiguration which in turn produces change in the transmittance through MPC. However, PSB spectra change minimally in this case compared to the input polarization changes on magnetization reversal.

1.2 Organization of Dissertation

This dissertation work is divided into five chapters beyond this introduction. Chapters two and three provide relevant background on iron garnet magnetism, polarized light and magneto-optic effect in magnetic garnet media, YIG band structure and origin of FR in magnetic garnets, fabrication and characterization methods of these garnet films, optical waveguide theory, theory of gratings in waveguide structures, photonic crystals, and photonic bandgaps.

In chapter four, an experimental background section covers the FR measurement setup, sample preparation, thickness measurements, RBS analysis for compositional check, micro-Raman analysis for lattice vibration change, FR measurements, and absorption loss (dichroism) measurements on magnetic garnet films. The chapter gives the centrality to the enhancement in specific FR in the ultra-thin magnetic garnet films. Magnetic Circular dichroism measurements are used as cross comparison to the specific FR enhancement, since they provide an independent check on FR measurements through the Kramers-Kronig relations.

Chapter five presents a theoretical part on photonic-stopband and back reflection processes in elliptically birefringent magneto-optic media by considering gyrotropic layered stacks as a medium of propagation for the waveguide normal modes. The experimental part consist of fabrication and characterization of ridge waveguides and one dimensional photonic crystals in magneto-optic films, normal modes in longitudinally magnetized ridge waveguides and PSB tuning by using these normal modes and magnetization. A small section in the chapter describes tuning of Bloch modes and transmittance control through MPC.

Chapter six summarizes the dissertation and proposes possible directions for the future of this research.

Chapter 2

Magnetic Garnets: Origin of Faraday rotation

Magnetic garnet films in the presence of external magnetic fields manipulate the polarization state of a monochromatic and coherent optical beam upon traversing the beam through such films. Light and matter interactions inside the magnetic garnet system are inevitable for the occurrence of such a polarization state change of the optical beam. Inherently, the magnetic garnet crystal structure is mainly responsible for these interactions. The ability to manipulate the polarization of optical beams brings a wide variety of uses for magnetic garnet film in optics and semiconductor based applications. For instance, optical isolators and optical circulators are devices where magnetic garnets are used. Therefore, in this chapter, the fundamentals of optical polarization, iron garnet crystal structure, Faraday Effect, origin of FR in magnetic garnet system, and growth technique of magnetic garnet film are to support the research work presented in chapter 4. Magnetism plays a crucial role in achieving the Faraday-Effect from the magnetic garnet films. Thus, the former section of this chapter covers magnetism in material.

2.1 Magnetism in Materials

The orbital and spin motions of electrons and their interactions with one another generates magnetism to a given material. It is worth to mention here that all materials are magnetic in nature. An applied magnetic field $\mathbf{H}$ induces magnetization $\mathbf{M}$ inside the material by aligning the magnetic dipoles along the direction of the field and therefore the magnetic field inside the material can no longer be $\mathbf{H}$; rather, the applied field generates an induced magnetic field $\mathbf{B}$ also known as magnetic induction. The magnetic induction induced on the material from the field $\mathbf{H}$ can be written as

$$\mathbf{B} = \mu_0 (\mathbf{H} + \mathbf{M}), \tag{2.1}$$

where μ_0 is the permeability of the free space which is $4\pi \times 10^{-7}\ H.\ m^{-1}$. The units of $\mathbf{H}$ and $\mathbf{M}$ are Ampere per meter (A/m) and of B weber/m^2 or Tesla (T). Here, $\mathbf{M}$ is the magnetic moment density of a material upon the application of a magnetic field. On the

other hand, material magnetization is related to the magnetic moments of the individual atoms or molecules, and their exchange and dipole moment interactions.

In relation to magnetization, another material parameter called magnetic susceptibility χ relates the $\mathbf{M}$ magnetization with the applied field **H.** If the applied field is small enough then the magnetization has linear dependency to the applied field and can be written as

$$\mathbf{M}=\chi\mathbf{H}. \tag{2.2}$$

Using magnetic induction and the magnetic susceptibility from Eq. (2.1) and Eq. (2.2), the permeability μ of a material can be written as

$$\mu = \mu_0 (1+\chi). \tag{2.3}$$

The best way to introduce the different types of magnetic materials is to describe how materials respond to magnetic fields. In that case, magnetic susceptibility distinguishes high to low magnetization materials based on the collective interaction of atomic magnetic moments occurring in the material. Since the magnetic susceptibility χ from Eq. (2.2) is a function of the external field, the magnetic materials can be classified as diamagnetic, paramagnetic, ferromagnetic, and ferrimagnetic, respectively, depending on the nature of χ.

In diamagnetic materials, there are no net magnetic moments, because all the orbital shells of the atoms of these materials are occupied with electrons. However, when exposed to a magnetic field, orbiting electrons oppose the field, and as a result, a negative magnetization is produced; thus the susceptibility is negative. Unlike diamagnetic materials, in paramagnetic materials, some of the atoms or ions have a net magnetic moment due to unpaired electrons in partially filled atomic orbitals. The cause of net positive magnetization and positive susceptibility in this kind of material is due to a partial alignment of the atomic magnetic moments in the direction of the applied field. In absence or withdrawal of the magnetic field, in paramagnetic material, dipole moments of such materials are randomly oriented, as the individual magnetic moments do not interact magnetically. However, in the absence of a field, also in ferromagnetic and antiferromagnetic materials, the atomic moments exhibit very strong interactions. In the interior, these material is divided into magnetic domains, each of which is spontaneously

magnetized. The exchange interactions among these domains produces parallel (ferromagnetic) or antiparallel (antiferromagnetic) alignment of atomic moments. Due to this spontaneous magnetization and magnetic ordering property, a saturation magnetic field is always required to completely magnetize these materials. Similarly, a ferrimagnetic system also requires a saturation field due to the same properties. In this type of magnetic structure, two magnetic sublattices are separated by anions. The exchange interactions are mediated by anions via a super-exchange interaction mechanism. The strongest super-exchange interactions result in an antiparallel alignment of spins between two sublattices, but of different magnitudes. Hence, ferrimagnetic materials also have nonzero resultant magnetic moments. Iron garnet films for magneto-optical applications has a ferrimagnetic ordering and therefore all unit cells form domain structures inside the bulk material as shown in Figure 2.1(a). Figure 2.1(b) shows that all unit cell magnetic moments in the iron garnet material can be aligned for magneto-optic activities by applying a strong magnetic field.

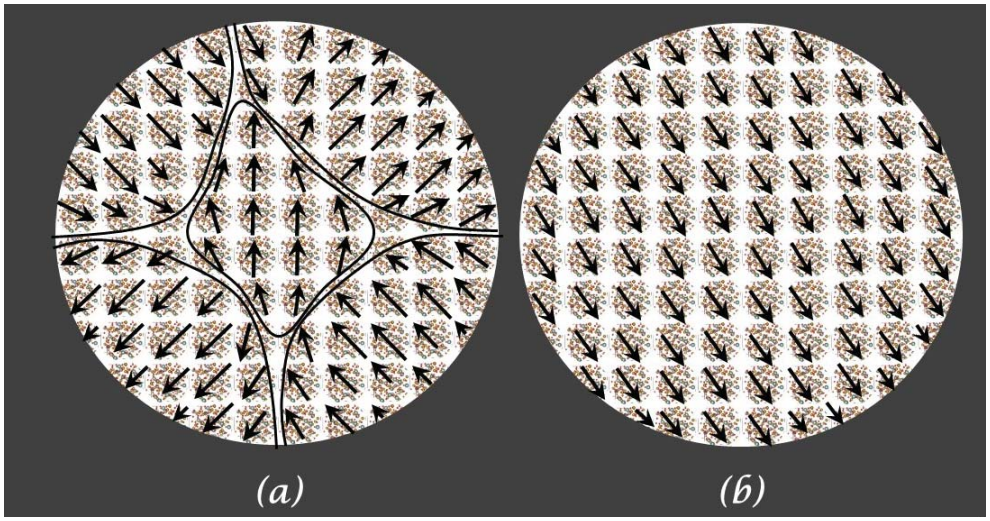

Figure 2.1 (a) Unit-cell dipole moments in iron garnets form domain structures and (b) an applied magnetic field align these moments for magneto-optic activities in such garnets.

2.2 Crystal Structure of the Garnet Family

Naturally occurring silicates with prototypic chemical formula, $\{C^{3+}\}_3[A^{3+}]_2(Si^{3+})_3O_{12}$, where C and A stand for the ions that occupy sublattices other than Silicon in a crystal

structure was originally named as garnet [8]. The first synthesis of an iron garnet was done by Bertaut and Forrat [73]. Analysis of the iron garnet crystal structure was carried out by Geller and Gilleo [74, 75]. The iron garnet structure belongs to the centrosymmetric space group Ia3d (O_h^{10}) and is crystalline. Therefore, it is considered to have cubic symmetry. Most of the synthetized iron garnets are ferrimagnetic and therefore, a cubic symmetry of the crystal structure is not a correct assumption, as they have spontaneous polarization and magnetization. The garnet structure has three cation sites: tetrahedral d, octahedral a, and dodecahedral c, as shown in a section of the crystallographic unit cell in Figure 2.2 (inset). Oxygen anions coordinates to these cation sites with co-ordination numbers 4, 6 and 8 respectively. There is no translational degree of freedom to the cations, since they are surrounded by O^{2-} anions. Oxygen ions occupy the *h*-positions in the crystal structure and have three degrees of freedom. The unit cell of the garnet crystal contains 8-formula-units, having 20 ions in each unit. However, the primitive unit cell of the garnet crystal structure contains 80 ions only. There is a total of 160 ions at four different sites: 24 ions occupy the tetrahedral d sites, 16 ions occupy the octahedral a sites, 24 ions occupy the dodecahedral c sites, and 96 oxygen ions surround these three sublattices.

Spontaneous magnetization in iron garnets arises from the dominant d sublattice contribution to the magnetization, as the ratio of the tetrahedral sites to the octahedral sites in the crystal structure is 3:2. The sublattice magnetization determines the saturation magnetization M_s of the garnet crystal, where M_s is a temperature-dependent quantity. In some garnets, e.g. Yttrium Iron Garnet (YIG), the dodecahedral sub-lattice makes no contribution to the magnetic moment of the crystal. Doping of larger sized ions to the dodecahedral sites in such garnet crystals can change the saturation magnetization. Therefore, the saturation magnetization $M_s(T)$ of the garnet can be written as the vector sum of the magnetizations coming from all the sublattices. It can be expressed as

$$M_s(T) = \left| M_d(T) \pm M_c(T) - M_a(T) \right| , \tag{2.4}$$

where $M_d(T)$, $M_c(T)$, and $M_a(T)$ denote the temperature-dependent saturation magnetizations of tetrahedral, dodecahedral, and octahedral sites, respectively.

In the garnet family, YIG is the basic magnetic host, and properties of YIG can be altered by a variety of substitutions. YIG belongs to the ferrimagnetic class of material with ionic formula $\{Y^{3+}\}_3[Fe^{3+}]_2(Fe^{3+})_3O_{12}$ and is widely used for magneto-optic devices. Important applications at far visible and infrared frequencies, namely optical isolators, oscillators, circulators and others, use YIG due to its properties of large FR and high saturation magnetization. Some of the measured properties such as FR, absorption, and refractive index for YIG at 1310nm wavelength are given as 214 degrees/cm, 0.05 cm^{-1}, and 2.2 respectively. YIG, which has an average lattice parameter of 12.378 Å, is very large in comparison to other materials and due to this large and open structure of YIG, many advantageous derivatives can be grown through substitution processes. In the YIG structure, Fe^{3+} ions occupy two sublattices, octahedral and tetrahedral sites, which possess antiparallel and unequal magnetic moments resulting in a net magnetization of 5 Bohr magneton along the tetrahedral direction. The YIG unit cell, as shown in Figure 2.2, can be derived from the point positions of the space group Ia3d (O_h^{10}) given in Table 2-1. In the table, I and κ refers to $(0,0,0;1/2,1/2,1/2)$ and cyclic permutation (e.g. $(x,y,z)\kappa$ means $x,y,z;z,x,y;y,z,x$) respectively. Oftentimes, YIG is synthetized on a substrate

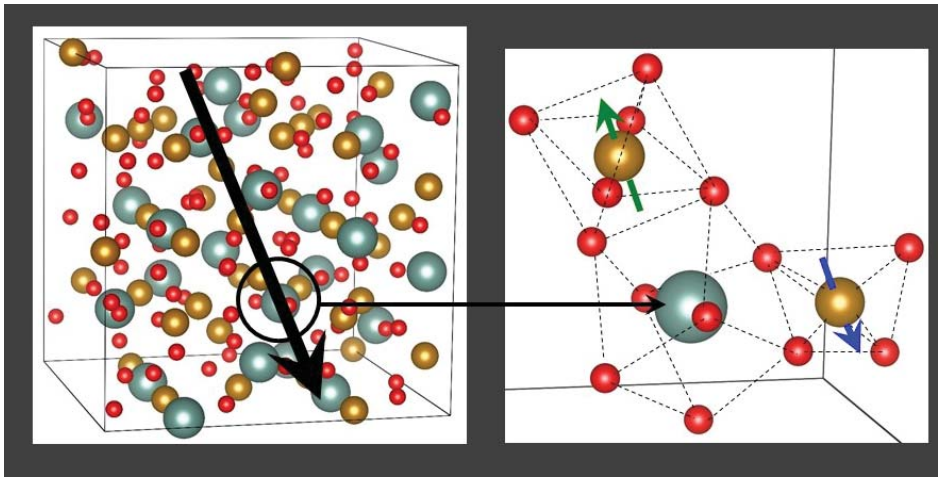

Figure 2.2 YIG crystal with a black arrow pointing the magnetic moment of the cell. Inset shows spin-down tetrahedral and spin-up octahedral Fe^{3+} ions (brown) with Y^{3+} ions (faded blue) in dodecahedron.

called gadolinium gallium garnet (GGG) due to their proximate lattice constants. The empirical formula of GGG is given by $Gd_3Ga_5O_{12}$, and the GGG crystal has 12.383 Å

lattice constant. Unlike YIG, the GGG crystal is paramagnetic in nature. With 1.9345 refractive index, GGG is transparent to IR absorption. Magnetic, crystalline, optical and other properties of YIG can be hugely modified through bismuth substitution for magneto-optic applications. The larger ionic radius of bismuth compared to yttrium produces a

Table 2-1: Ion position in Yttrium Iron Garnet (YIG) unit cell.

YIG lattice constant (a)= 12.378 Å	
[Fe^{3+}] in 16 a	$I+\left(0,0,0;1/4,1/4,1/4;\left(0,1/2,1/2;1/4,3/4,3/4\right)\kappa\right)$
{Y^{3+}} in 24 c	$I\pm\left(1/8,0,1/4;5/8,0,1/4\right)\kappa$
[Fe^{3+}] in 24 d	$I\pm\left(3/8,0,1/4;7/8,0,1/4\right)\kappa$
[O^{2-}] in 96 h	$I\pm(x,y,z;1/2-x,1/2+y,z;x,1/2-y,1/2+z;1/2+x,y,1/2-z;$ $1/4+x,1/4+z,1/4+y;3/4+x,1/4-z,3/4-y;$ $3/4-x,3/4+z,1/4-y;1/4-x,3/4-z,3/4+y)\kappa,$ $x=-0.027, y=0.0567, z=0.1504$ [Ref. [76]]

lattice constant in the Bi: YIG unit cell which can be as large as 12.62 Å with the complete substitution of bismuth to it. At fiber optic communication wavelength, 1550nm, the reported Faraday rotation (FR) for bismuth iron garnet (BIG) is 4300 degrees/cm, which is enormously large compared to that for YIG.

2.3 Polarized light and the Faraday Effect

Material can be made up of various types of molecules, such as spherical, non-spherical, spinal, helical, needle-like, and others. The refractive index of such material depends on the direction of alignment of these molecules inside the material. To study the refractive index of isotropic or anisotropic material, electromagnetic waves are used, as the index of refraction depends on the oscillation of the electric field. The electric field from the electromagnetic wave pushes the electrons from their equilibrium positions inside the material differently depending on the type of molecule and their arrangements in the

material. The physical interaction of wave and matter produces an electromagnetic wave with an electric field, which can oscillate in certain directions and in certain configurations only. This type of electromagnetic wave is known as the polarized wave. In relation to the polarized wave, the Faraday Effect is found in many of the transparent materials, specifically in magnetic materials. The rotation of the plane of polarization of an electromagnetic wave upon passing through a transparent substance, magnetized along the direction of propagation of the wave, is known as the Faraday Effect. More details about polarized electromagnetic wave and the Faraday Effect are discussed in the subsequent sections of this chapter.

2.3.1 Polarization of light

In the complex function representation, the electric field of a monochromatic plane wave of angular frequency ω traveling in the z direction with velocity c is generally described as

$$\mathbf{E}(z,t) = \mathbf{Re}\left[\mathbf{A}e^{i(\omega t - kz)}\right], \tag{2.5}$$

where $i = \sqrt{-1}$, and $\mathbf{A}$ is the complex envelope of an electromagnetic wave and lies in the $x-y$ plane. The polarization of the monochromatic wave can be described by tracing the endpoint of the vector $E(z,t)$ at each position z as a function of time. The x and y components of A can be written in terms of their magnitudes and phases as $A_x \exp(i\delta_x)$ and $A_y \exp(i\delta_y)$. Therefore, the components of the electric field vector in Eq. 2.5 can be written as

$$E_x = A_x \exp\left[i(\omega t - kz + \delta_x)\right] \tag{2.6}$$

and

$$E_y = A_y \exp\left[i(\omega t - kz + \delta_y)\right]. \tag{2.7}$$

From Eq. (2.6) and Eq. (2.7), as time evolves, the curve described by the end point of the electric field in Eq. (2.5) can be achieved by eliminating $(\omega t - kz)$ between the two equations, and hence the polarization of the monochromatic wave can be expressed as

$$\left(E_x/A_x\right)^2 + \left(E_y/A_y\right)^2 - 2\left[(E_x E_y)/(A_x A_y)\right]\cos\delta = \sin^2\delta\,, \tag{2.8}$$

where δ is the phase lag between the electric field components and is given by

$$\delta = \delta_y - \delta_x \tag{2.9}$$

Eq. (2.8) represents an ellipse at a fixed value of z, which is produced by the tip of the electric field vector precessing periodically in the x-y plane as shown in Figure 2.3.

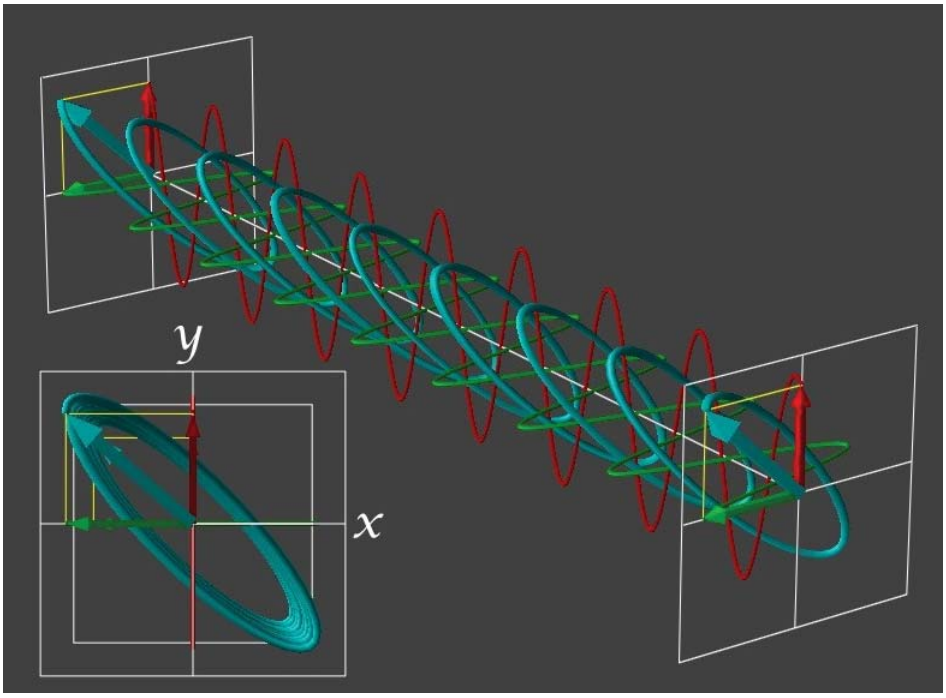

Figure 2.3 Electric field vector end point rotation in the x-y plane and snapshot of its trajectory in frozen time.

The precession direction of the electric field vector defines the handedness of any elliptical polarization state here. If time is frozen at t, then it appears that the locus of the tip of the electric field vector follows a helical trajectory in space (Figure 2.3).

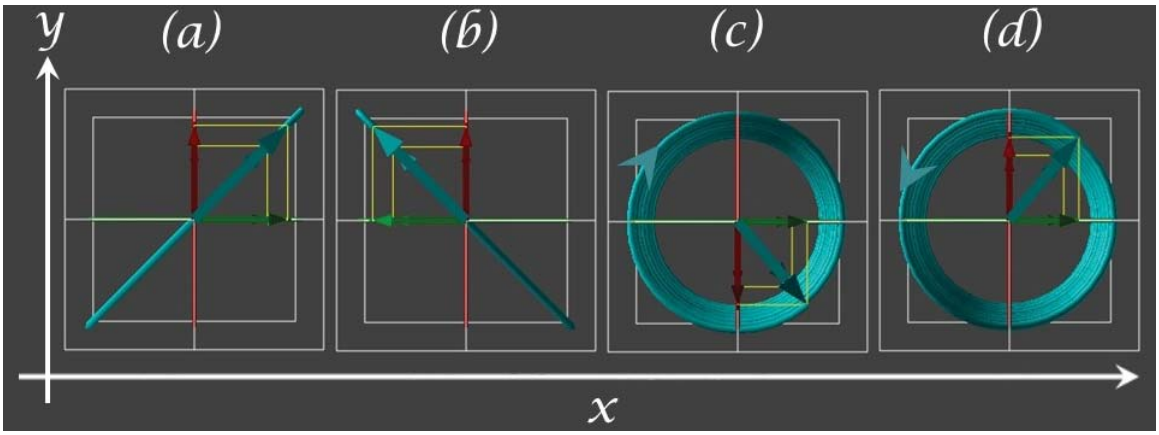

Figure 2.4 (a) 45° and (b) -45° linear and (c) right- and (d) left-circular polarization states of an optical beam.

Linear and circular polarization states of an optical wave in Figure 2.4 are special cases of the ellipse in Eq. (2.8). In linear and circular polarization states, phase lag between the orthogonal components of the optical wave are 0^0 and 90^0 respectively. A circular polarization state can be right- or left- handed depending on the advancement of one or the other orthogonal component of the electric field vector expressed in Eq. (2.6) and Eq. (2.7) by 90^0.

2.3.2 Magneto-optical Faraday Effect

In the absence of an external magnetic field, all magnetic materials are optically isotropic in nature. Application of a static magnetic field alters the electric permittivity tensor ε (Eq. (2.11)) of such magneto-optic material due to the interaction between the light and the internal magnetization of the material. This interaction of the static magnetic field with the orbital motion of the electrons in the material can be described in response to the optical electric field as

$$\mathbf{D} = \varepsilon\mathbf{E} + i\mathbf{E}\times\mathbf{g}\,, \tag{2.10}$$

where **D** is the displacement vector, and $\overline{g}$ is the gyration vector resulting from the applied magnetic field to the material.

Now, if a magneto-optic material is magnetized along the *z* direction by placing it into a

DC magnetic field, then the dielectric tensor ε becomes asymmetric, and can be expressed as

$$\varepsilon = \begin{bmatrix} \varepsilon_{\perp} & \pm ig & 0 \\ \mp ig & \varepsilon_{\perp} & 0 \\ 0 & 0 & \varepsilon_{\square} \end{bmatrix}. \tag{2.11}$$

The above relation assumes the material is lossless, with $\varepsilon_{\perp}, \varepsilon_{\square}$ and g having real values. Here, g is the magnitude of the gyration vector described above and it can switch sign from "positive" to "negative" depending on the forward or backward direction of the applied magnetic field. Due to this gyration vector, a linearly polarized optical wave of wavelength λ, for its normal incidence, decomposes into RCP and LCP normal mode components upon entering into this magnetized-lossless medium. These normal modes advance with different phase speeds through the material as shown in Figure 2.5. At the input of the material, the magnitude of the electric field associated with the RCP and LCP normal modes can be expressed as $E_{+} = (E/2)\exp(i\omega t)$ and $E_{-} = (E/2)\exp(i\omega t)$, respectively. E_{+} and E_{-} propagate along the z direction in the material with propagation constants $\beta_{+} = (2\pi/\lambda)n_{+}$ and $\beta_{-} = (2\pi/\lambda)n_{-}$, where n_{+} and n_{-} are the refractive indices acquired by the normal modes inside the medium and can be expressed using the components of the dielectric tensor in Eq. (2.11) as $n_{+} = \sqrt{\varepsilon_{\perp} + g}$ and $n_{-} = \sqrt{\varepsilon_{\perp} - g}$, respectively. After traversing a distance L inside the material, these two normal modes recombine again at the output end of the material and produce a resultant optical electric field followed by the equation

$$E_{+} + E_{-} = E\cos\left[\omega t - \frac{L}{2}(\beta_{+} + \beta_{-})\right]\exp\left\{i(\beta_{-} - \beta_{+})\frac{L}{2}\right\}. \tag{2.12}$$

Eq. (2.12) indicates a linearly polarized output wave having a plane of polarization with respect to the x axis rotated by an amount

$$\theta_{F} = \frac{L}{2}(\beta_{-} - \beta_{+}), \tag{2.13}$$

which is known as the FR of the optical wave.

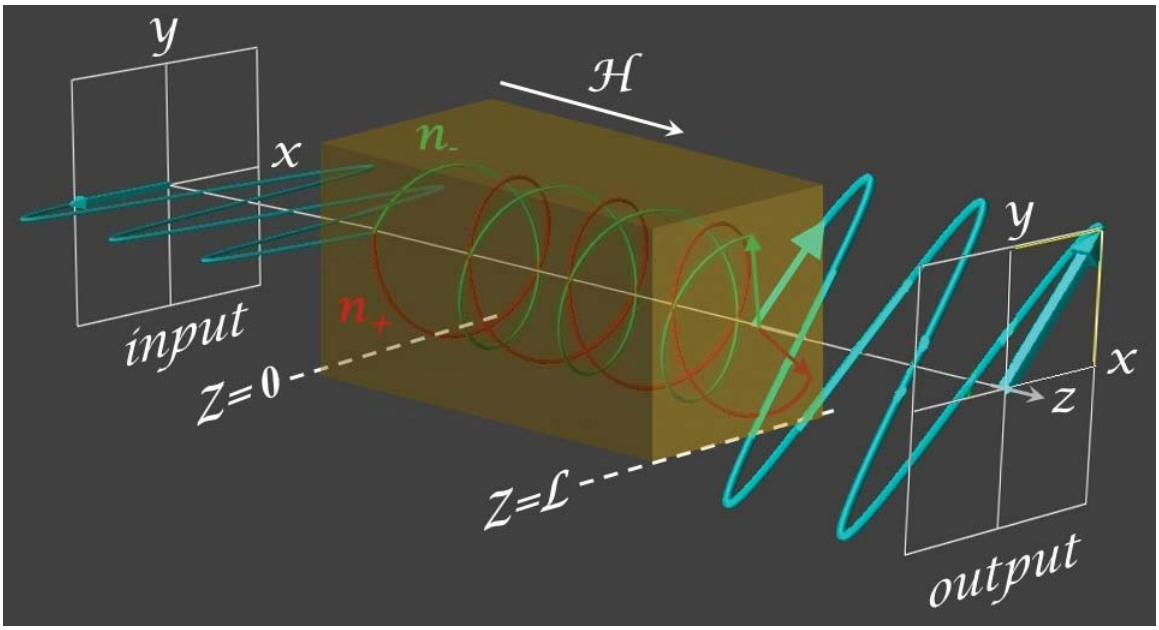

Figure 2.5 In the Faraday Effect, a linearly polarized input optical wave breaks down into RCP and LCP normal modes inside a lossless magnetized material and they propagate with different phase speeds. These normal modes recombine again at the output and produce a rotated linear polarization state.

2.3.3 Faraday rotation in YIG and Bi: YIG

The propagation of electromagnetic waves in YIG and Bi: YIG at optical frequencies can be described by using an electric permeability tensor similar to the tensor in Eq. (2.11), with the difference that each component is complex in this tensor, as absorption is present. FR occurs in these materials if the off-diagonal elements of this tensor are non-zero due to selected optical transitions, mainly coming from electric dipole transitions. This happens when the split-initial or final stationary orbital state for electric-dipole transition separates spectral energies for plane waves of right- and left-handed circular polarization. Orbital angular momentum splitting of these states occurs due to the spin-orbit coupling through the interaction of the rotating dipole electric field and orbital quantum state of the dipole. Depending on the splitting of the initial or final orbital state, there can be two types of optical transitions: (I) a diamagnetic transition (double transition) and (II) a paramagnetic transition (single transition). Here, diamagnetic optical transition refers to an orbital singlet

ground state with spin-orbit split excited states, whereas orbital degenerate ground state with a singlet excited state refers the other type of optical transition as shown in Figure 2.6.

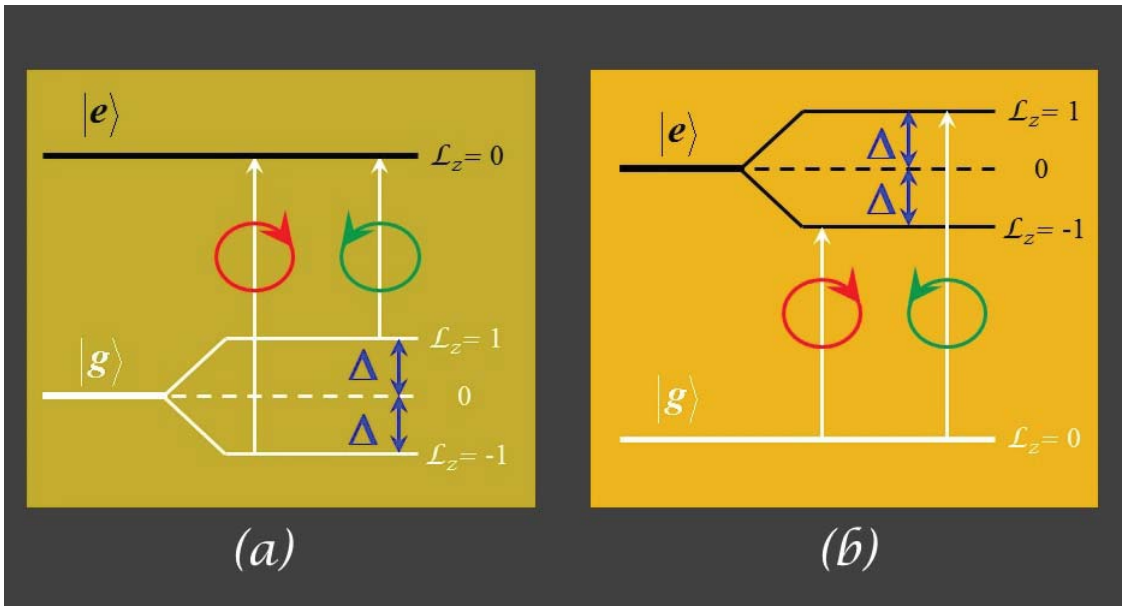

Figure 2.6 Spin-orbit coupling between atomic quantum state and orbital angular momentum makes degeneracy lifting $\mathcal{L}_z = \pm 1$ with Δ amount of energy to the ground state in (a) paramagnetic transition. By the same reason, excited state splits into degenerate states for (b) diamagnetic transition. Faraday rotation is due to the distinctive absorption of RCP (red) or LCP (green) photons, which assist for optical transition of the electron, either from the split ground state to singlet excited ((a) paramagnetic), or from the singlet ground state to the triplet excited states ((b) diamagnetic) in magneto-optic material.

In YIG, FR arises mainly due to the paramagnetic transitions, where the split ground states are thermally populated according to a function called Boltzmann population distribution [77]. Consequently, there is a difference in absorption of RCP and LCP light established due to the different population sites present in the degenerate ground states as shown in Figure 2.7. Different absorptions of these normal modes lead to the refractive index differences between the circular polarizations of the incoming linearly polarized optical wave and hence, the wave goes through a FR to its polarization state. Of a particular note, FR in YIG is a cumulative effect coming from the different paramagnetic optical transitions due to the Fe^{3+} ions in the tetrahedral d and octahedral a sublattices in the YIG crystal. Unlike in YIG, a population-sensitive split ground state, splitting occurs to the excited iron ^3P state by spin–orbit coupling and produces the large value of the off-

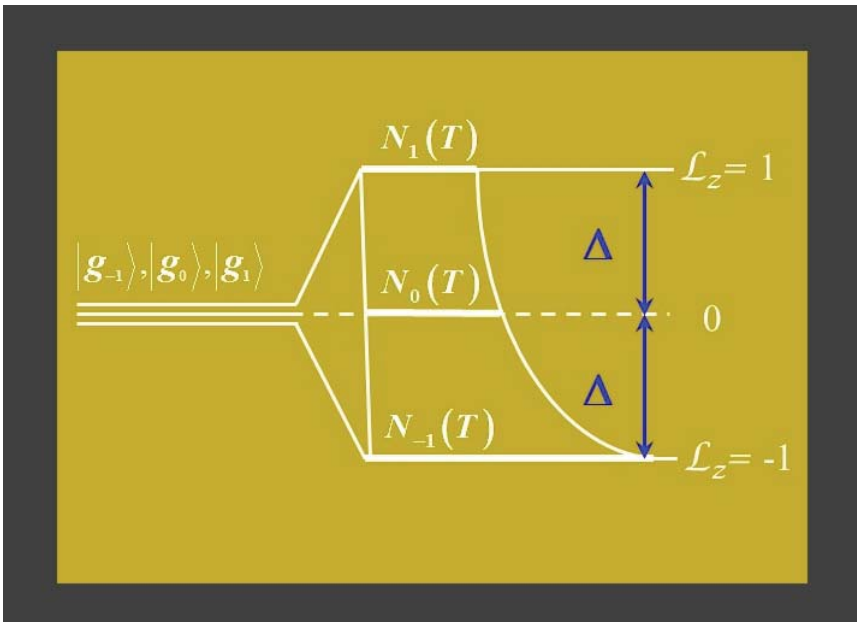

Figure 2.7 In paramagnetic transition, spin-orbit split ground state depends on temperature to define the population densities for distinctive RCP and LCP absorption.

diagonal tensor element for Bi: YIG. Therefore, the FR in Bi: YIG is assumed to result primarily from the diamagnetic transition. Most of the magneto-optical enhancement across a band from 2 to 5 eV in Bi:YIG are considered to stem from the two strong absorption lines with transition energies of 2.6 and 3.15 eV, taking place due to the Fe^{3+} ions in the tetrahedral d and octahedral a sublattices as shown in Figure 2.8. A third transition at 3.9 eV from the tetrahedral d sublattice similar to sign and proportions to the one at 2.6 eV is also responsible for the large FR in Bi: YIG.

FR in YIG and Bi: YIG materials are small at far infra-red (IR) frequencies compared to that at UV and optical frequencies. However, the same optical transitions described in the previous paragraph of this section are also responsible for the magneto-optic effect at far IR frequencies in these materials. It is important to mention here that there is no absorption of electromagnetic intensity by these materials at IR frequencies. Therefore, the FR in YIG and Bi: YIG at these frequencies can be explained using the Kramers-Kronig identity relations. In a material dielectric tensor, the Kramers-Kronig identity relates the real and the imaginary parts of a complex dielectric permittivity component. Here, all the dielectric components in the tensor are frequency dependent. A ω_0 frequency dependent complex

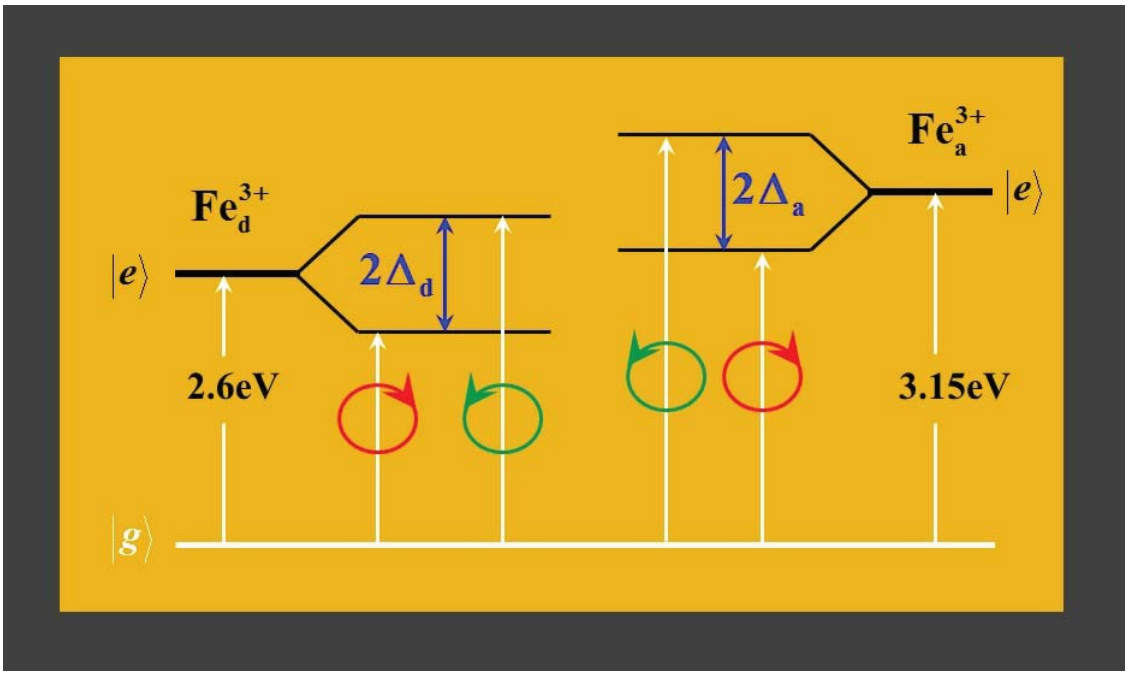

Figure 2.8 Diamagnetic transitions at optical energies 2.6 eV and 3.15 eV for tetrahedral and octahedral Bi: YIG crystal sublattices are majorly responsible for the observed magneto-optic effect in Bi: YIG.

dielectric permittivity relation can be written as

$$\varepsilon(\omega_0) = \varepsilon'(\omega_0) + \varepsilon''(\omega_0)\,, \tag{2.14}$$

where $\varepsilon'(\omega_0)$ and $\varepsilon''(\omega_0)$ are the real and imaginary parts of the dielectric permittivity. It is worth mentioning here that the real and the imaginary dielectric parts measure the refractive index and absorption of a medium at a particular frequency. The Kramers-Kronig relations, which relate the real and the imaginary parts of the permittivity of a medium, can be written as

$$\varepsilon'(\omega_0) = \frac{2\mathrm{P}}{\pi}\int_0^{\infty} \frac{\omega\varepsilon''(\omega)}{\omega^2 - \omega_0^2} d\omega \tag{2.15}$$

$$\varepsilon''(\omega_0) = -\frac{2\mathrm{P}}{\pi}\int_0^{\infty} \frac{\omega\varepsilon'(\omega)}{\omega^2 - \omega_0^2} d\omega\,, \tag{2.16}$$

where P denotes the Cauchy principal value. Given the real or imaginary part of $\varepsilon(\omega)$ for all frequencies ω, these powerful formulas allow the complementary component to be determined at a particular frequency ω_0. By this logic, the absorptions happening in the UV and visible range of frequencies in YIG and Bi: YIG are considered to be responsible for the identified FR at IR frequencies.

2.4 Growth and characterization of iron garnet films

Iron garnet film growth techniques include: liquid phase epitaxy (LPE), reactive ion beam sputtering (RIBS), pulsed laser deposition (PLD), metal organic chemical vapor deposition (MOVCD), radio-frequency sputtering (RFS), and electron cyclotron resonance sputtering (ECRS). Among all these available growth techniques, LPE is one of the widely used technique for growing iron garnet due to its capability of producing high quality mono-crystal films. Film with microns of thickness can be very easily grown without losing the uniform crystallinity in the film with this technique. Similar to growth techniques, characterization of iron garnet film also involves various techniques, including, but not limited to, transmission- and reflection- ellipsometry for film thickness, refractive index, absorption characterization, X-ray diffraction (XRD) for crystallinity check, Rutherford backscattering (RBS) for compositional analysis, Micro-Raman analysis for vibrational studies, field emission scanning electron microscopy (FESEM) for imaging and energy dispersive analysis, transmission electron microscopy (TEM) for determination of crystal structure, etc. Below, the LPE grown method and some of the characterization techniques for iron garnet film are described in two sub-sections of this section to relate the work presented in chapter 4.

2.4.1 Liquid phase epitaxy (LPE)

Iron garnet films used for this dissertation work are grown by liquid-phase-epitaxy and therefore, they are mono-crystalline and already in the garnet phase as grown. They are grown in a melt and, unlike sputter-deposited films, do not require annealing to crystallize or to form a garnet phase. In this method, a single crystal GGG substrate is submerged into

a supersaturated, metastable melt flux. The substrate is first lowered close to the melt and allowed to equilibrate its temperature with that of the melt, and then dipped slowly into the melt and allowed to rotate with a constant rate. The growth conditions for the film remain unchanged and always stay optimal during the whole of the growth process. The rate of rotation of the substrate also remains constant during growth. Temperature variation during growth process may be only 0.5 degrees centigrade, which eliminates the chance of composition irregularity in the film. In the completion of the growth process, the substrate attached with the melt is pulled out just above to the melt and rotated again to remove excess melt. From here, substrate with the melt is allowed to cool down to the ambient temperature through a slow cooling process. Undercooling steps avoid the cracking and stoichiometry change in the film. Therefore, film thickness and stoichiometry of the iron garnet film is mainly controlled by the rotation speed and undercooling conditions in the LPE technique.

2.4.2 Film characterization

The dissertation work presented in chapter 4 uses reflection ellipsometry for accurate iron garnet film thickness measurement, and RBS analysis for compositional analysis. The method involving these measurements are described in this sub-section.

In reflection ellipsometry, a V-Vase ellipsometer, an instrument used for this dissertation work, measures the outgoing elliptical polarization against the incident linear polarization reflected from a sample surface as shown in Figure 2.9. In general, ellipsometeric measurement involves the determination of two parameters: ψ and Δ, where ψ represents the orientation of the elliptical polarization and Δ is the phase lag between the orthogonal components of the measured output. By measuring these values, the Instrument actually measures the ratio between Fresnel's reflection coefficients $\tilde{R}_p$ and $\tilde{R}_s$ for the p- and s- polarizations of the output light wave as

$$\tan(\psi)\exp((i\Delta) = \frac{\tilde{R}_p}{\tilde{R}_s} . \qquad (2.17)$$

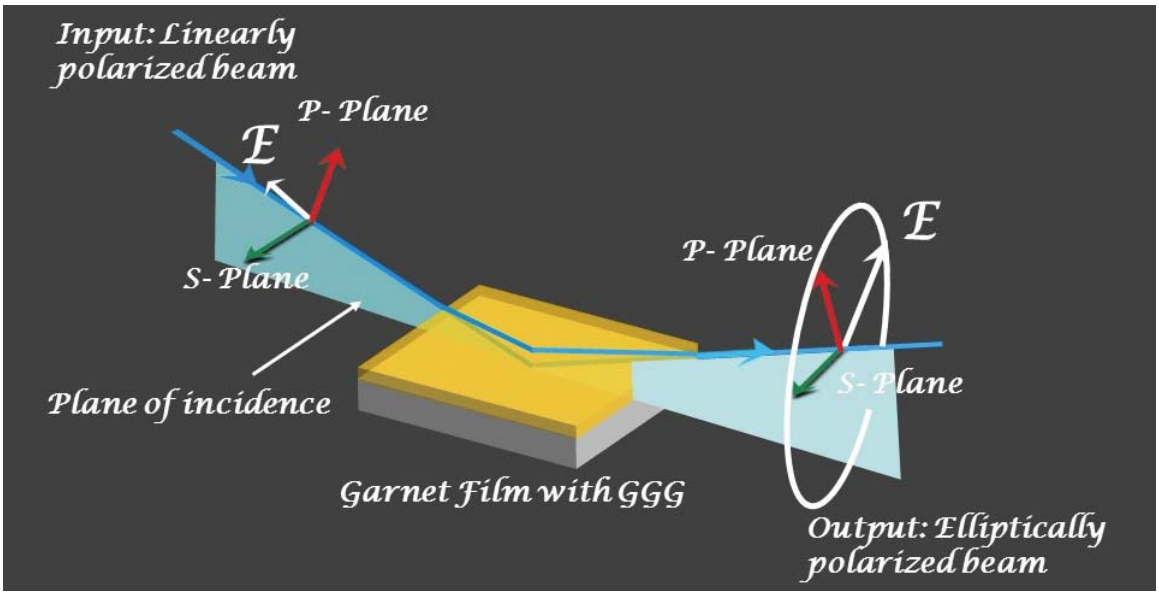

Figure 2.9 Ellipsometer measures sample reflected output elliptical polarization against the input linear polarization to determine certain optical parameters of the garnet films.

Now, in a sample with two interfaces, for example film-air and film-substrate in the Bi: YIG film with GGG substrate, the electromagnetic wave undergoes multiple reflections from these interfaces and creates a path difference between the incoming and the outgoing wave. Fresnel's reflection coefficients from Eq. (2.17) measures this path difference β' for the electromagnetic wave with angle of incidence ϕ and wavelength λ as

$$\beta' = 2\pi\tilde{n}\frac{d}{\lambda}\cos(\phi), \tag{2.18}$$

where d is the film thickness and $\tilde{n}$ is the complex index of reflection of the film. Therefore, ψ and Δ indirectly measure the path difference between the incident and reflected electromagnetic waves and thereby the thickness of a film. To extract the information about film thickness, ψ is only measured for a range of wavelengths, where there is no absorption of the electromagnetic wave by the sample. In that case, path difference of the film from Eq. (2.18) only depends on the wavelength because $\tilde{n}$ is real and can be assumed as constant. As this path difference acts like a positive integer analogous to Bragg's law in crystallography, it repeats its value after certain values of wavelength. This makes ψ to be sinusoidal in the measured wavelength range. Curve fitting on this

measurement using Lorentz, Gaussian or Tauc-Lorentz functions determines the desired film thickness of a sample. Accuracy of the measurement can be improved by measuring ψ for different incidence angles of the electromagnetic wave.

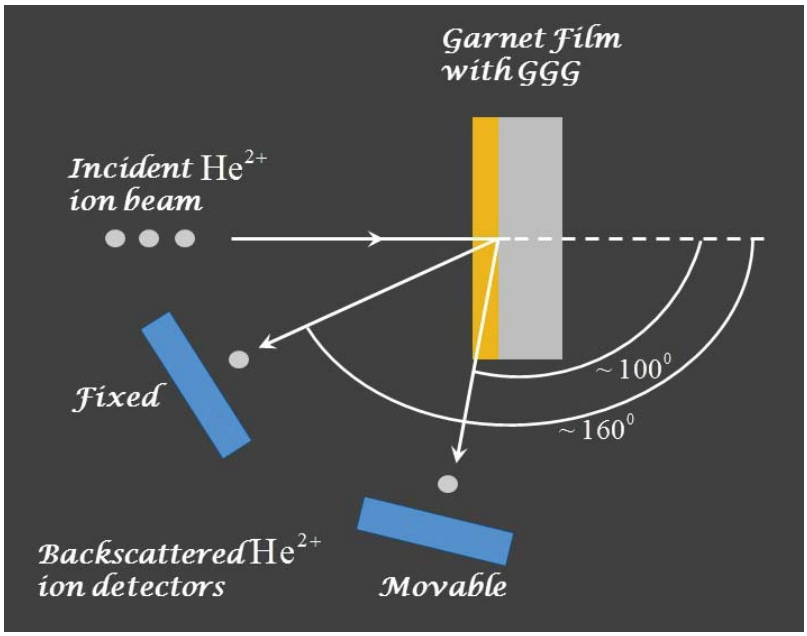

Figure 2.10 RBS measurement uses two detectors to collect the energy spectrum for backscattered He^{2+} ions to determine the composition of a garnet film.

In RBS measurements, a He^{2+} ion beam with 2.275 MeV energy is targeted to a sample of garnet film with GGG substrate at its back. In the process of the experiment, some of the ions penetrate the sample and some are backscattered. To perform the compositional analysis of garnet film used in this dissertation, the RBS experiment uses two detectors: one is fixed at a position near to the incident beam to collect the normally scattered He^{2+} ions and the other detector moves in a plane as shown in Figure 2.10. Both the detectors here are engaged to measure the backscattered He^{2+} ion beam energy during the course of the experiment. Recorded energy spectra by the two detectors are then analyzed using a theoretical layer model to calculate elemental composition of the desired film. RBS can also provide information about the film thickness; however, accuracy is poor, as measurement assumes the film densities.

Chapter 3

Optical Waveguides and Bragg-Gratings

This chapter discusses the general theories of waveguide modes and their transport mechanisms through a wavelength-comparable optical waveguide structure. The confined propagation of electromagnetic radiation with a transverse dimension defined by the waveguide structure is regarded as a "guided mode." The fundamental properties of a guided wave can be studied by solving Maxwell's equations subject to the waveguide geometry-imposed boundary conditions. To discuss the confined propagation of guided modes, a slab dielectric waveguide geometry is used. In this discussion, TE and TM modes are derived for such geometry and explained using the principle of total internal reflection of plane waves from the dielectric interfaces. Furthermore, the coupling of these modes in a waveguide with Bragg-gratings is discussed using coupled mode theory. Finally, wave-propagation characteristics in the PBG of a magneto optic media are discussed in context to support the discussion in chapter 5.

3.1 Properties of Optical Waveguides

The general requirement of an optical waveguide is that there should be a guiding region with a higher refractive index than elsewhere to transport the electromagnetic radiation only through the structure but not perpendicular to it. Generally, thin films deposited on transparent dielectric substrate serve the purpose of a guiding region in a basic optical waveguide provided film index is higher than the substrate. Figure 3.1(a) shows schematic of a basic step index type lossless waveguide structure with a distinct refractive index profile (Figure 3.1(b)) that includes cladding, guide, and substrate layers. An optical wave can be regarded as a guided wave in this structure if it propagates only in the film region. Here, the film thickness 'd' is engineered to be greater than a critical thickness value, above which the film can confine the optical wave and allow it to propagate.

A guided optical wave in the slab waveguide structure illustrated in Figure 3.1(a) exists when incoming coherent light rays undergo multiple total internal reflections at the slab

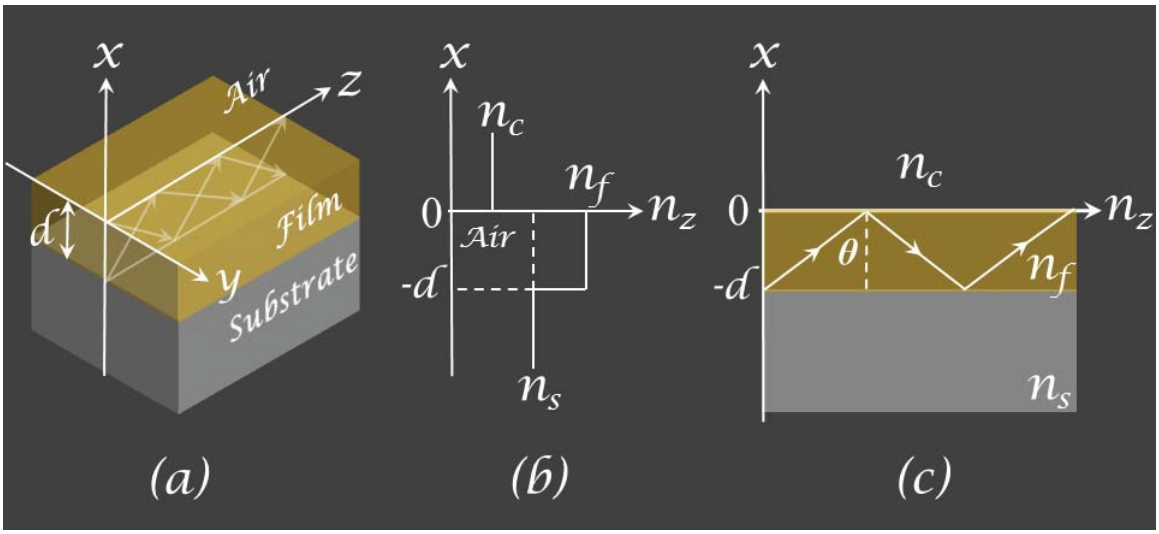

Figure 3.1 (a) Basic step-index type waveguide with (b) refractive index profile of cladding (air), film and substrate layers for (c) guided wave propagation.

boundaries without a loss of power and propagate in the *z* direction. The possibility of the absence of power loss through the waveguide structure depends on the incident angle of the incoming light rays. The incident angle 'θ' in Figure 3.1(c) must meet the critical condition $\theta_s<\theta< 90°$ for total confinement of the light wave inside the guiding layer, where θ_s is a critical angle. The value of θ_s is determined using the film and substrate refractive indices, and is given by:

$$\theta_s = \sin^{-1}\left(\frac{n_s}{n_f}\right). \tag{3.1}$$

There is another critical angle associated with the cladding-film interface, θ_c, which is used to determine likelihood of leakage through the cladding layer. This angle is always smaller than $\theta_s$for an asymmetric waveguide structure, and is given by:

$$\theta_c = \sin^{-1}\left(\frac{n_c}{n_f}\right). \tag{3.2}$$

3.1.1 Waveguide Modes

A waveguide mode in a waveguide structure can be studied using wave nature of light. In

a homogenous lossless linear medium, waveguide modes can be achieved by solving Maxwell's equation inside this medium. Here, eigen-solutions of the source-free Maxwell's equation constitute the waveguide modes of a dielectric waveguide. There can be two types of solutions to the Maxwell's equation in a slab waveguide structure, depending upon the polarization state of the propagating optical wave; these are either transverse electric (TE) or transverse magnetic (TM) waveguide modes.

Maxwell's equation in lossless linear dielectric media can be given by

$$\nabla \times \mathbf{E} = -\mu \frac{\partial \mathbf{H}}{\partial t} \tag{3.3}$$

$$\nabla \times \mathbf{H} = \varepsilon \frac{\partial \mathbf{E}}{\partial t} \tag{3.4}$$

where μ and ε are dielectric permeability and permittivity of the media, respectively, and **E** and **H** are the electric and magnetic field vectors associated with the propagating wave inside the dielectric media, also respectively.

Optical modes in a waveguide structure can be described using the plane wave equation. A wave inside a waveguide structure such as that described in Figure 3.1(a) propagating in the *z* direction can be described by this set of equations:

$$\mathbf{E} = \mathbf{E}(x, y)\exp\left[i(\omega t - \beta z)\right] \tag{3.5}$$

$$\mathbf{H} = \mathbf{H}(x, y)\exp\left[i(\omega t - \beta z)\right] \tag{3.6}$$

where $i = \sqrt{-1}$, ω is the angular frequency, and $\beta = k_0 N = k_0 n_f \sin\theta$ is the propagation constant.

Using Eq. (3.3) – Eq. (3.6), the TE and TM mode equations of the waveguide structure in Figure 3.1(a) can be written as

$$\frac{\partial^2 E_{x,y}}{\partial x^2} + \left(k_0^2 n^2 - \beta^2\right) E_{x,y} = 0, \tag{3.7}$$

$$\frac{\partial^2 H_{x,y}}{\partial x^2} + \left(k_0^2 n^2 - \beta^2\right) H_{x,y} = 0, \tag{3.8}$$

where $k_0 = \omega/c$ and c is the velocity of light in the vacuum.

To describe characteristics of the respective modes, it is useful to understand the physical nature of the solutions for Eq. (3.7) and Eq. (3.8) in the clad, film, and substrate regions of a slab waveguide structure. Due to similarities in the characteristics between TE- and TM–mode waves, a discussion of only TE characteristics is presented here. Considering the nature of the solutions as a function of the propagation constant β at a fixed frequency ω, the waveguide mode characteristics can be described for the propagation constant regimes (a), (b), (c) and (d) as shown in Figure 3.2.

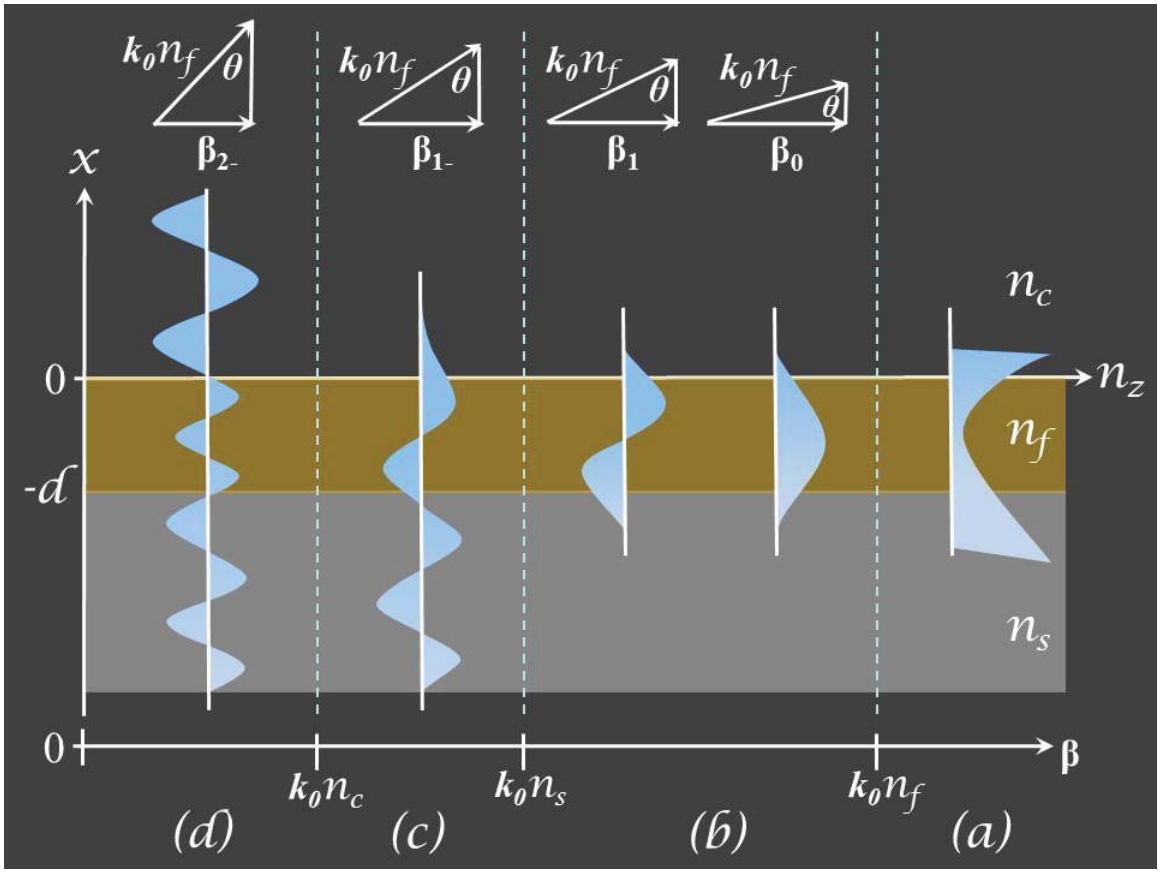

Figure 3.2 In different propagation constant regimes (a), (b), (c) and (d), propagation triangles (top), and corresponding mode profiles (middle) of different modes with β_0, β_1, β_{1-}, β_{2-} propagation constants in the step index type waveguide structure.

TE mode characteristics can be well understood by re-writing Eq. (3.7) for clad, film and substrate regions as

Clad: $$\frac{\partial^2 E_{x,y}}{\partial x^2} + \left(k_0^2 n_c^2 - \beta^2\right) E_{x,y} = 0 \quad , \qquad (3.7\text{–}1a)$$

Film: $$\frac{\partial^2 E_{x,y}}{\partial x^2} + \left(k_0^2 n_f^2 - \beta^2\right) E_{x,y} = 0 \quad , \qquad (3.7\text{–}1b)$$

Substrate: $$\frac{\partial^2 E_{x,y}}{\partial x^2} + \left(k_0^2 n_s^2 - \beta^2\right) E_{x,y} = 0 \quad . \qquad (3.7\text{–}1c)$$

Regime (a): In this regime, $\beta > k_0 n_f$. Therefore, $\left(1/E\right)\left(\partial^2 E/\partial x^2\right) > 0$ everywhere, and $E\left(x\right)$ is exponential in all clad, film, and substrate regions of the waveguide. Since the field distribution is unbounded to the waveguide as seen in Figure 3.2(a), the solution to Eq. (3.7.1) does not correspond to a real wave.

Regime (b): In this regime, $k_0 n_s < \beta < k_0 n_f$. Therefore, $\left(1/E\right)\left(\partial^2 E/\partial x^2\right) < 0$ in the film region, and the solution to Eq. (3.7.1) is sinusoidal as seen in Figure 3.2(b). In the clad and substrate regions, $\left(1/E\right)\left(\partial^2 E/\partial x^2\right) > 0$, and hence the solution exponentially decays in these regions. The energy carried in these different modes is confined to the film region, and is thus regarded as "guided modes." Propagation constants of these modes are β_0 and β_1, belonging to the fundamental and first-order TE waveguide transmission modes, respectively, and can be seen and this can be seen from the propagation triangle schematics presented in Figure 3.2(b).

Regime (c): In this regime, $k_0 n_c < \beta < k_0 n_s$, and therefore $\left(1/E\right)\left(\partial^2 E/\partial x^2\right) < 0$ in the film and substrate regions, and the solution to Eq. (3.7.1) is sinusoidal, as seen in Figure 3.2(c). In the clad region, $\left(1/E\right)\left(\partial^2 E/\partial x^2\right) > 0$ and so the solution exponentially decays in this region. The energy carried by the waveguide in this mode is radiated through the substrate, and so this regarded as the "substrate radiation mode." In Figure 3.2(c), β_1- represents the propagation constant for the first order substrate radiation mode. From the

propagation triangle schematic, it is clear that the radiation mode depends on the angle of incident of the coherent incoming beam to the waveguide.

Regime (d): In this regime, $0 < \beta < k_0 n_c$, and therefore $(1/E)\left(\partial^2 E/\partial x^2\right) < 0$ in all clad, film, and substrate regions, and the solution for $E(x)$ in Eq. (3.7.1) becomes sinusoidal as seen in Figure 3.2(d). These are the so-called "waveguide radiation modes." In Figure 3.2 (d), β_2- represents the propagation constant for the second-order TE radiation mode.

3.1.2 Dispersion of modes in Asymmetric Waveguide

Waveguide geometry induces dispersion among the TE and TM modes of a slab waveguide structure in Figure 3.1(a). The dispersion relation for TE modes can be obtained by applying the boundary conditions to the field solutions of Eq. (3.7.1) and can be given by

$$k_x d = (m+1)\pi - \tan^{-1}\left(k_x/\gamma_s\right) - \tan^{-1}\left(k_x/\gamma_c\right), \tag{3.9}$$

where $k_x = k_0\sqrt{n_f^2 - N^2}$, $\gamma_s = k_0\sqrt{N^2 - n_s^2}$, and $\gamma_c = k_0\sqrt{N^2 - n_c^2}$.

Similarly, from Eq. (3.8), TM mode dispersion relation can be obtained as

$$k_x d = (m+1)\pi - \tan^{-1}\left(\left(k_x/\gamma_s\right)\left(n_s/n_f\right)^2\right) - \tan^{-1}\left(\left(k_x/\gamma_c\right)\left(n_c/n_f\right)^2\right). \tag{3.10}$$

In Eq. (3.9) and Eq. (3.10), $m = 0, 1, 2, 3.....$ represent different waveguide modes.

For example, on an iron-garnet film ($Bi_{0.8}Gd_{0.2}Lu_2Fe_5O_{12}$) on $Gd_3Ga_5O_{12}$ (GGG) substrate, the dispersion characteristics of the TE and TM modes can be calculated using Eq. (3.9) and Eq. (3.10), and can be plotted as shown in Figure 3.3. Parameters used for the calculation are as follows: cladding layer = air, $Bi_{0.8}Gd_{0.2}Lu_2Fe_5O_{12}$ film index = 2.29, GGG substrate index = 1.94, operating wavelength = 1543 nm. At this wavelength, the cut-off film thickness to support single TE and TM waveguide modes are 188.4 nm and 287.0 nm, respectively. A change in wavelength from infrared to visible light at 633 nm lowers the cut-off film thickness to 58% of the previous value. Therefore, to measure the mode

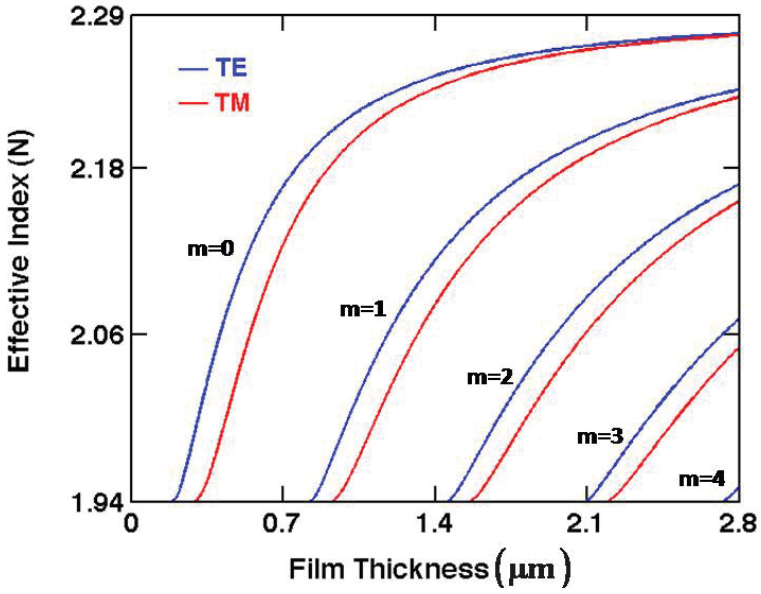

Figure 3.3 Calculated TE and TM modes for $Bi_{0.8}Gd_{0.2}Lu_2Fe_5O_{12}$ film/ GGG substrate at 1543nm wavelength and m = {0, 1, 2, 3, and 4}.

and thickness of an ultrathin film, waveguide mode measurement is done at a lower wavelength.

3.1.3 Mode Index and Thickness Measurements

Experimentally, mode refractive index and film thickness can be measured using the "prism-coupler" technique. The working principle behind the prism-coupler technique is as follows: the mode index and film thickness on a glass sample is measured using a symmetric prism mounted on a computer-driven rotary table. The rotary table varies the angle incidence of the laser beam striking the prism, and is able to locate film propagation modes. A pneumatically-operated coupling head presses the glass sample to be measured (Figure 3.4) against the base of the prism and creates a small air gap between the film and the prism. Millimeter-thick glass samples are useful here, as these samples are slightly flexible and yield elastically under the clamping pressure from the pneumatic head.

Normally, a laser beam transmitted through the air penetrates the prism, strikes its base, and reaches a photo-detector after total internal reflection. Laser light intensity drops sharply for certain incident angles. These are called "mode angles," as light tunnels through the air gap and couples to the film and is guided in the film for optical propagation.

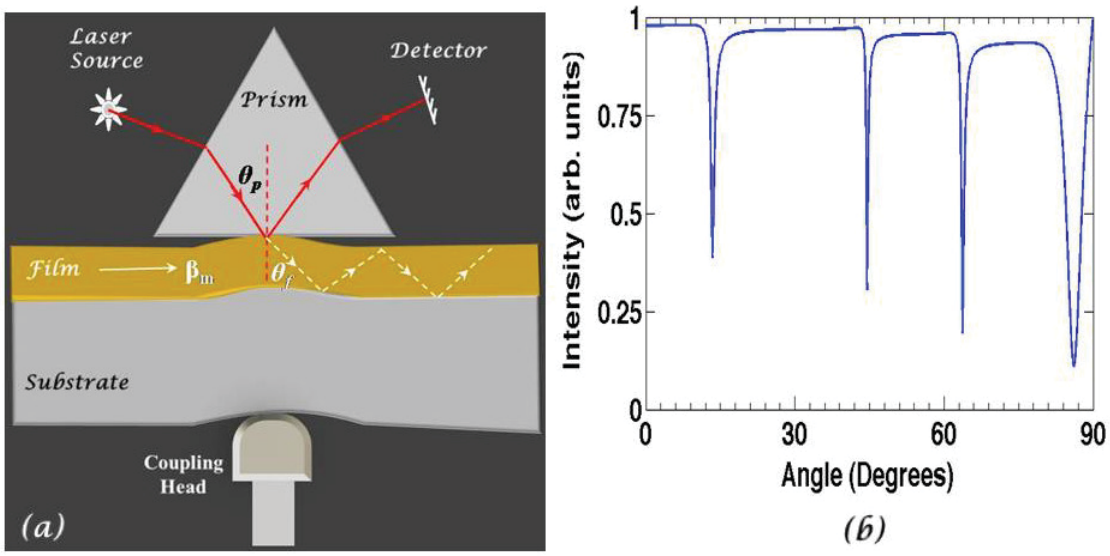

Figure 3.4 (a) Prism-coupler measures the (b) intensity dips at various prism angles (θ_p) to determine the modes from a slab waveguide.

When two of the mode angles are found, the film thickness and mode index are computed by following TE and TM dispersion equations as described in Eq. (3.9) and Eq. (3.10). The mode and film thickness computation depends on operating wavelength, substrate refractive index, and prism refractive index respectively. A prism with high refractive index is typically used to measure the mode indices from thinner films.

3.2 Bragg-Gratings on Ridge Waveguide

A ridge waveguide structure consists of a slab waveguide with a strip superimposed onto it. To fabricate this type of waveguide structure, the surface of a slab waveguide is modified using techniques called photolithography and dry plasma etching. The resulting strip is an integral part of the film, as can be seen in the schematic shown in Figure 3.5. Typical photolithography steps involved in the fabrication of the ridge waveguide structures are substrate cleaning; photo-resist layer formation by spinning; soft baking; mask alignment; UV exposure and development; and hard-baking as shown in the cross-section schematic (a), (b), (c) and (d) respectively in Figure 3.6. High-density argon plasma treatment to the photo-resist layer coated film in Figure 3.6 (d) etches the film from the exposed regions as can be seen in the Figure 3.6(e). After plasma exposure, the film is rinsed into the required chemical solution to erase the left-over photo-resist (Figure 3.6 (f))

and the final product can be seen as fabricated ridge waveguide structures onto the slab film.

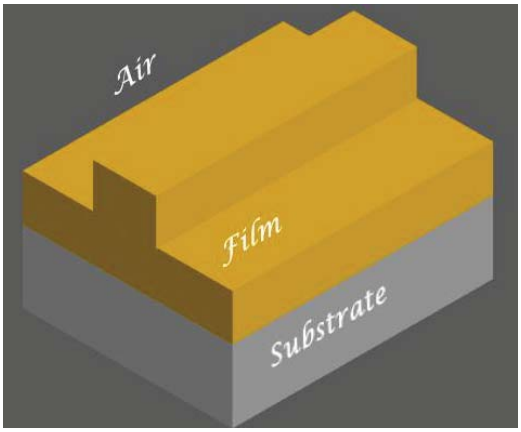

Figure 3.5 Ridge waveguide schematic

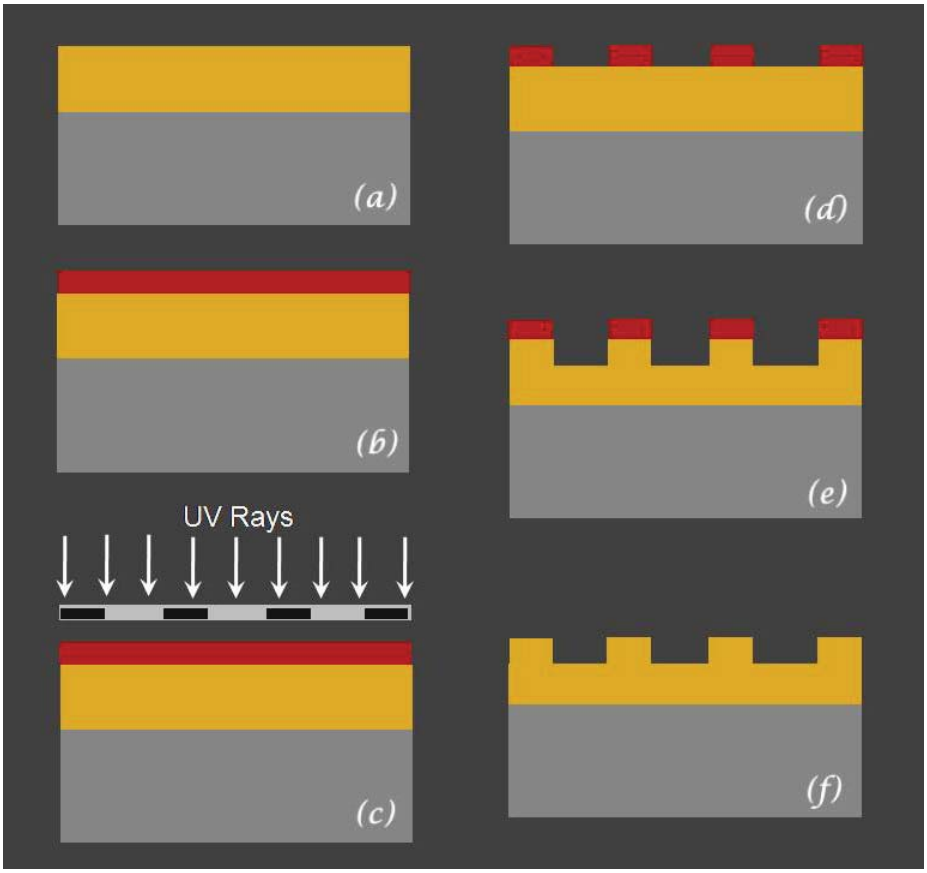

Figure 3.6 Fabrication of ridge waveguide requires optical photolithography steps: (a) sample cleaning (b) photo-resist coating (c) Ultra-Violet ray exposure (d) photo-resist development. Following lithography, dry etching using plasma treatment produces (e) slab film with strip patterns and creates the (f) ridge waveguide structures.

The fabrication of Bragg gratings on a ridge waveguide uses a technique called focused ion beam (FIB) milling. In general, FIB uses gallium ions to mill micro- or nanostructures. Heavy Ga^+ ions bombard a sample surface thus ejecting material from the sample and creating the desired pattern. To fabricate 1D Bragg gratings, the pattern is first drawn in 2D-design CAD, and later translated onto the sample surface using nano pattern generation system (NPGS) software to guide the FIB beam accordingly. The schematic of 1D Bragg gratings can be seen in Figure 3.7 as a periodically varying refractive index structure where alternating layers of material and air coexist. Bragg gratings function as perfect mirrors, and also known as 1D photonic crystals. In presence of the Bragg gratings, optical waves propagating through the ridge waveguide structure are subjected to the refractive index change and undergo Bragg reflection. In the Bragg reflection process, a forward propagating wave interacts with the backward-reflected wave through a phase matching mechanism. This phase matching condition depends on the grating's period, shown in the highlighted portion of the schematic in the Figure 3.7.

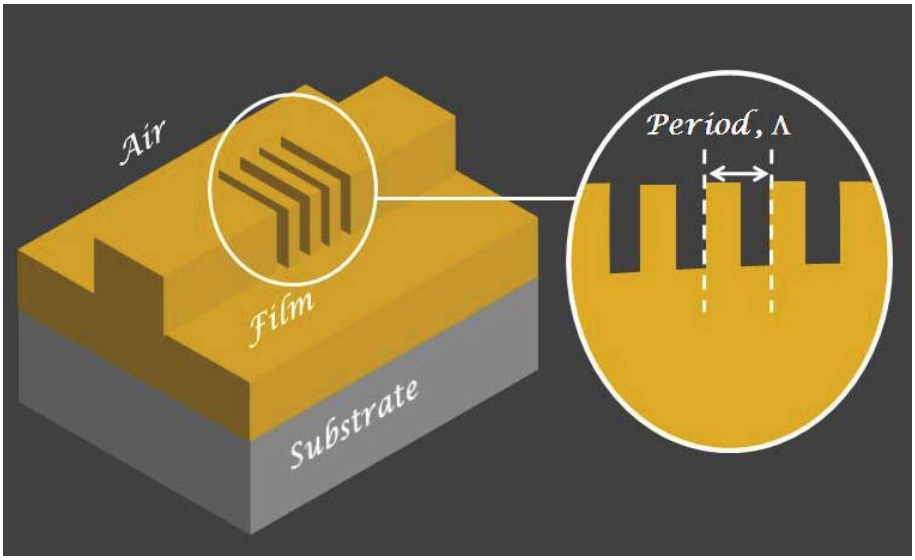

Figure 3.7 Bragg gratings on a ridge waveguide structure

3.2.1 Mode Coupling due to Dielectric Perturbation

In Bragg gratings, a forward-propagating wave couples to a back-reflected wave due to the surface corrugation of the waveguide structure. In this case, there is a dielectric

perturbation $\Delta\varepsilon(x,y,z)$ due to the surface corrugation which facilitates the coupling between waveguide modes of different orders. In the ridge waveguide structure, the fundamental waveguide mode couples to all higher order waveguide modes in the presence of Bragg gratings. The dielectric tensor as a function of space for a ridge waveguide structure can be written as

$$\varepsilon(x,y,z)=\varepsilon_0(x,y)+\Delta\varepsilon(x,y,z), \tag{3.11}$$

where $\varepsilon_0(x,y)$ is the unperturbed dielectric function describes the waveguide structure.

Here, the dielectric perturbation $\Delta\varepsilon(x,y,z)$ is periodic in z, therefore it can be expanded into a Fourier series as

$$\Delta\varepsilon(x,y,z)=\sum_{l\neq 0}\varepsilon_l(x,y)\exp\left[-il\frac{2\pi}{\Lambda}z\right], \tag{3.12}$$

where the summation is over all $\boldsymbol{l}$ except $\boldsymbol{l=0}$ because if the $\varepsilon(x,y,z)$ from Eq. (3.11) is expanded into a Fourier series then $\varepsilon_0(x,y)$ serves the zeroth component of the series.

Now, a propagating wave through a ridge waveguide with Bragg gratings can be expressed as the linear combination of all the waveguide modes of the ridge waveguide

$$\mathbf{E}=\sum A_m(z)E_m(x,y)\exp\left[i(\omega t-\beta_m z)\right], \tag{3.13}$$

where $A_m(z)$ are the waveguide mode amplitudes which depend on z.

The waveguide modes are mutually orthogonal and satisfy the following orthonormality condition [78]:

$$\langle m|k\rangle=\int E_m^*\cdot E_k\,dxdy=\frac{2\omega\mu}{|\beta_k|}\delta_{km}\ . \tag{3.14}$$

By applying Eq. (3.12), Eq. (3.13) and Eq. (3.14) to the wave equation

$$\left[\nabla^2+\omega^2\mu\left\{\varepsilon_0(x,y)+\Delta\varepsilon(x,y,z)\right\}\right]E=0, \tag{3.15}$$

the coupled-waveguide mode equation may be derived

$$\frac{d}{dz}A_k(z) = -i\frac{\beta_k}{|\beta_k|}\sum_m\sum_l C_{km}^{(l)}A_m(z)e^{i(\beta_k-\beta_m-l2\pi/\Lambda)z}, \quad (3.16)$$

where the measure of spatial overlapping of two counter propagating waveguide modes due to the dielectric perturbation $\Delta\varepsilon(x,y,z)$ is given by the coupling coefficient:

$$C_{km}^{(l)} = \frac{\omega}{4}\langle k|\varepsilon_l|m\rangle = \frac{\omega}{4}\int E_k^* \cdot \varepsilon_l(x,y)E_m dxdy. \quad (3.17)$$

For significant mode coupling between modes ***k*** and ***m*** in a perturbed ridge waveguide structure, two conditions must be satisfied.

Condition I: There should be **a phase match** between the modes

$$\beta_k - \beta_m - l\frac{2\pi}{\Lambda} = 0. \quad (3.18)$$

This condition is also known as the Bragg's reflection condition.

Condition II: There should be a **non-vanishing coupling coefficient,**

$$C_{km}^{(l)} \neq 0. \quad (3.19)$$

It is important to mention here that the described mode coupling occurs either between TE modes or TM modes. There is no mode coupling between TE to TM modes because in the corrugation function, $\Delta\varepsilon(x,y,z) = \varepsilon_0\Delta n^2(x,y,z)$, $\Delta n^2(x,y,z)$ is a scalar quantity.

3.2.2 Photonic Bandgap and stopband

The dispersion of waveguide modes in a ridge waveguide structure plays a crucial role in the formation of photonic bandgaps in the ridge waveguide with 1D Bragg gratings. Photonic bandgap formation takes place here through the contra-directional coupling between the two forward- and back-reflected waveguide modes. Guided mode dispersion and the formation of an optical bandgap can be understood using a Brillouin zone picture. Dispersion of TE and TM guided modes in a ridge waveguide structure can be described

using the Brillouin diagram in Figure 3.8(a). All guided modes from Figure 3.3 can be placed into the 1st Brillouin zone, and their coupling due to the presence of Bragg gratings can be explained in this way.

An optical mode with propagation vector β_m that couples through a phase-matching condition to another optical mode β_k within a Bragg grating is well described in Eq. (3.18). An optical wave incident to a grating with a spatial dependence of $\exp\left(-i\overline{\beta}.\overline{r}\right)$ can have wave components in the grating region described by the propagation vectors $\overline{\beta}+l\overline{K}$,

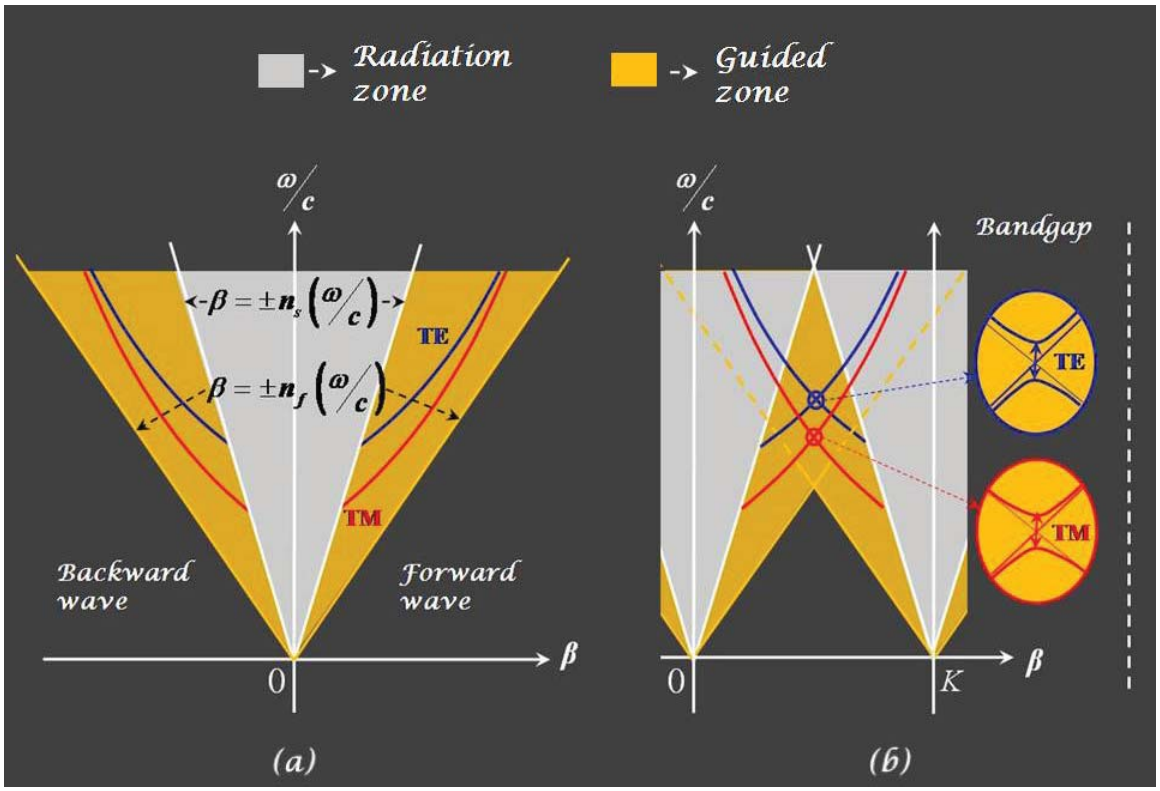

Figure 3.8 Brillouin diagrams for (a) guided mode dispersion in a ridge waveguide structure and (b) optical bandgaps due to contra-directional coupling in ridge waveguide with 1D Bragg gratings.

$\overline{K}=2\pi/\Lambda\,\hat{z}$. These are termed "space harmonics." Space harmonics are produced due to the result of phase modulation $\Delta\varepsilon\left(x,y,z\right)$, and can propagate in a waveguide structure due to the phase matching condition in Eq. (3.18). Here, l is the order of coupling. The 1st Brillouin zone and 1st order space harmonic in Figure 3.8(b) yielded by 1D Bragg gratings in a ridge waveguide structure can be obtained by shifting the curves in Figure

3.8(a) by an amount $\left|\overline{K}\right|$ along the β axis. Due to phase matching, the coupling between TE-TE and TM-TM modes occurs in the vicinity of the intersection of the incident forward mode and space harmonic-generated mode waves, as can be seen in the Figure 3.8(b). Here, the coupling of different modes produces interference, and the original mode curves become folded and separated into upper and lower curves. The gap between these curves is the so-called "1D photonic bandgap." In this bandgap, no optical wave may propagate in the forward direction, as β is imaginary, and hence an optical "stop band" appears.

3.3 Direct End Coupling – Mode Excitation

The simplest method for guided mode excitation in a waveguide structure is the direct end coupling method. In this method, light with a profile similar to a guided mode wave is fed normal to a waveguide end-face to induce guided wave propagation. As discussed earlier in section 3.1.2, an optical wave propagates in a waveguide structure in the form of modes. Therefore, an incident optical wave from an optical fiber to a ridge waveguide structure like that in Figure 3.9 can be considered as a superposition of these modes.

In general, an optical source $S(y)$ has arbitrary optical distribution profile and is therefore capable of exciting different waveguide modes in a waveguide structure

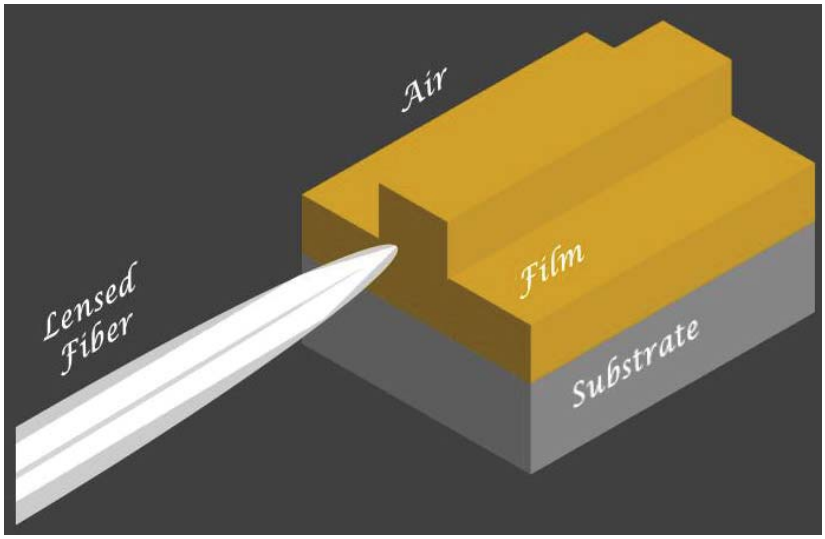

Figure 3.9 Optical wave coupling from a fiber to a ridge waveguide structure through Direct Coupling Method.

depending on the externally impressed conditions. The power transfer from the source to mode m depends on the degree of similarity between the source $S(y)$ and modes $u_m(y)$. Fiber coupling is referred to as "pig-tailing" and is a common strategy to achieve direct coupling. To achieve high efficiency, profile matching should be satisfied between the fiber input and guided waves by adjusting the positions of the components. Also, efficiency can be enhanced by minimizing the Fresnel reflection loss by using an antireflection coating, or by filling the gap between the fiber and the waveguide structure.

Chapter 4

Magneto-Optic Interactions in Ultra-thin Garnet Films

In magneto-optic media, linearly polarized light exhibits Faraday rotation during magnetization along the direction of light propagation. Bismuth-substituted rare-earth iron garnet films show a strong magneto-optical response, as the right and the left circularly polarized lights are differently absorbed at wavelengths shorter than the probe wavelength (Kramer-Kronig). This difference in the absorption is mainly due to the different electronic dipole transitions from the singlet ground state to the spin-orbit split excited states of Fe^{3+} ions in the sublattices of the Bi: YIG material. This part of the dissertation addresses a different kind of mechanism of increase in Faraday rotation from the Bi: YIG based film. The findings discussed in this chapter were published in the journal[1] Appl. Phys. Lett. 107, 011104 (2015).

LPE-grown mono-crystal $Bi_{0.8}Gd_{0.2}Lu_2Fe_5O_{12}$ on $Gd_3Ga_5O_{12}$ films are used for the investigation to determine the FR enhancement from such films. These single-layer bismuth-substituted-rare-earth iron-garnet films were grown by liquid-phase-epitaxy (LPE) on (100) gadolinium gallium garnet (GGG) substrates. In this chapter, total four sections are included to present the FR enhancement study in $Bi_{0.8}Gd_{0.2}Lu_2Fe_5O_{12}$ films. The first section, titled "Instruments and garnet thin film characterization," includes: ultra-sensitive FR measurement setup development, preparation method of thin film samples, thickness characterization of thin films, and the MCD measurement set-up. Section two, "Measurements on garnet films," discusses the specific FR, MCD and Kramer's Kronig analysis; RBS analysis; and micro-Raman analysis performed on $Bi_{0.8}Gd_{0.2}Lu_2Fe_5O_{12}$ films. A separate subsection of errors in measurement is also included in the second section. The third and final section, "Theoretical analysis of garnet films," is presented to support the experimental findings in the preceding sections.

---

[1] Reprinted with permission from: M. Levy, A. Chakravarty**,** H.-C. Huang, R. M. Osgood, Jr**.** *Large magneto-optic enhancement in ultra-thin garnet films*, Appl. Phys. Lett. 107, 011104 (2015). Copyright [2015], AIP Publishing, LLC.

4.1 Instruments and Garnet Thin Film Characterization

This section discusses the working principles behind the optomechanical and mechanical setups involve for characterizing and fabricating commercially obtained $Bi_{0.8}Gd_{0.2}Lu_2Fe_5O_{12}$ film on GGG substrate for its magneto-optical studies. First, the development of a phase-sensitive FR measurement setup is discussed. This instrument is built on an already-existing setup through electronic and mechanical modifications that enable the measurement of FR from sub-nanometer thick garnet films. Preparation of an ultra-thin $Bi_{0.8}Gd_{0.2}Lu_2Fe_5O_{12}$ film from the 2.72 μm -thick film sample utilizes a chemical etching technique. To execute and control the wet etching process, a spin-wet-etch device is developed. The study also requires the determination of thickness of the wet-etched film to a high degree of accuracy. Reflection ellipsometry and transmission electron microscopy (TEM) are the two techniques used for thickness characterization of such films. In reflection ellipsometry, a theoretical model is used in conjunction with experimental data to measure the thickness of a wet-etched film. TEM thickness measurement involves a sample preparation step in which a thin sample of ~30 nm thickness is prepared using FIB. Along with techniques, an MCD set-up is constructed to understand the physical origin of FR enhancement in the ultra-thin $Bi_{0.8}Gd_{0.2}Lu_2Fe_5O_{12}$ film. Herein, all details regarding the set-ups and the techniques used are discussed in their respective subsections.

4.1.1 Ultra- Sensitive FR Measurement Setup

In Figure 4.1, schematic of a very low angular displacement measurement possible optical setup is presented. In this setup, light from a 532nm-wavelength CW diode-pumped-solid-state laser source, operating at 67mW output power, is first allowed to propagate through a neutral density filter, polarizer, collimating and focusing lenses and impinge at normal incidence onto the sample after passing through a bored pole piece of an electromagnet. The laser source here is rated at 5% RMS stability/4hours. The spot size at the sample surface is estimated at 51 μm Airy diameter, approximately. After emerging from the sample and a second pole piece, the beam is collimated and directed through a rotating

Glan-Thompson polarization analyzer, with a rated extinction-ratio of 100,000:1. The probe signal acquires a sinusoidal wave form at 120Hz after passing through the rotating analyzer and being detected by a silicon photo-receiver.

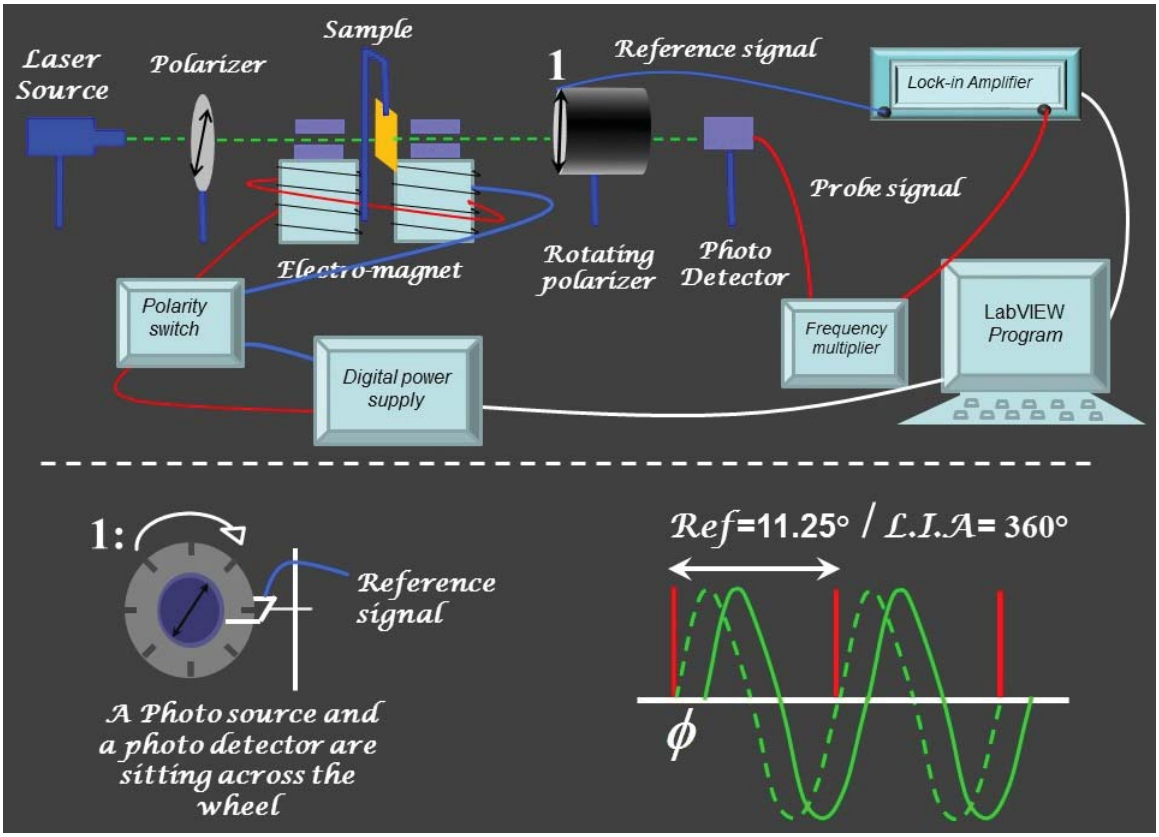

Figure 4.1 In this ultra-sensitive Faraday-Rotation measurement setup, measured polarization rotation gets amplified 32 times, as the phase between two consecutive wheel grooves has an arc distance of 11.25°, whereas the same phase is read as 360° by the lock in amplifier. Some of the components are not shown to keep the schematic clear.

Upon receiving the probe signal, the photo receiver signal is fed into the lock in amplifier via a frequency multiplier assembly. The probe signal has a sinusoidal form and oscillates with a 120 Hz frequency after it passes through the Glan- Thompson polarization analyzer. Given that the analyzer uses the same 60 Hz DC motor housing and the analyzer passing optical beam follows the Malus's polarization law (see Appendix 2), the probe signal frequency is double that of the DC motor frequency. The polarization law also explains the sinusoidal form of the probe signal. The 16× frequency multiplier assembly

is used after the analyzer for further amplification of the probe frequency to match with a reference signal frequency, which is also fed to the lock in amplifier.

A U-shaped photoelectric sensor provides the reference signal from slots on an aluminum wheel with 32 equidistantly-spaced square grooves at the rim. The wheel is mounted on the same hollow-shaft-motor housing as the Glan-Thompson cube and therefore rotates with the same 60 Hz frequency. The reference signal acquires a 1920 Hz frequency. Seeing as the probe and the reference signals are at the same frequency, the SR830 Lock in Amplifier is able to calculate the phase difference between these two signals by integrating them over a time interval of 100ms.

The SR830 lock-in amplifier is designed to read an angular phase shift of 360° for each reference signal interval. However, as each reference pulse is coming in at 11.25° angular intervals from the rotating-wheel, the probe signal acquires a multiplicative factor of 32× as read by the phase monitor of the amplifier. As the reference phase shifts down to 0.01° and is detectable by the amplifier, the Faraday rotation values can be measured as low as 0.00031° since the angular phase shift signal is actually amplified 32 times. Hence, measurements can be comfortably performed on ultra-thin samples. XYZ stage is used to mount the film sample in between the bored pole pieces and a LabVIEW program is used for data acquisition. The digital power meter and a magnetic polarity switch supply the current and flip the magnetic field of the electromagnet.

In the Faraday rotation measurement setup, a 532nm-wavelength laser source is used in order to detect relatively large Faraday rotations as compared to those at near-infrared wavelengths. Given the very small thickness of the thinnest samples, the net rotations that can be observed even at this wavelength are in the order of 0.1°. Of course, the price paid by working at this wavelength is to suffer an increased absorption loss. However, even at this wavelength, the absorption coefficient is still two orders of magnitude lower than in the ultraviolet absorption bands for this garnet material and about one order of magnitude lower than in the 450 nm and 500 nm band. Moreover, and very importantly, the magnetic circular dichroism at 532nm is relatively small, yielding 1.1° of ellipticity.

4.1.2 Thin and Ultra-Thin Film Preparation

A total of 14 $Bi_{0.8}Gd_{0.2}Lu_2Fe_5O_{12}$ films ranging in thickness from 19 nm to 2 μm are prepared for Faraday-Rotation measurements. The samples are prepared by sequential etching of 2.72 μm film in an 80ml ortho-phosphoric acid bath with a slow-rotation rate to ensure uniform thickness. The slow rotation of the sample in the acid is provided by a spin-wet-etching device as shown in Figure 4.2. This microcontroller-based etching device contains two stepper motors and a dc motor. Steppers transfer the film sample from the phosphoric acid to the water bath, and the dc motor provides the rotational motion while

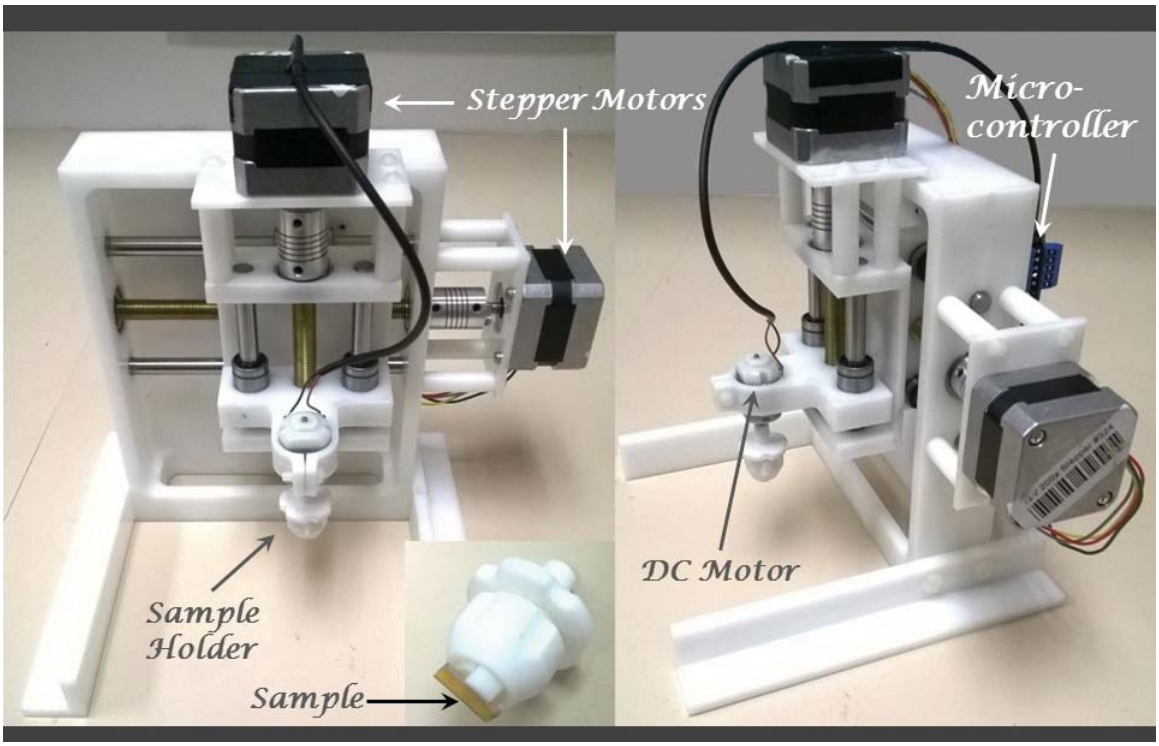

Figure 4.2 Micro-controller based spin wet etching device used for fabricating thin and ultra-thin garnet films by reducing the thickness of a thicker film.

the sample is immersed in the baths. These motors are controlled by an Arduino microcontroller and are controlled with Arduino with LabVIEW. The device frame is made from DuPont Delrin resin (polyoxymethylene acetal resin) and the sample holder is made from Teflon (polytetrafluoroethylene). Teflon does not interact with the phosphoric acid,

but Delrin does. The sample holder is designed in such a way that it can hold easily samples of 4–6 mm width in between its mechanically adjustable chucks.

For etching a $Bi_{0.8}Gd_{0.2}Lu_2Fe_5O_{12}$ film with GGG substrate, the spin-wet-etching device is mounted first on a temperature-controlled hot plate. Two baths of phosphoric acid and de-ionized water are also mounted on this hot plate along with the device. Here, the temperature of the hot plate is kept in between 85 and 120°C. The hot plate temperature is set to these temperatures to produce a film surface with minimum surface roughness after the etching. Positions of the two baths on the hot plate are adjusted such that the dc motor mount holding the sample can dip into the water bath once acid etching process is complete. To accomplish a uniform etching throughout the film surface, the sample is rotated with a slow speed of 40 rpm in the acid bath. After etching, the sample is lifted slightly above to the acid and rotated again with 100 rpm speed to throw off the acid residue from the film surface. This avoids the uncontrolled etching of the film while the sample transfer process from acid to water bath is occurring. Then, the stepper motor, which controls the sample position in the vertical direction, lifts the sample up all the way in a sample cart. The sample cart, sits on two aluminum rods of identical diameter and length, and on a lead screw. In operation, stepper motors rotate this lead screw, and thus the sample cart, held by friction to the lead screw, moves in the vertical direction. Two aluminum rods are holding the cart loosely to support the motion of the cart on the lead screw. Once, the sample is all the way up, the other stepper motor pushes the sample cart, aluminum rods, and lead screw assembly in the horizontal direction, thus directing it to the water bath. This assembly cart is designed to move in the horizontal directions by means of a lead screw and two aluminum rods, similar to the sample cart. After the sample reaches its position above the water bath, it is then lowered and allowed to go inside the water. In the water bath, the sample is rotated at 100 rpm, and then lifted slightly up above the water surface and rotated again at the same speed to clean the sample surface. Finally, the sample from this position is moved up to a position above the water bath, where it was initially at the start of the acid etching process.

The etching process described above takes 3 to 4 hours' time to thin a 2.7 μm -thick

$Bi_{0.8}Gd_{0.2}Lu_2Fe_5O_{12}$ film to a final thickness of 0.5 μm at 120°C. During the etching process, the film thickness was periodically measured in V-Vase ellipsometer in order to to target the desired final thickness. After reaching 0.5 μm film thickness, the temperature of the acid bath was lowered to 85° C for another 2 hours of acid processing. At this temperature, the etching rate is sufficiently slow to enable thickness reduction down to sub-nanometer dimensions. A sample of smooth, ultra-thin $Bi_{0.8}Gd_{0.2}Lu_2Fe_5O_{12}$ film is thus prepared by the acid etching process.

4.1.3 Film Thickness Characterization

Thickness measurements on a thin garnet film uses two techniques: the reflection ellipsometry method and the TEM analysis. These two methods yields mutually consistent results.

The reflection ellipsometry method uses a V-VASE ellipsometer to measure the reflected elliptical polarization state orientation, ψ of an optical beam. This measurements are done on the $Bi_{0.8}Gd_{0.2}Lu_2Fe_5O_{12}$ films on GGG substrate and in the wavelength range 1000–1700 nm with a 10 nm wavelength step-size. In this wavelength range, $Bi_{0.8}Gd_{0.2}Lu_2Fe_5O_{12}$ film does not absorb light and hence allows accurate thickness measurement. For further improved accuracy in the measurement, the ψ value is measured for three different angles of incidence of the optical beam to the sample surface; 65°, 70°, and 75°. Initial measurements are done on two thin film samples: 2.72 μm-thick $Bi_{0.8}Gd_{0.2}Lu_2Fe_5O_{12}$ film on GGG substrate, and a bare GGG substrate. To measure the film thickness, film samples are roughened from the substrate side to avoid the transmission loss. In the measurement, sinusoidal oscillation in ψ is recorded over the selected wavelength range from the samples which comprise thin films on a GGG substrate. This oscillation is attributed to the two interfaces of the samples in question, as described earlier in subsection 2.4.2 of Chapter 2. In contrast, ψ spectra of only the GGG substrate do not show the same oscillations. Later, using the GGG substrate ψ spectra as reference, an oscillator model is built upon the results from the 2.72 μm-thick film sample, as shown in Figure 4.3. In the thickness model, Lorentz, Tauc-Lorentz, and Gaussian

oscillator functions are used to calibrate the film thickness. The model is used later as a reference to calculate the film thicknesses of 15 other film samples ranging from 2.72 μm to 19 nm in size. The model-calibrated $Bi_{0.8}Gd_{0.2}Lu_2Fe_5O_{12}$ film thicknesses on GGG substrate are shown in Figure 4.4. It can be seen from Figure 4.4 that the magnitude of ψ oscillation decreases with decreasing film thickness. This is due to a decrease in the path

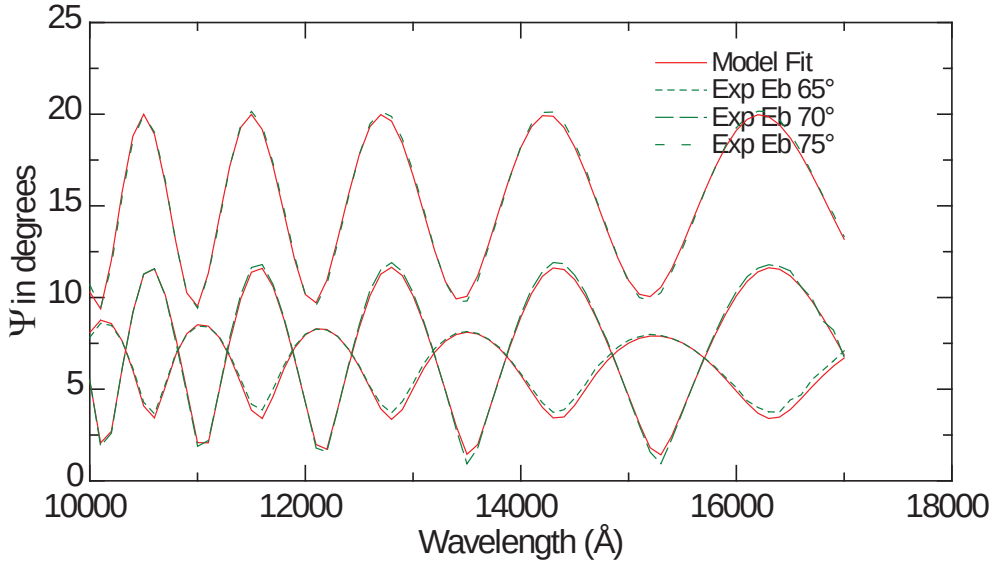

Figure 4.3 Ellipsometric model to determine the thickness of a $Bi_{0.8}Gd_{0.2}Lu_2Fe_5O_{12}$ film on GGG substrate. Film thickness value in this measurement reads 2717.79 ± 0.94 nm.

difference between reflected waves from the aforementioned two interfaces. The model developed in this work calibrates this difference, and is thus capable of calculating the $Bi_{0.8}Gd_{0.2}Lu_2Fe_5O_{12}$ film thickness on GGG substrate.

Film thickness accuracy plays an important role in calculating the specific Faraday rotation of garnet films with different thicknesses. It is also required when calculating the absorption coefficients of RCP and LCP lights in such films at specific optical frequencies, as described later in section 4.2.

TEM film thickness measurement involves a step of preparing a thin film sample of size ~30 nm through which electrons form the instrument can penetrate and produce a transmission image for thickness analysis. Steps involved in the TEM sample preparation are shown in Figure 4.5.The FIB foil lift-out technique [79] is used to prepare such a film sample. In this technique, a tungsten pad of the dimensions 15 μm in- length 3 μm in width

and ~1 μm or more in height is deposited first on top of the targeted sample to protect the surface film from the milling. This also assists later during the lift-out process. After the deposition of a tungsten pad, a rectangular prism of material 26 μm in length, 4 μm in

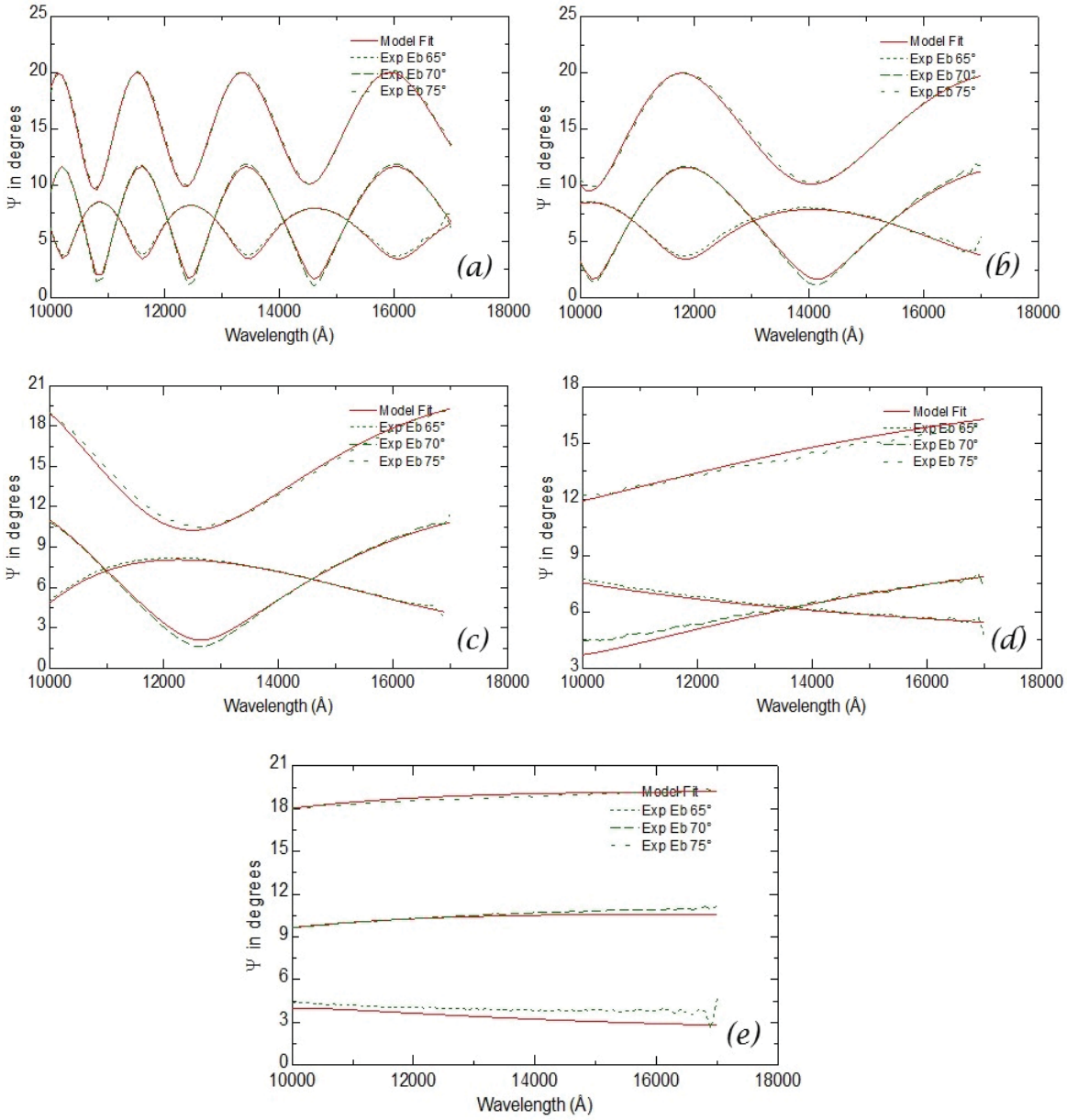

Figure 4.4 $Bi_{0.8}Gd_{0.2}Lu_2Fe_5O_{12}$ film thicknesses: (a) 1884.9 nm (b) 828.8nm (c) 376.7nm (d) 96.5nm, and (e) 31.3nm on GGG substrates measured by reflection ellipsometry method.

width, and 6 μm in height is milled at the boundary between the bulk film and substrate. The prism of material is then lifted out by engaging a tungsten microprobe at the corner.

After lifting out the chunk sample part, it is attached to a TEM grid, again using tungsten deposition. Further milling is carried out on the vertical walls along the width of the sample to produce a sample ~50 nm in width. Subsequently, vertical walls of this 50 nm thick sample are polished using a FIB beam of 35 nm diameter and 0.015–0.04 nA current.

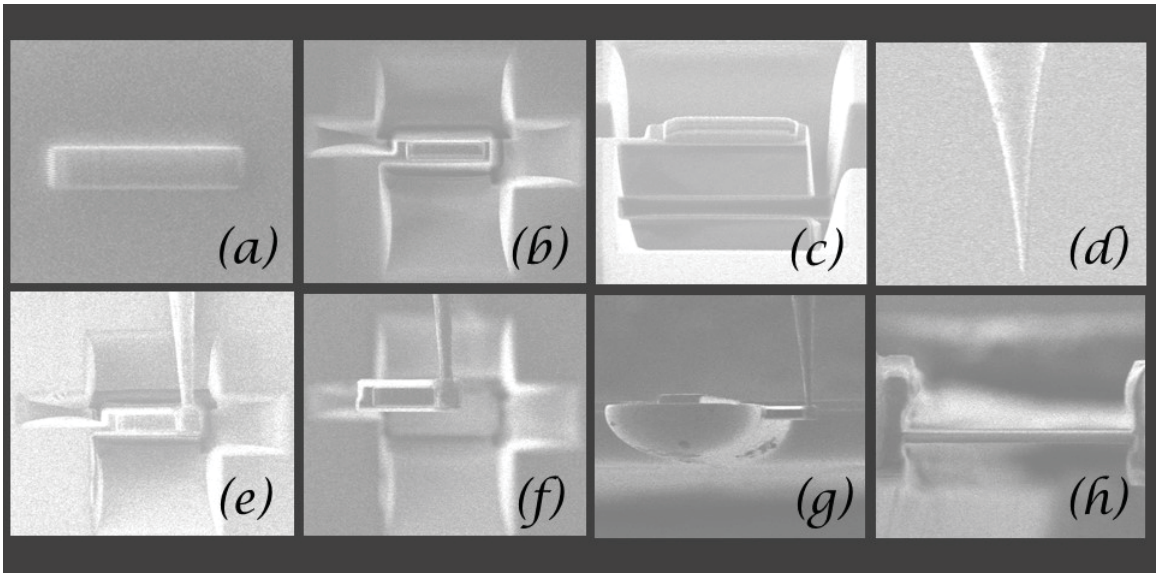

Figure 4.5 TEM sample is prepared by depositing (a) a tungsten pad on targeted sample. FIB mills out (b), (c) a small piece of the sample by (d), (e), (f) engaging a tungsten microprobe and then attached to (g) TEM grid by welding. Furthermore, the vertical walls of the sample are polished in FIB for electron transparency.

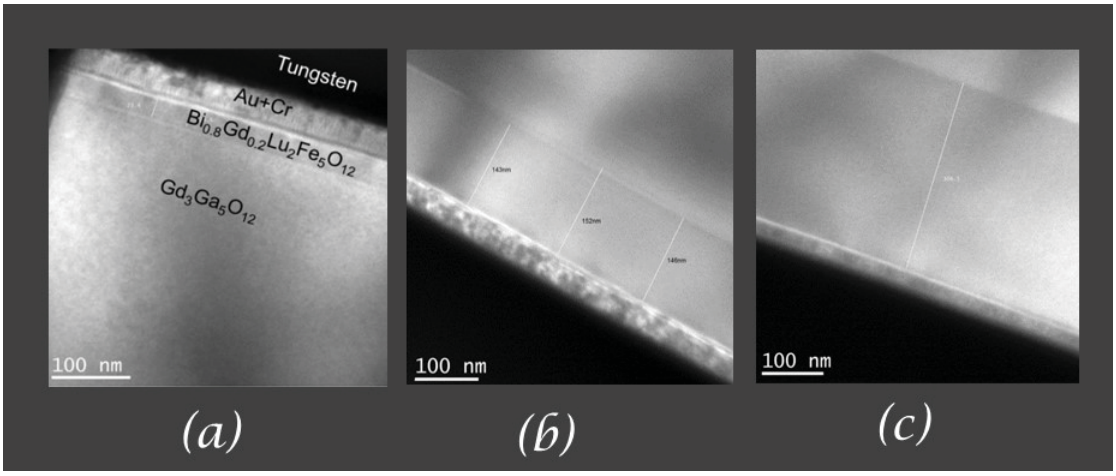

Figure 4.6 $Bi_{0.8}Gd_{0.2}Lu_2Fe_5O_{12}$ film thicknesses measured using TEM for (a) 23.4nm (b) 146nm and (c) 307nm films, respectively.

In the TEM analysis, tunneling electrons are allowed to pass through the ~30 nm thick $Bi_{0.8}Gd_{0.2}Lu_2Fe_5O_{12}$ film and GGG substrate foil, creating a transmission image of the

sample. Under TEM observation there is a clear demarcation between the $Bi_{0.8}Gd_{0.2}Lu_2Fe_5O_{12}$ films and the GGG substrate, as shown in Figure 4.6. Four samples out of 13 are examined with TEM to verify the thicknesses measured via ellipsometry.

4.1.4 MCD Measurement Setup

These measurements are performed in the V-Vase ellipsometer, in a magnetic field, and are designed to evaluate the absorption and circular dichroism in the 260–800nm wavelength range. Each sample is placed in an aluminum mount holding two strong neodymium magnet rings 10mm apart, configured to magnetize the sample in the normal direction. The magnets produce a 1.3 Tesla magnetic field. The mount and magnet assembly is such that the ellipsometric beam can easily pass through 6.35mm-diameter

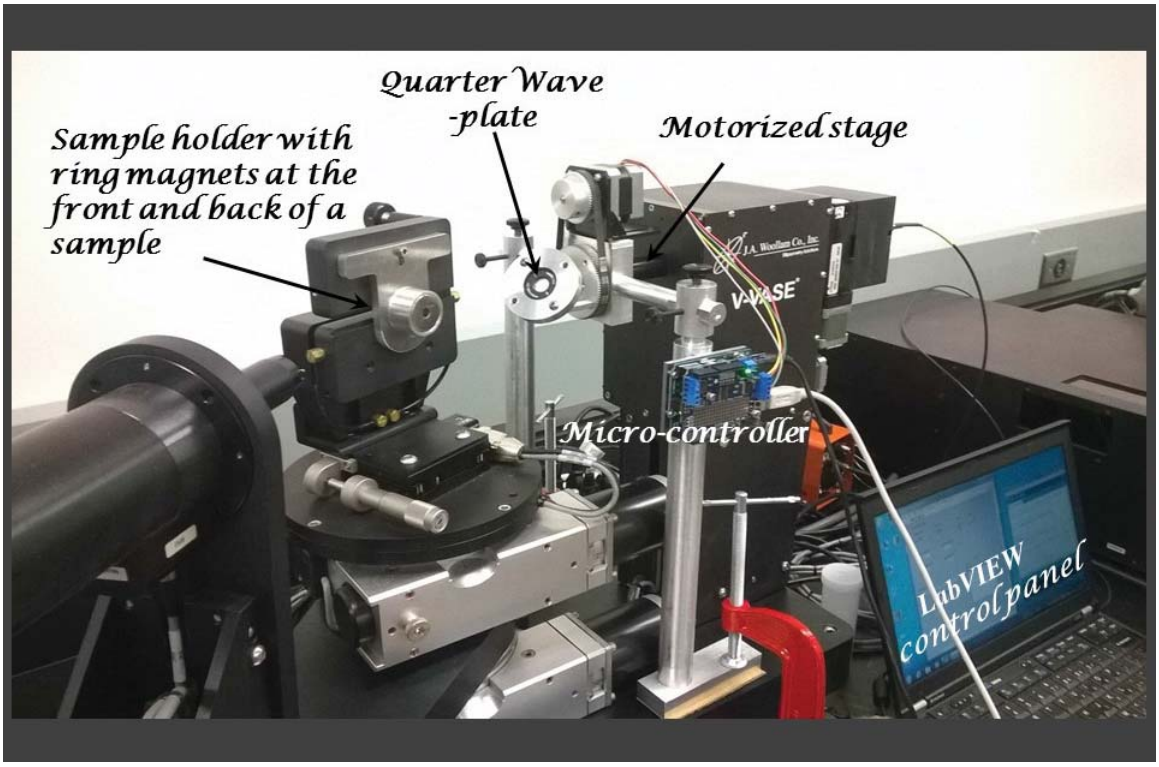

Figure 4.7 Modified V-Vase ellipsometer setup to produce pure circular polarization states in the wavelength range 260—800nm to perform MCD measurements from $Bi_{0.8}Gd_{0.2}Lu_2Fe_5O_{12}$ films.

holes in the magnets. Absorption measurements for both right- and left-circularly polarized light are conducted using two-quarter wave plates, rated to operate in the 260–410 nm and

400–800nm wavelength ranges, respectively. Here, the micro-controller based setup as shown in Figure 4.7 gives rotation or tilt to a quarter wave plate to achieve pure circular polarization states from the V-Vase ellipsometer.

4.2 Measurements on Garnet Films

4.2.1 Specific FR from Hysteresis Measurements

In this analysis, the $Bi_{0.8}Gd_{0.2}Lu_2Fe_5O_{12}$ sample films are placed between pole pieces of an electromagnet in the optical setup described in subsection 4.1.1. An electrical current step and maximum current of 0.05A and 7A, respectively, are used for the Faraday rotation measurements, corresponding to a maximum magnetic field of 2,700 Oe on the sample at 19.3Oe scan field-steps. Since the films are grown on paramagnetic GGG, the substrate's response from the overall Faraday rotation signal must be subtracted out. Therefore, the hysteresis loop measurements are also carried on bare substrate samples for calibration purposes. These yield a net Faraday rotation of 0.42° at 2,700 Oe across the full bare substrate thickness of 1 mm. A total of 15 $Bi_{0.8}Gd_{0.2}Lu_2Fe_5O_{12}$ films ranging in thickness from 2.72 μm to 19.16nm are studied. Figure 4.8 (inset) shows hysteresis measurements on some of the films. Again, Figure 4.8 shows the specific Faraday rotation per centimeter at the saturation field for each film analyzed in this work. This data is extracted from the recorded hysteresis loops. This figure shows that for samples thicker than ~100nm, the specific rotation remains constant, showing a bulk-like response, but grows steadily for thinner films.

Although there is a small calibration difference between thickness measurements under TEM and ellipsometric techniques, both show mutually consistent specific Faraday rotation results as shown in Figure 4.9. In Figure 4.9, a given set of specific Faraday rotation data for $Bi_{0.8}Gd_{0.2}Lu_2Fe_5O_{12}$ films of thickness lower than 400nm is plotted. The blue and red data sets correspond to normalization, ellipsometric, and TEM-thickness values, respectively.

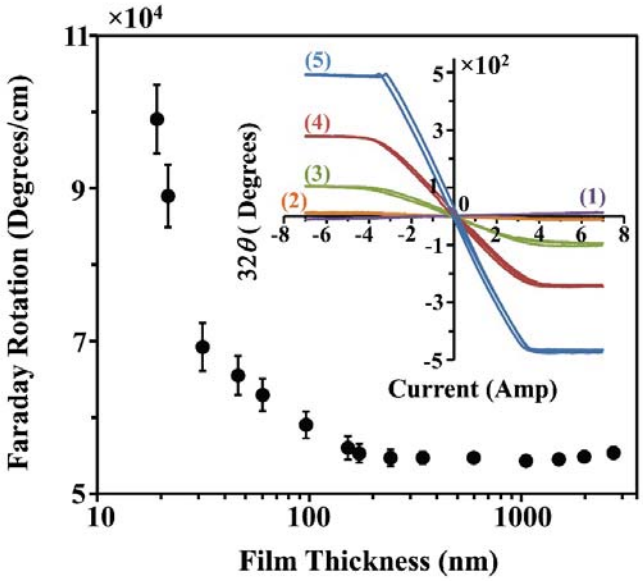

Figure 4.8 Specific Faraday rotation θ versus film thickness for $Bi_{0.8}Gd_{0.2}Lu_2Fe_5O_{12}$ films (the substrate contribution has been folded out in this data set) at 532nm wavelength. Inset: Faraday rotation hysteresis loops measured on the $Bi_{0.8}Gd_{0.2}Lu_2Fe_5O_{12}$ films for different thicknesses and on the GGG substrate: (1) Substrate, (2) 60nm, (3) 590nm, (4) 1520nm and (5) 2720nm. The magnetic field is expressed in terms of the current in the electromagnet. Reprinted with permission from: ref. [1] Fig. 1

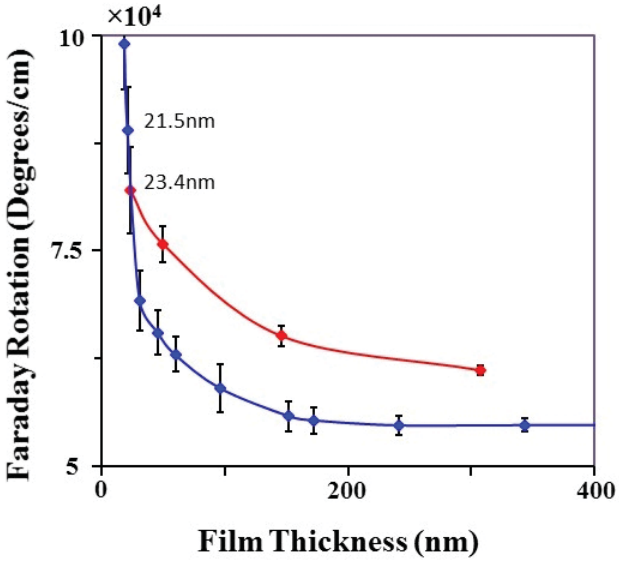

Figure 4.9 Specific Faraday rotation calculated using ellipsometry-measured film thicknesses (blue curve) and the TEM-measured film thicknesses (red curve) show the same increasing trend with decreasing thickness.

4.2.2 MCD and Kramers-Kronig Analysis

The main purpose of these measurements is to gain insight into the optical absorption bands of $Bi_{0.8}Gd_{0.2}Lu_2Fe_5O_{12}$ films in the ultraviolet, visible, and infrared regimes. Elucidation of the effects of these absorption bands on Faraday-rotation may help explain the mechanism underlying the monotonic increase in specific FR from ultrathin films. These measurements also allow for an independent verification of the increasing trend in specific Faraday rotation for sub-100 nm films previously observed via the rotating polarizer technique described in section 4.2.1. Magnetic Circular dichroism (MCD) away from the Faraday-rotation-probe wavelength, and especially in the strong ultraviolet and visible absorption bands, determines the Faraday rotation at that wavelength through the Kramers-Kronig relations.

MCD in the ultraviolet and visible absorption bands determine the Faraday rotation at the 532nm probe wavelength. Hence, these data are used to obtain an independent verification of the dimensional dependence of Faraday rotation. MCD measurements are done on four films, of thicknesses: 152.0, 96.5, 46, and 19 nm. MCD is determined by measuring the transmission of circular polarized light of opposite helicities across the samples in a magnetic field. A bare 1 mm-thick GGG substrate is also analyzed in this way in order to subtract out its absorption loss from that measured for films comprising a film plus the substrate. Right- and left-circularly polarized lights are sent through the samples, and the transmission spectra for both beams are recorded for the above-mentioned films.

In general, transmitted power through the GGG substrate is given by

$$I_S^i = I_0 e^{-\alpha_S^i d_S} \quad , \tag{4.1}$$

where I_0 is the intensity of the probe beam, I_s^i and α_s^i are the transmitted power and the absorption coefficients, respectively, for right- and left-circularly polarized light in the substrate; d_s is the substrate thickness; and the index i tracks the helicity of the beam. Again, the transmission spectra for a $Bi_{0.8}Gd_{0.2}Lu_2Fe_5O_{12}$ film plus GGG substrate is given by

$$I_{f+S}^{i} = I_0 e^{-(\alpha_f^i d_f + \alpha_S^i d_S)} \quad , \tag{4.2}$$

where I_{f+s}^{i} corresponds to the transmitted power of the different circularly polarized beams, α_f^i to the absorption coefficients for the right- and left-circularly polarized light in the film, and d_f is the thickness of the film. The absorption coefficient of the circular polarized light in the film is obtained from the ratio of Eq. (4.2) and Eq. (4.1), and the natural logarithm of this ratio. It should be noted here that film thickness plays an important role in determining the value of the absorption coefficients. Absorption coefficients for both circular polarizations in the 260–800 nm wavelength range obtained in this way. Transmission spectra are corrected to account for reflections by normalizing the data to the substrate transmittance. MCD is thus defined here as the difference in the absorption coefficients between the two circular polarizations at each wavelength. Measured MCD spectra for four films are shown with the calculated theoretical spectra in Figure 4.10. Theoretical calculation of MCD spectra is discussed in section 4.3.

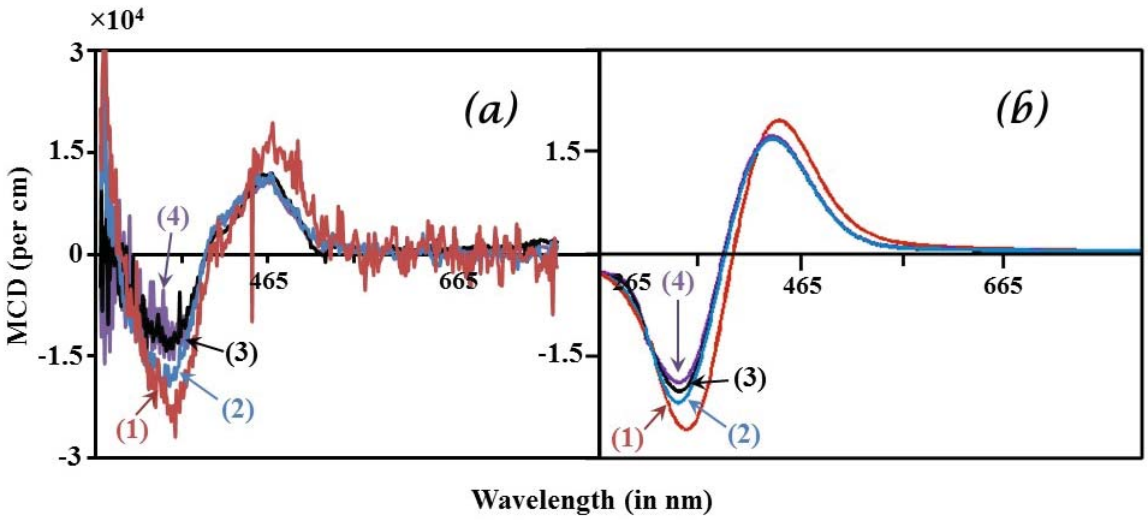

Figure4.10 Magnetic circular dichroism on four $Bi_{0.8}Gd_{0.2}Lu_2Fe_5O_{12}$ films of different thicknesses: (a) Experimental results. (b) Theoretical analysis calculated from the permittivity tensors for iron garnets as explained in theoretical section 4.3. The curves correspond to the following film thicknesses: (1) 19 nm, (2) 46 nm, (3) 95 nm, (4) 153 nm. Reprinted with permission from: ref. [1] Fig. 2

To perform a Kramers-Kronig analysis and obtain the refractive indices for right- and left-circularly polarized light at 532 nm, the optical spectrum is partitioned into in small wavelength steps and a summation is performed over the wavelength range. The index is thus given by

$$n_p^i = 1 + \frac{\mathbf{P}}{2\pi^2}\sum_n \frac{\alpha^i(\lambda_n)}{1-\frac{\lambda_n^2}{\lambda_p^2}}\Delta\lambda_n \quad , \tag{4.3}$$

where n^i_p are the refractive indices of the i^{th}- (right- or left-) circularly polarized light at the probe wavelength (532 nm), **P** is the Cauchy principal value (equal to 1), λ_p is the probe wavelength, and $\Delta\lambda_n$ are the wavelength steps. $\alpha^i(\lambda_n)$ is the absorption coefficient for the i^{th} circular polarization at λ_n wavelengths.

The specific Faraday rotation (in degrees) at wavelength λ is given by $180(n_R - n_L)/\lambda$. Specific Faraday rotations calculated from MCD data for the aforementioned film thick-

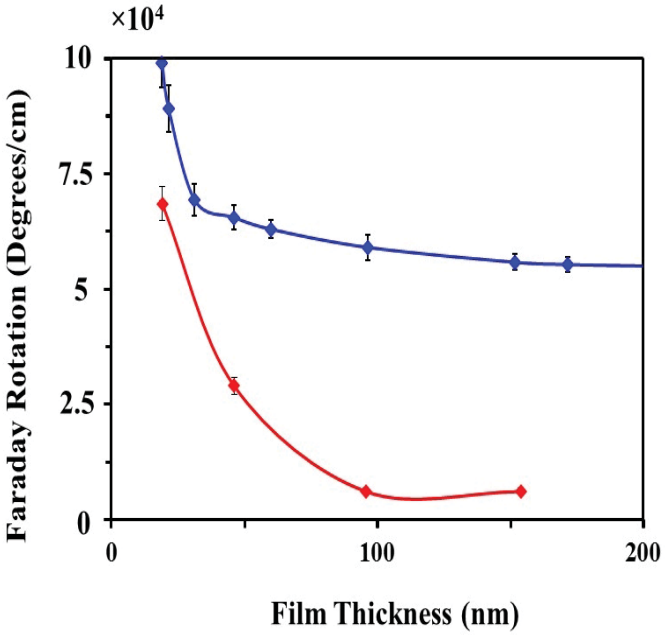

Figure 4.11 The calculated specific Faraday rotation (red curve) at 532 nm from the MCD measurements increases with decreasing film thickness. For the purpose of comparison, the specific Faraday rotation (blue curve) for 200nm $Bi_{0.8}Gd_{0.2}Lu_2Fe_5O_{12}$ film thicknesses measured by ellipsometer is shown.

-nesses yield the same trend as before; increasing rotation with decreasing thickness below ~150nm. This is shown by the red curve in Figure 4.11. However, it can be seen that rotation angles for films thicker than 19 nm are offset from ellipsometry film thickness measurements by factors of ~7 or more. These differences are due to two reasons: dichroism measurements neglect absorption loss contributions at wavelengths below 260 nm, and the intensity of the ellipsometer lamp source is very low below 350 nm for thicker films.

4.2.3 Compositional Analysis: RBS

Direct experimental confirmation of the composition of the films in the bulk region and the transient layer at the interface (with the GGG substrate) are obtained from Rutherford-backscattering data. RBS is described in section 2.4.2 of Chapter 2. Four samples of different thicknesses ranging from 19 to 340 nm, all from the same LPE-grown wafer, are analyzed. The transient layer is modeled to contain Ga in addition to Bi, Lu, Fe, Gd and O, since the substrate composition is $Gd_3Ga_5O_{12}$. It is assumed that some of these elements diffuse into the film during growth. Only an average composition for the transient layer is sought. The bulk composition for the thickest of these films (340 nm) was found to be $Bi_{0.8}Gd_{0.2}Lu_{2.0}Fe_{4.5}O_{12}$ per formula unit (pfu), and the thinnest (19 nm) was measured to be $Bi_{0.7}Gd_{0.2}Lu_{2.0}Fe_{5.0}O_{12}$. The transient layer was 16 nm thick for the thickest (340 nm) film with $Bi_{0.8}Gd_{0.2}Lu_{2.0}Fe_{5.0}Ga_{0.1}O_{12}$ pfu. An important feature of these data is that in none of the four samples analyzed has an average Bi content across the thickness (including the transient layer) in excess of 0.8 pfu. Figure 4.12 shows the result from one of the RBS measurement done on 340 nm thick film. These RBS measurements are done commercially by Evans Analytical Group (*EAG*). *EAG* uses a theoretical layer model to adjust the concentration of compositions and thickness of the film over the experimentally measured data. Table 4-1 shows *EAG* measured layer film thicknesses over 340nm $Bi_{0.8}Gd_{0.2}Lu_2Fe_5O_{12}$ film and its constituent elements in percentage. Assumed density in their analysis is also shown in the table.

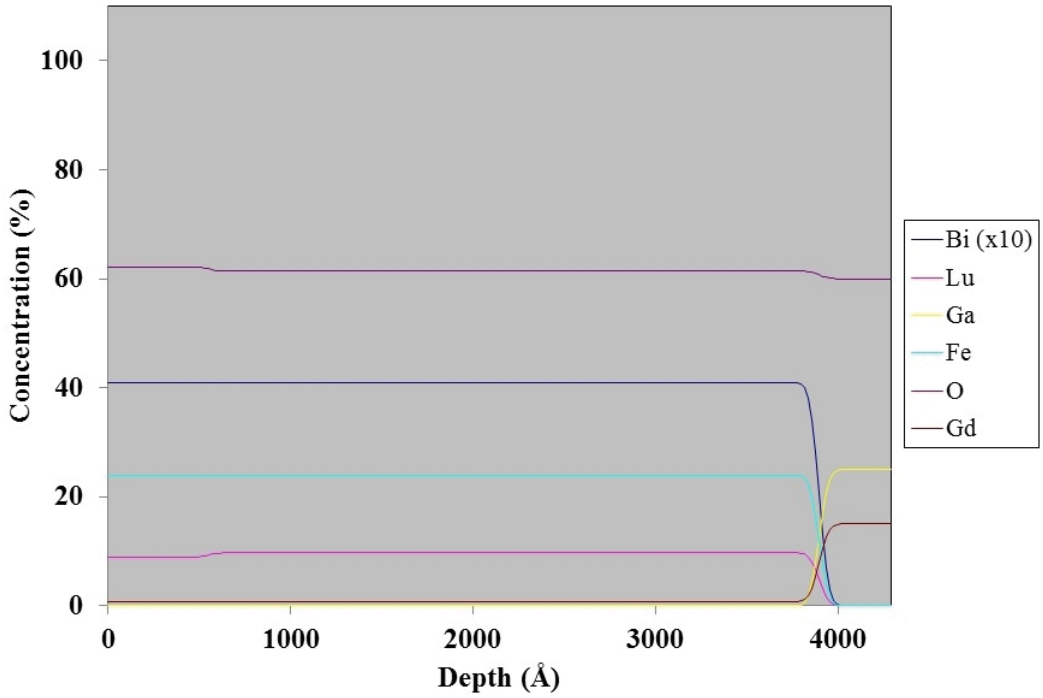

Figure 4.12 The RBS measurement shows a transient layer in between the 340nm thick $Bi_{0.8}Gd_{0.2}Lu_{2.0}Fe_{4.5}O_{12}$ film and the GGG substrate.

Table 4-1: Compositional analysis done on film $Bi_{0.8}Gd_{0.2}Lu_2Fe_5O_{12}$ with GGG substrate by EAG.

	"RBS" Thickness [Å]	**Atomic Concentrations [at%]**						**Assumed Density [at/cc]**
		Bi	**Lu**	**Ga**	**Fe**	**O**	**Gd**	
Layer 1	550	4.1	8.9	-	24	62.2	0.8	6.91×10^{22}
Layer 2	3350	4.1	9.7	-	24	61.4	0.8	6.88×10^{22}
BULK	-	-	-	25	-	60	15	6.00×10^{22}

Estimated uncertainties in the compositional concentrations by *EAG* are shown in Table 4-2.

The density of the $Bi_{0.8}Gd_{0.2}Lu_2Fe_5O_{12}$ film with a GGG substrate used by RBS analysis to determine the composition of the film can be calculated using atomic densities of the atomic constituents. Accurate film densities allow for precise calculation of the film

Table 4-2: Uncertainties in the film compositions calculation used by *EAG*.

Element	Uncertainty (at %)
Bi	±0.5
Lu	±0.5
Gd	±1
Fe	±1
O	±5
Ga	±1

thickness and composition, and they can be calculated by two methods: the elemental number density method, and the unit cell method. In the first method, the atomic number density of an element is calculated using the atomic mass (m_s) and normal density (d_s) by the following formula:

$$n_s = \frac{\mathrm{N_A} d_s}{m_s} \quad , \tag{4.4}$$

where N_A is Avogadro's number, 6.023×10^{23} mol^{-1}. After calculating the atomic number densities for all constituents in the garnet film, the garnet film atomic density is calculated (see Appendix 3). Calculating atomic densities by this method tends to estimate slightly lower atomic number densities than the actual number densities of a garnet film.

In the unit cell method, the atomic number density of a garnet film is estimated from the lattice constants of garnets which are grown by a complete substitution of a particular rare-earth element in YIG garnet. This method first calculates the unit cell volume of these garnets, and then the number of unit cells that exist in a 1 cm^3 volume. Since all the YIG-based iron garnets contain 160 atoms in their unit cell, multiplying this number by the number of unit cells per cubic centimeter yields the atomic number densities of those completely rare-earth-element substituted YIG garnets. Now using the atomic number densities of these garnets, and based on known YIG number densities, the atomic number density of an iron garnet film with variable composition may be calculated (see Appendix

3). This method estimates a slightly higher atomic number density of an iron garnet film than the actual value.

Averaging atomic number densities calculated by the above two methods can give a good estimation of the atomic number density of a garnet film. Calculated atomic number densities for three films used in the RBS analysis are given in Table 4-3. From this table, it can be seen that there is a difference in atomic number densities from that used by *EAG*. Therefore, it is guessed that the thickness of $Bi_{0.8}Gd_{0.2}Lu_2Fe_5O_{12}$ is slightly higher in their estimations.

Table 4-3: Average atomic number density of garnet films.

Magnetic Garnet Films	Atomic number density (at/cc)
$Bi_{0.8}Gd_{0.2}Lu_2Fe_5O_{12}$	7.1473×10^{22}
$Bi_{0.4}Gd_{1.6}Lu_{1.0}Fe_{2.5}Ga_{2.5}O_{12}$	6.9863×10^{22}
$Gd_3Ga_5O_{12}$	6.7668×10^{22}

4.2.4 Surface Measurements

Samples of different film thicknesses are prepared from a single wafer by the etching process described in section 4.1.2. Surface roughness is examined by atomic force microscopy on 4 samples. For these measurements, a clean $20\times20\ \mu m^2$ area on the sample surfaces is selected. A mean surface roughness of 1.3 nm is recorded for the 21.6 nm-thick film, 1.7 nm for the 60.1 nm-thick film, and 4.7 nm for thicker films (171.88 nm- and 342.95 nm-thick) as shown in Figure 4.13. Surface analysis on these samples is important as it can reveal surface contributions to the monotonic increase of specific Faraday rotation in ultra-thin $Bi_{0.8}Gd_{0.2}Lu_2Fe_5O_{12}$ films. Further study of the film surface is planned for future work.

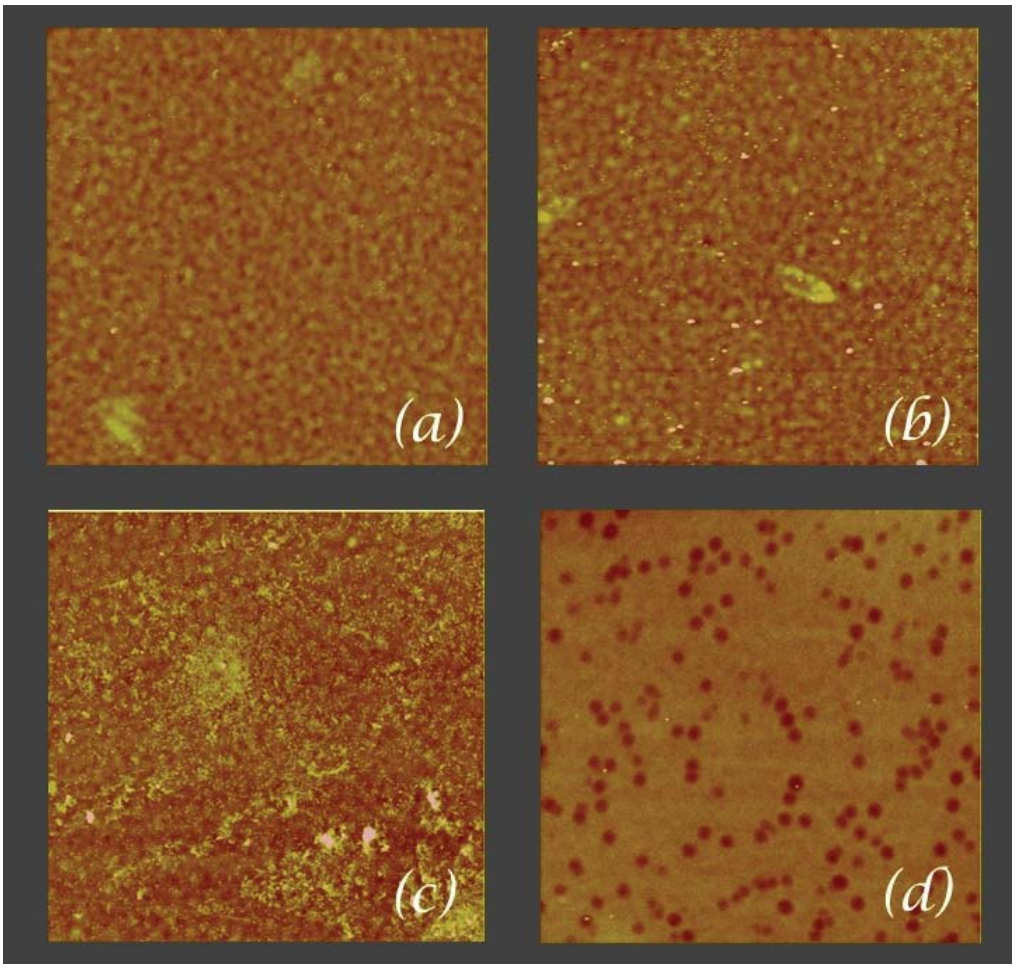

Figure 4.13 AFM measurements on $Bi_{0.8}Gd_{0.2}Lu_2Fe_5O_{12}$ film of thicknesses (a) 21.6nm (b) 60.1nm (c) 342.9 nm, and on (d) GGG substrate.

4.2.5 Micro-Raman Measurements

Micro-Raman spectroscopy is conducted on several of the film samples as a function of film thickness. The results are shown in Figure 4.14(a). Note that the exposure time of the excitation on each film is optimized so that the obtained spectra can be vertically displaced for clarity. In particular, Lorentzian peak fitting is performed on the spectra between the wavenumber of 600–800 cm^{-1} to investigate the effects of film thickness on phonon modal activities. In this spectral range, Raman modes at ~685 cm^{-1} (denoted P_1) and ~729 cm^{-1} (denoted P_2), originating from the intrinsic $Bi_{0.8}Gd_{0.2}Lu_2Fe_5O_{12}$ film were revealed, in addition to a mode at ~740 cm^{-1} originating from the GGG substrate. The peak intensity ratio of I (P_2)/I (P_1) and the mode location of P_2 were further characterized and shown in

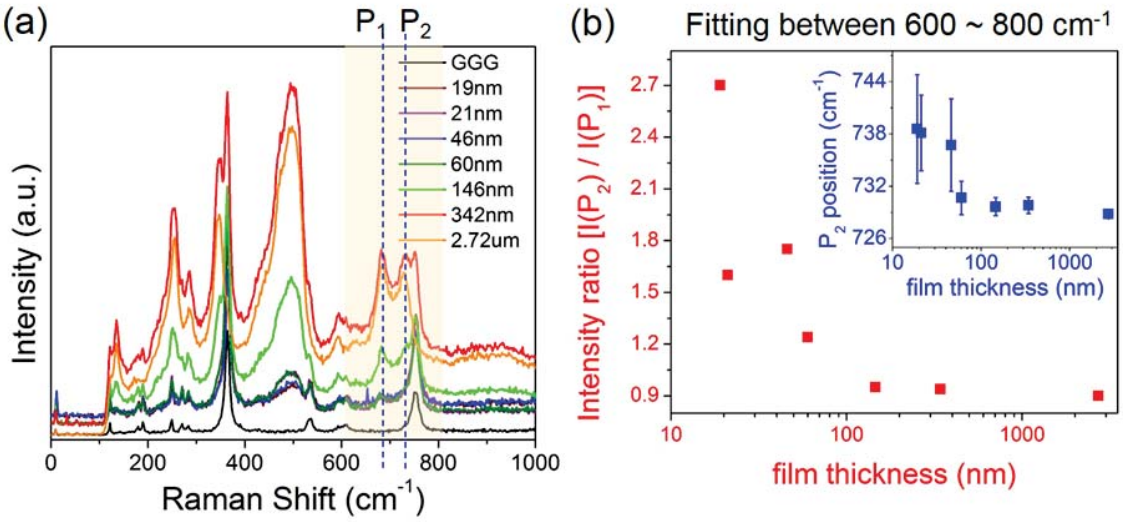

Figure 4.14 Raman shifts as a function of film thickness showing enhancement in intensity ratio and shifts in relative peak position. Reprinted with permission from: ref. [1] Fig. 3

Figure 4.14(b). As seen in Figure 4.14(b), these features show a similar trend of changes as compared to the Faraday rotation data in Figure 4.8. Raman peak-ratio and peak-separation enhancement on selected pairs of Raman peaks are found for reduced film thickness (Figure 4.14). It is possible that the surface and compositional gradients at the interface are playing a role by affecting the vibrational modes and electronic relaxation times. These changes reflect variations in electronic polarizability through lattice modifications below ~100 nm.

4.2.6 Error Analysis

Uncertainties in the data can stem from a few sources of error. Frequency fluctuations in the lock-in amplifier's reference signal due to imperfect equidistant spacing of the grooves in the rotating wheel mounted around the Glan-Thompson polarization analyzer is one of them. This imperfection leads to 0.3 Hz frequency fluctuations in the reference signal, corresponding to a ±0.053° uncertainty in the un-normalized Faraday rotation values. Another source of error corresponds to uncertainties in the measured thickness of the films. Average variations in film thickness measured by ellipsometer are ±1nm. These are too minute to be noticeable in the specific rotation of thick samples. However, for thinner films,

these uncertainties are not insignificant and are included in the error bars shown in Figure 4.8, Figure 4.9, and Figure 4.11.

4.3 Theoretical Analysis of Iron Garnet Films

An enhancement in the specific Faraday rotation at 532 nm can be traced back to a corresponding enhancement in magnetic circular dichroism in the absorption bands of the iron garnet[20, 21]. The real part of the dielectric permittivity at this wavelength, and hence the difference in refractive indices between right- and left-circular polarizations, is a function of the magnetic circular dichroism at all other wavelengths. This is a consequence of the Kramers-Kronig relations.

Thus following the formulation of Dionne and Allen for bismuth-substituted iron garnets [1, 20, 21], the magnetic circular dichroism at wavelength λ in the absorption bands is given by

$$\Delta\alpha = \frac{4\pi}{\lambda}\left(\frac{k\varepsilon_1' - n\varepsilon_1''}{n^2 + k^2}\right), \tag{4.5}$$

where n and k are the average real and imaginary parts of the refractive index (averaged over both circular polarizations), and the diamagnetic functions for the off-diagonal components of the permittivity tensor elements $\varepsilon_1 = \varepsilon_1' + i\varepsilon_1''$ are described by

$$\varepsilon_1(\omega) = \omega_p^2 \sum_{i=a,d} \sum_{+}^{-} \frac{f_{i\pm}}{2\omega_{i0}} \frac{\omega(\omega_{i0\pm}^2 - \omega^2 - \Gamma_i^{\,2}) + i\Gamma_i(\omega_{i0\pm}^2 + \omega^2 + \Gamma_i^{\,2})}{\left[(\omega_{i0\pm}^2 - \omega^2 + \Gamma_i^{\,2})^2 + 4\omega^2\Gamma_i^{\,2}\right]} \tag{4.6}$$

The summation indices *a*, *d* refer to the octahedral- and tetrahedral-coordinated sub-lattices of the garnet, respectively; $\omega_p = \sqrt{\frac{4\pi Ne^2}{m\varepsilon(\infty)}}$ is the plasma frequency; *N* the density of electronic transition centers, $\varepsilon(\infty)$ the dielectric permittivity at very large frequencies; *e* and *m* are the electron charge and mass, respectively; $f_{i\pm} = \pm(f_i/2)(1 \pm \Delta_i/\omega_{i0})$ are the oscillator strengths of the positive and negative circular-polarization-induced electronic

transitions; ω_{i0} and Γ_i correspond, respectively, to the resonance frequency and half-linewidth of the transition from the ground state to the Fe^{3+} excited state that is spin-orbit split by $2\Delta_i$; and $\omega_{i0\pm} = \omega_{i0} \pm \Delta_i$.

Fits to this model show good agreement with the experimental MCD data and are displayed in Figure 4.8. Suitably adjusted standard parameter-values found in the literature for Bi-substituted iron garnets are used for the thicker 153nm film[7, 24, 25]. In order to fit the data for the thinner samples, variations in all the relevant parameters, $\omega_p^2 f_{i\pm}$, ω_{i0}, Δ_i and Γ_i were explored. Reductions in the half-linewidth Γ_d for the higher-energy tetrahedral sub-lattice-transition are found for the 95nm-thick-film (a 19% reduction) and 46nm-thick-film (a 39% reduction). A 2% reduction in the octahedral sub-lattice resonant frequency ω_{a0} together with an 11% reduction in the corresponding octahedral half-linewidth Γ_a reproduces the 19nm-thick film MCD results. No significant departures in bulk Bi concentration through its effect on spin-orbit splitting or oscillator strength are detected. In summary, the model points to an enhancement in the lifetime of electronic excitations at reduced film thicknesses below ~100nm.

Evidence of longer decay rates and lifetime enhancement in electronic transitions in nanoscale structures has been reported in another material system[80]. The occurrence of a sharp enhancement in excitation state lifetimes may be attributed to surface effects. Further investigation of the surface contribution to the decay rate mechanism in ultra-thin garnet films is planned.

Chapter 5

Magneto-Optic Waveguide with Photonic Crystals

This chapter covers the research done on photonic stop band reconfiguration upon magnetization reversal in elliptically birefringent Bragg gratings (MPCs) waveguide. It is shown that for longitudinally-magnetized waveguides in magneto-optic films, the character of the orthogonal elliptically-polarized normal modes is strongly affected by magnetization reversal, impacting MPCs stop band configuration. The strongly reconfigured stop bands in a multimode MPC waveguide is due to the asymmetric back reflection of different-order waveguide modes from the fundamental mode. The findings discussed in this chapter were published in the journal[2] Phys. Rev. B 84, 094202, September 2011 and in a book chapter[3] of Springer publication, 2013.

To address the photonic stopband reconfiguration in one-dimensional magneto-photonic crystals, the chapter is divided into the following sections: the first section discusses the theory of elliptically birefringent media using a stacked model. The PC fabrication on the magneto-optic waveguide is presented in the subsequent section. Later sections discuss the optics required for MPC waveguide characterization and Stop-Bands measurement from 1D MPC. Finally, Bloch mode reconfiguration is demonstrated theoretically and experimentally in the fabricated PC structures.

---

[2] Reprinted (abstract/excerpt/figure) with permission from: A. Chakravarty, M. Levy, A. A. Jalali, Z. Wu, and A. M. Merzlikin, *Elliptical normal modes and stop band reconfiguration in multimode birefringent one-dimensional magnetophotonic crystals*, Phys. Rev. B 84, 094202 (2011). Copyright (2011) by the American Physical Society.

[3] With kind permission from Springer Science and Business: *Magneto-Photonic Bragg Waveguides, Waveguide Arrays and Non-reciprocal Bloch Oscillations*, Magnetophotonics, 2013 M. Inoue, M. Levy, A. V. Baryshev (Eds.), p. 135-161, M. Levy, A. Chakravarty, P. Kumar, and Xiaoyue Huang.

5.1 Theory of Elliptical Birefringent Periodic Medium: Stacked Model

In a birefringent MO waveguide, the electromagnetic wave equation can be written as [2, 3]

$$\left(k_0^2\tilde{\varepsilon} - k^2\mathbf{I} + \mathbf{kk}\right)\cdot\mathbf{E}_0 = 0\,, \tag{5.1}$$

where $\mathbf{E}_0$ is the plane wave amplitude, **kk** is a dyadic product of the wave vector, **I** is the 3×3 identity matrix, and $k_0^2 = \omega/c$. c is the speed of light in vacuum and ω is the angular frequency. The dielectric permittivity matrix $\tilde{\varepsilon}$ of the birefringent MO waveguide magnetized along the direction of light propagation (z-direction) has the form:

$$\tilde{\varepsilon} = \begin{pmatrix} \varepsilon_{xx} & \pm ig & 0 \\ \mp ig & \varepsilon_{yy} & 0 \\ 0 & 0 & \varepsilon_{zz} \end{pmatrix}. \tag{5.2}$$

In the above equation, $\varepsilon_{xx}, \varepsilon_{yy}, \varepsilon_{zz}$ and g are real-valued parameters, as this study relates to the experimental study performed for wave propagation in the ridge waveguide structure fabricated on bismuth-substituted-rare-earth iron-garnet films. These films have no optical absorption at the telecommunication band. With the magneto-optical gyrotropy parameterized by the off-diagonal components $\pm ig$, elliptical birefringence can be employed to the guide by considering $\varepsilon_{xx} \neq \varepsilon_{yy}$. Here, squares of the experimentally measured fundamental or high-order TE and TM mode indices from the film for its slab configuration are assigned for ε_{xx} and ε_{yy} , respectively.

In the waveguide, a monochromatic plane wave propagating parallel to the z axis for its normal incidence breaks down to elliptical eigenmodes. The eigenmodes and their phase speeds $v_{\pm}$ can be derived by solving the wave equation [2, 3], Eq. (5.1):

$$\hat{e}_{\pm} = \frac{1}{\sqrt{2}}\begin{pmatrix} \cos\alpha \pm \sin\alpha \\ \pm i\cos\alpha - i\sin\alpha \\ 0 \end{pmatrix} \tag{5.3}$$

$$\tan(2\alpha) = \frac{\varepsilon_{yy} - \varepsilon_{xx}}{2g} \tag{5.4}$$

$$v_{\pm} = c / n_{\pm} \tag{5.5}$$

$$n_{\pm}^{2} = \bar{\varepsilon} \pm \sqrt{\Delta^2 + g^2} \tag{5.6}$$

$$\bar{\varepsilon} = \frac{\varepsilon_{yy} + \varepsilon_{xx}}{2} \tag{5.7}$$

$$\text{and} \qquad \Delta = \left(\varepsilon_{yy} - \varepsilon_{xx}\right) / 2 \tag{5.8}$$

In Eq. (5.3) and Eq. (5.6), $\hat{e}_{\pm}$ and $n_{\pm}$ refer to the elliptical eigenmodes and their indices in the elliptically birefringent waveguide magnetized in the direction of light propagation. Formation of the elliptical normal modes in such ridge waveguide structure can be explained by understanding the response of the guide to the linear and the circular polarization states of an optical beam for its different magnetization conditions. A waveguide can be transversely magnetized by applying a magnetic field perpendicular to the direction of optical wave propagation. If the linear birefringence is present to the waveguide structure, then the normal modes of the waveguide are TE and TM, in the sense that they maintain their polarization state, as the wave propagates down the guide. The linear birefringence arises in a waveguide due to its structural asymmetry and creates TE and TM modes to acquire different phase speeds in the waveguide structure. However, for a magneto-optic waveguide which is longitudinally magnetized by applying a magnetic field parallel to the wave propagation direction, TE and TM modes can no longer be considered normal modes, as the optical gyrotropy comes into play. For longitudinal magnetization and without the linear birefringence, normal modes of such waveguides are RCP and LCP states due to the gyrotropy or the Faraday Effect. Combination of the linear birefringence to the gyrotropy in a MO waveguide combines the TE mode with RCP mode as shown in Figure 5.1(a) and thus produces a right-handed elliptical normal mode, which has a semi-major axis aligned with the previous TE mode. Similarly, another left-handed normal mode which has an axis aligned with the previous TM mode also gets produced due to the combination of the TM mode with LCP state in such a waveguide. Here, the TM

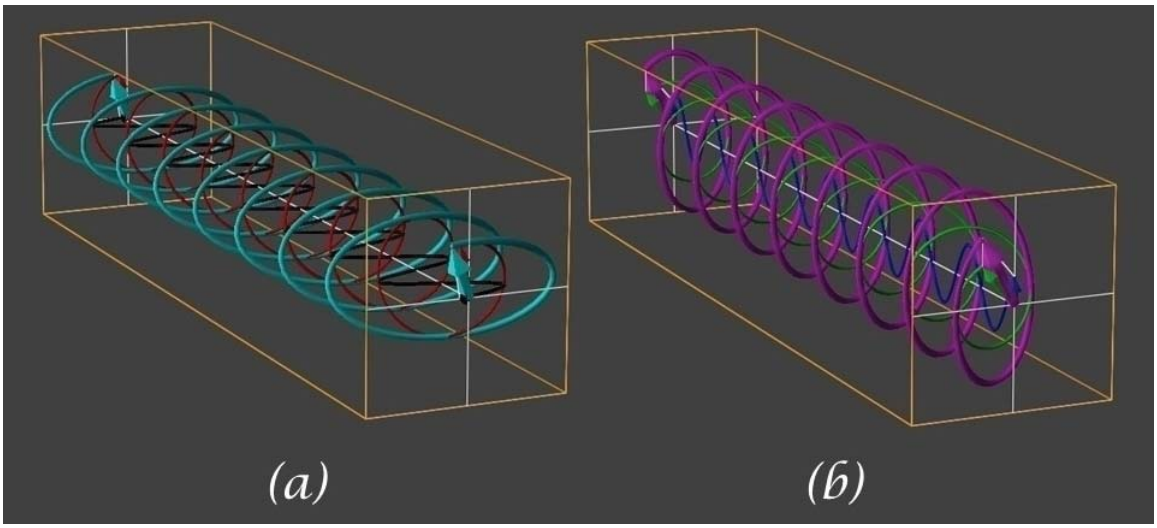

Figure 5.1 (a) Horizontal and (b) vertical normal modes arise in an elliptical birefringent medium due to the combination of linear birefringence with the optical gyrotropy in such a medium.

mode is 90° phase-shifted with the TE mode in the waveguide structure. Figure 5.1(b) shows a vertically oriented elliptical normal mode. The elliptical shape of these normal modes are decided by the original TE and TM modes of the transversely magnetized waveguide structure. The helicity acquired by the normal modes are determined by the RCP and LCP polarization states. Generally, a vertically-oriented left-elliptical normal mode has slightly higher ellipticity compared to the horizontally-oriented right-elliptical normal mode, as the TE mode in the described waveguide structure has slightly larger magnitude compared to the TM mode. However, the right-elliptical normal mode has slightly higher magnitude than its counterpart for the same reason.

When the magnetization direction is opposite to the direction of light propagation in such a waveguide, the gyration vector of the medium changes the precession direction and therefore, its magnitude becomes negative. This makes the dielectric tensor in Eq. (5.1) acquire both "positive" and "negative" signs in the non-reciprocal gyrotropic term. Reversed magnetization also changes α to $\frac{\pi}{2}-\alpha$ in Eq. (5.3) and therefore, eigenmodes of the waveguide structure acquire the reversed helicities compared to the previous eigenmodes. For the reversed magnetization direction, eigenmodes of the wave in Eq. (5.1) can be parameterized as [2, 3]

$$\hat{e}_{\pm}^{r} = \frac{1}{\sqrt{2}} \begin{pmatrix} \pm\cos\alpha + \sin\alpha \\ -i\cos\alpha \pm i\sin\alpha \\ 0 \end{pmatrix}, \tag{5.9}$$

where the superscript *r* indicates helicity reversal.

The effect of magnetization reversal on the normal modes of the MO waveguide structure can be demonstrated through a Poincaré sphere representation as it is shown in Figure 5.2. In circularly birefringent MO waveguides, normal modes of the structure take positions at the north and south poles of the Poincaré sphere. Due to the magnetization reversal in the waveguide structure, modes interchange their positions in the sphere. However, in an elliptically birefringent MO waveguide, normal modes take positions in the upper and lower hemisphere on the Poincaré sphere according to their helicities. Magnetization reversal on such waveguides yields new normal modes and takes positions on the sphere which are the mirror reflection of the previous positions through the equatorial plane.

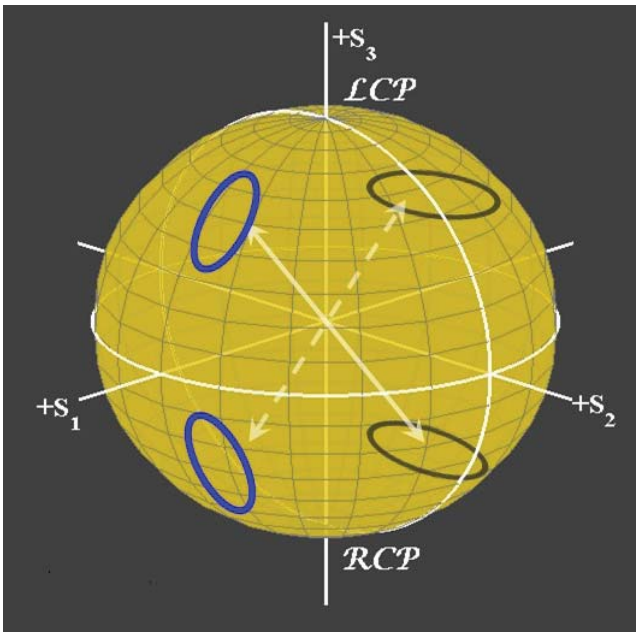

Figure 5.2 Magnetization reversal in elliptically birefringent MO waveguide pushes elliptical normal modes to the equatorial plane reflected positions (pointed by the dashed arrow) in a Poincaré sphere. Reprinted figure with permission from: ref. [2] Fig. 2

Levy and co-workers discussed the formation of stop bands in MPC in several of their publications [2, 3, 69-71]. Also, earlier in the subsection 3.2.2 of chapter 3, the mechanism

behind the stop band formation from a PC structure is discussed. There, it is pointed out that the optical wave suffers severe attenuation in its intensity due to the presence of PBG in an optical structure. Several PBGs are found from the artificially fabricated PCs on a multimode supporting ridge waveguide structure. In such PBGs, the fundamental waveguide mode of the ridge waveguide structure couples to the fundamental and higher waveguide modes accordingly, in first order contra-directional manner[2, 3]. The Bragg condition for this coupling to happen can be defined as

$$\lambda = (n_f + n_b)\Lambda\,, \tag{5.10}$$

where λ is the wavelength in vacuum, n_f and n_b are the mode indices of the forward-propagating and back-reflected modes, and Λ is the grating period. The phase matching between these modes as described in subsection 3.2.1 of chapter 3, also occurs due to this Bragg condition. Here, Bragg gratings actually provide the necessary spatial harmonics to

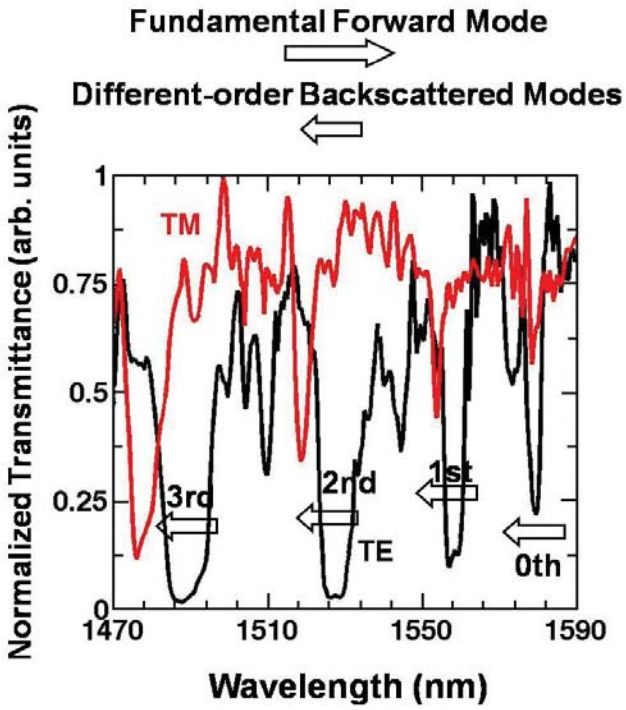

Figure 5.3 Measured multiple TE and TM stop bands (normalized to waveguide transmittance) in the presence of a transverse magnetic field, from the magneto photonic crystals fabricated on the ridge waveguide in an iron garnet film. Reprinted figure with permission from: ref. [2] Fig. 2

couple the two waveguide modes contra-directionally in the PC structure. Experimentally measured multiple stop bands from the PCs fabricated on a ridge waveguide in an iron garnet film are shown in Figure 5.3. Coupling between the waveguide modes in a multimode supporting ridge waveguide structure is studied by creating a theoretical model which consists of two layers with different optical properties. Relevant background for the model can be found in [2, 3, 69-71]. Diagonal components ε_{xx} and ε_{yy} of the model dielectric permittivity tensor in Eq. (5.2) are approximated by the squares of the experimentally measured fundamental or high-order TE and TM mode indices of a slab film. Adjacent layers of the stack are allowed to have index contrast for the representation of different ridge heights. This is adjusted in the diagonal components (TE and TM mode index values) of the dielectric permittivity tensors for the adjacent layers. The layers are made gyrotropic by assigning off-diagonal elements to the layer tensors. The model with this theoretical background is not constrained by the relative linear birefringence, gyrotropy, or thickness of the layers.

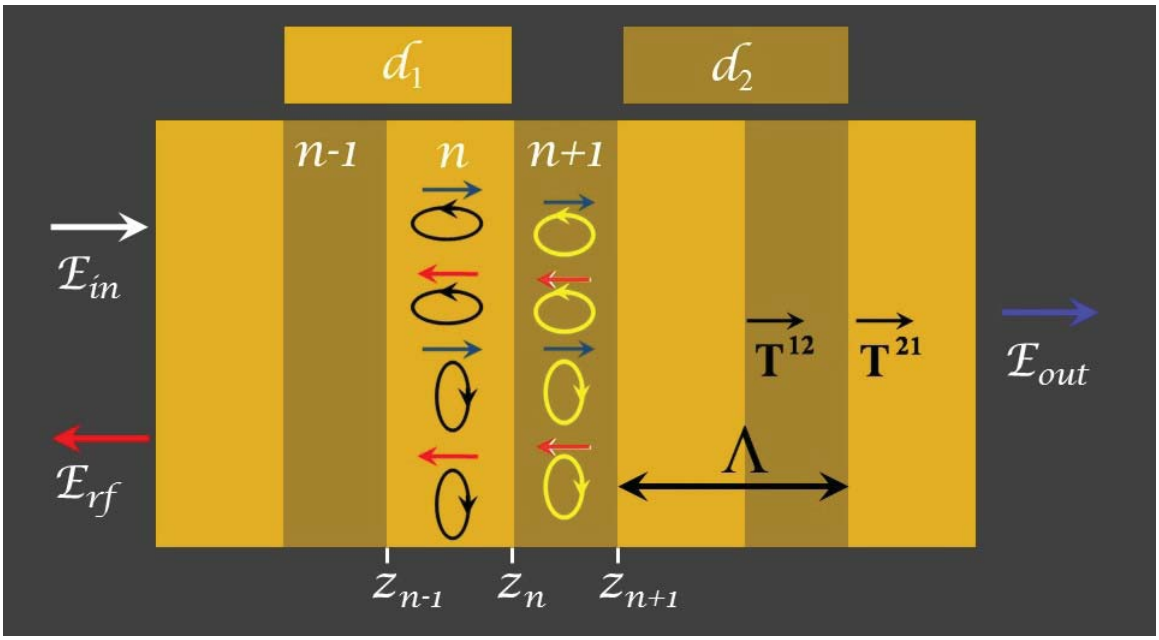

Figure 5.4 Stack model with two periodically varying elliptical birefringent layers of thicknesses d_1 and d_2. In each layer, propagation of an optical wave can be expressed by the local normal modes of the layer. Based on this model, a transfer matrix is formulated to calculate the transmittance from the full crystal.

The model considers normal incidence of a propagating wave in the periodic stack structure. To calculate the transmittance of the stack, a transfer matrix formulation can be built based on this model as shown in Figure 5.4 and is described in Refs [2, 3] . Initially, for an arbitrary layer *n* in the stack, the Bloch mode is formulated in terms of local elliptically-polarized normal waveguide modes in order to get an expression for the transfer matrix [2, 3]. Forward and backward traveling waves are allowed to correspond to different mode-orders to account for fundamental to high-order back-reflections. Thus, for any given layer *n* of the stack, the field vector is expressed as [2, 3]:

$$\begin{aligned} E(z,t) = \hat{e}_+^f E_{01} \exp(i\omega n_+^f (z - z_n)/c) + \hat{e}_+^b E_{02} \exp(-i\omega n_+^b (z - z_n)/c)... \\ \hat{e}_-^f E_{03} \exp(i\omega n_-^f (z - z_n)/c) + \hat{e}_-^b E_{04} \exp(-i\omega n_-^b (z - z_n)/c), \end{aligned} \tag{5.10}$$

where $i = \sqrt{-1}$ for a light-wave of frequency ω propagating in the z-direction[2, 3],[68-70]. Here, the superscripts *f* and *b* refer to the forward and backward propagating modes. The mode indices$n_\pm$ $n_\pm^{f,b}$ are assumed to correspond to local waveguide normal modes of opposite helicity. The E_{0j}, *j*=1-4 were partial-wave amplitude constants with z_n as the location of the interface between two arbitrary layers *n* and *n*+1 in the media. The elliptical polarization-state unit-vectors $\hat{e}_\pm^{f,b}$ in the form $\hat{e}_\pm(\alpha^{f,b})$, where the elliptically polarized waveguide normal modes propagate in the forward or backward direction, respectively, and is shown in Figure 5.4. Here, forward and backward propagating normal modes have different elliptical polarizations.

The transfer matrix is calculated by solving the wave propagation from one layer to the next and matching boundary conditions at the interface, for the two-layered unit cell with period Λ in Figure 5.4. The transfer matrix from layer *n*-1 to layer *n*+1 can be written as[65]:

$$\mathrm{T}^{(n-1,n+1)} = (\mathrm{P}^{(n+1)})^{-1}(\mathrm{D}^{(n+1)})^{-1}\mathrm{D}^{(n)}(\mathrm{P}^{(n)})^{-1}(\mathrm{D}^{(n)})^{-1}\mathrm{D}^{(n-1)}, \tag{5.11}$$

where $\mathrm{D}^{(n)}$ is the dynamic matrix, which helps transferring the forward and back reflected elliptical normal modes to propagate from the layer *n* to the *n*+1 layer. While the transfer process is happening, $\mathrm{P}^{(n)}$ describes the phase matrix, which contains the information of

the phases acquired by these four normal modes. For layer *n*, these matrices in the Eq. (5.11) have the following forms[65]:

$$\mathbf{D}^{(n)} = \begin{pmatrix} \cos\alpha_f^{(n)} & \cos\alpha_b^{(n)} & -\sin\alpha_f^{(n)} & -\sin\alpha_b^{(n)} \\ n_{+,f}^{(n)}\cos\alpha_f^{(n)} & -n_{+,b}^{(n)}\cos\alpha_b^{(n)} & -n_{-,f}^{(n)}\sin\alpha_f^{(n)} & n_{-,b}^{(n)}\sin\alpha_b^{(n)} \\ \sin\alpha_f^{(n)} & \sin\alpha_b^{(n)} & \cos\alpha_f^{(n)} & \cos\alpha_b^{(n)} \\ n_{+,f}^{(n)}\sin\alpha_f^{(n)} & -n_{+,b}^{(n)}\sin\alpha_b^{(n)} & n_{-,f}^{(n)}\cos\alpha_f^{(n)} & -n_{-,b}^{(n)}\cos\alpha_b^{(n)} \end{pmatrix}$$

$$\mathbf{P}^{(n)} = \begin{pmatrix} \exp(-i\frac{\omega}{c}n_{+,f}^{(n)}d_n) & 0 & 0 & 0 \\ 0 & \exp(i\frac{\omega}{c}n_{+,b}^{(n)}d_n) & 0 & 0 \\ 0 & 0 & \exp(-i\frac{\omega}{c}n_{-,f}^{(n)}d_n) & 0 \\ 0 & 0 & 0 & \exp(i\frac{\omega}{c}n_{-,b}^{(n)}d_n) \end{pmatrix}.$$

In the phase matrix $\mathrm{P}^{(n)}$, d_n is the thickness of layer *n*.

The transfer matrix for the full crystal can be obtained by repeated multiplications of the two-layered transfer matrix and can be written as

$$\mathrm{T} = \left(\mathrm{T}^{12}\mathrm{T}^{21}\right)\left(\mathrm{T}^{12}\mathrm{T}^{21}\right)\left(\mathrm{T}^{12}\mathrm{T}^{21}\right).....,\tag{5.12}$$

where $\left(\mathrm{T}^{12}\mathrm{T}^{21}\right)$ represents one periodic distance, Λ, transfer of the forward and the back reflected elliptical normal modes from layer 1 to 2 and then layer 2 to 1 in the crystal, as shown in Figure 5.4. To calculate the transmittance of a propagating wave from the full crystal, the propagating wave is first converted accordingly to the frame of reference of the elliptical normal modes in layer 1. The transfer of the propagating wave through the full crystal is given by following equation:

$$\begin{bmatrix} T_{11} & T_{12} & T_{13} & T_{14} \\ T_{21} & T_{22} & T_{23} & T_{24} \\ T_{31} & T_{32} & T_{33} & T_{34} \\ T_{41} & T_{42} & T_{43} & T_{44} \end{bmatrix} \begin{bmatrix} E_{e1}^{i} \\ E_{e1}^{r} \\ E_{e2}^{i} \\ E_{e2}^{r} \end{bmatrix} = \begin{bmatrix} E_{e1}^{t} \\ 0 \\ E_{e2}^{t} \\ 0 \end{bmatrix} \tag{5.13}$$

where E_{e1}^{i} , E_{e2}^{i} , and E_{e1}^{r}, E_{e2}^{r} are the electric field amplitudes of the forward and backward propagating elliptical normal modes, respectively. Forward mode electric field amplitudes are obtained by expressing the incident propagating wave into the normal mode coordinates of the system. Backward field amplitudes are the result of the matrix operation. The transmission spectrum of the full crystal is calculated using the amplitudes of the transmitted intensities from Eq. (5.13) as

$$\text{Transmittance} = \begin{bmatrix} E_{e1}^{t} & E_{e2}^{t} \end{bmatrix} \begin{bmatrix} \left(E_{e1}^{t}\right)^{*} \\ \left(E_{e2}^{t}\right)^{*} \end{bmatrix}. \tag{5.14}$$

Based on the model, a MATLAB code is developed to mimic the transmittance spectra found by measuring the transmittance of a PC structure in the experimental studies discussed later in this chapter. The code is tested with conditions such as transmittance for a linear birefringent medium, a circularly birefringent medium, and a medium without any birefringence. All the tests produce physically realistic results. The theoretical transmittance spectrum produced by the MATLAB code has very good agreement with the experimental results and is discussed later in subsection 5.4.2. The code is given in Appendix 4.

5.2 PC Fabrication on the Magneto-Optic Waveguide

The step involved in the fabrication of the magneto-optic waveguide and the PC for this dissertation are already discussed in section 3.2 of chapter 3. However, the details about the fabrication process were not covered in that section. This section discusses the

experimental details on the fabrication process of the ridge waveguide structure followed by PC fabrication by patterning an iron garnet film.

To fabricate the ridge waveguide on an iron garnet film, a positive photo-resist Rohm & Haas SC1827^{TM} is first spin-coated on the sample using hexa-methyl-disilazane (HMDS) as an adhesive layer. Spin-coating is done in two spin-step processes: 500 rpm to get a thicker layer of the resist on top of the film followed by 2000 rpm for creating a required uniform thin layer from that thicker layer. After resist coating, the layer is hardened by heating the substrate for 4 minutes at a temperature of 100°C. An Electronic Vision Group (EVG) 620 mask aligner integrated with the 365 nm wavelength I-line UV source is used to align the ~ 1 to $2\ \mu m$ -thick photo-resist layered sample under the light source for 10-15 seconds at a 15-20 mW/cm^2 ultra-violet power density. A mask with line-widths ranging from 1 to $10\mu m$ is used for ridge waveguide fabrication. After exposing the photo-resist layer to the UV light via soft contact, the substrate is developed in a Rohm & Haas MF319^{TM} solution followed by 20 minutes of post-baking at 100°C. Following the photolithography steps, ion beam-milling transfers the ridge waveguide pattern into the iron-garnet film. An argon-ion plasma source is used for ion beam milling at 700 V, 170-210 μA/cm^2 current density, 10-20 sccm argon gas flow-rate and $8\times10^{-5} - 4\times10^{-4}$ Torr pressure. In these process conditions, ion plasma, at the etch rate of ~14 nm/min,

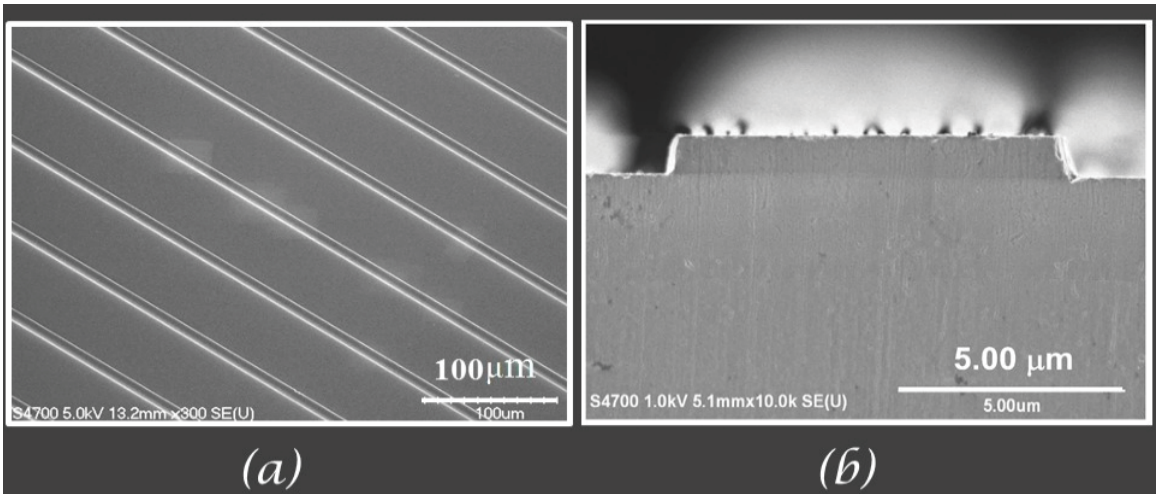

Figure 5.5 SEM images of (a) ridge waveguide structures and (b) a mirror polished ridge waveguide facet fabricated on iron garnet film. With kind permission from Springer Science and Business ref. [3] Fig. 6.1

etches the iron garnet film for approximately 45 minutes to produce 600-700 nm ridge height on the film. The post-milling process involves removing the left-over resist by using acetone, isopropanol and de-ionized water. Ion beam milling produces sidewall damage to the fabricated waveguide structures. Therefore, to address this issue, the sample is dipped into an ortho-phosphoric acid bath for 12-15 seconds at 100°C. After this chemical etching step, the substrate is then rinsed thoroughly in de-ionized (DI) water.

For optical testing, the input-output facet ends of a ridge waveguide must be mirror-polished. To achieve a mirror finish facet, the end of a waveguide is sequentially polished with diamond lapping films of grain coarseness 30, 9, 3, 1 and $0.3\ \mu m$, respectively. SEM images of several ridge waveguides and the cross-section of a waveguide after facet polish--ing are shown in Figure 5.5.

Fabrication of 1D PC on a ridge waveguide involves mask-free milling, using the focused ion beam technique. A focused beam of gallium ions with an acceleration energy of 30 keV scans over the surface of a ridge waveguide along the waveguide direction according to the PC structure drawn in CAD. The vector patterning method from the NPGS control system installed in the Hitachi FB-2000A FIB system is applied in the PC structure fabrication. The reported FIB system has a single beam and variable aperture settings. Two beam modes, M1 for working beam and M0 for imaging beam, are available in the system to assist the sample patterning. Initially, the M0 beam mode with aperture settings of $50\ \mu m$ is used for selecting a milling area of $250 \times 250\ \mu m^2$ in PC fabrication on a ridge waveguide. In this setting, the beam current and beam diameter can be read as 0.02-0.05 nA and 60 nm, respectively. Here, the PC structure aimed for fabrication has the following specifications: $10\ \mu m$ in-width, $200\ \mu m$ in-length, and 600 – 700 nm in-depth. The center-to-center groove spacing for 100nm thick grooves in the PC structure is selected anywhere in the range of 335 –350 nm. For milling the ridge waveguide surface, the M1 mode with $100\ \mu m$ aperture settings is selected. The beam current and beam diameter of this configuration are 0.4 –0.8 nA and 60 nm. Ideally, the following parameters are chosen in NPGS for PC fabrication: continuous mode writing, center-to-center beam spacing and beam line-spacing 4.12 nm, single scan, beam dual time $0.001\ \mu Sec$ and $60 - 80\ \mu C/cm$

line-dose. Here, the parameter selections are based on a balance between the milling time and the desired depth. With the selection, the 60 nm diameter beam in FIB and 4.12 nm center-to-center beam distance and line spacing in NPGS creates almost 90% overlapping of the two successive milled spots and about the same overlapping between the two successive milled lines. Therefore, the milling process is highly smooth. Usually, the FIB system takes 40 – 45 minutes to fabricate such PC structure on an iron garnet based ridge waveguide. It is crucial to note here that the beam current in the FIB system should not vary while the PC fabrication process is on: if the beam current changes, then the shape and the focus of the beam on the milling surface changes drastically. This can result in a misaligned or underdeveloped PC structure. In some cases, differed beam current result in zero milling and thereby create no structure on the sample. SEM images of the PC structure on a ridge waveguide fabricated on iron garnet film is shown in Figure 5.6.

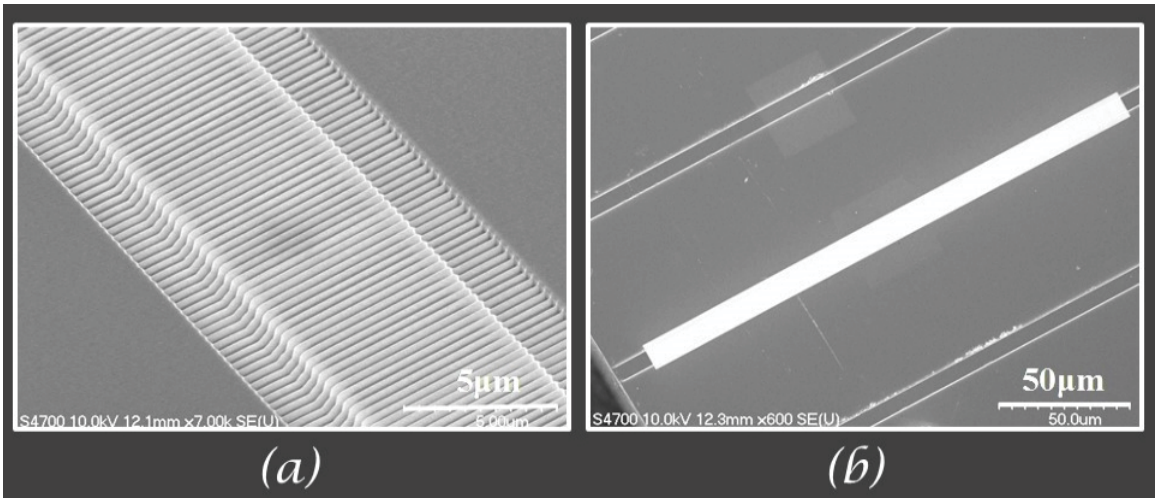

Figure 5.6 (a) Photonic crystal structure, reprinted figure with permission from: ref. [2] Fig. 4 and (b) photonics crystals (white) with ridge waveguide structure fabricated on iron garnet film.

Material re-deposition, Ion implantation and sidewall damage are some of the common issues that arise in PC fabrication from the FIB ion beam milling. These ambiguities in the PC structure hinder its optical performance. To address these issues, a fabricated sample is immersed in the ortho-phosphoric bath at 75°C for 10~15 seconds and after that rinsed in DI water. It is seen that this post treatment step in the PC fabrication process enhances the PCs' optical performance remarkably.

5.3 Optics for the MPC waveguide characterization

The performance of a ridge waveguide or a ridge waveguide with PC fabricated on iron garnet film is tested by measuring optical transmittance through the structure. To do the optical transmittance measurements, a single mode optical fiber is connected to a 1480 – 1580 nm tunable laser source (Ando AQ4321A) via an Agilent 11896A polarization controller as shown in Figure 5.7. This single mode fiber with a lensed tip produces a $2\ \mu m$ spot size and has a working distance of $3\sim5\ \mu m$. The laser has a 7.9 mW (9 dBm) maximum and 0.079 mW (-11 dBm) minimum output power with a capability of 0.001 nm wavelength resolution. The polarization controller in between the fiber and the laser is used to adjust the birefringence of the single mode fiber. Therefore, any desired output polarization state from the linearly-horizontal or quasi-TE, linearly-vertical or quasi-TM, circular or elliptical polarization states can be produced from the fiber depending on the experimental requirement. To prepare the transverse polarization states, a motorized rotatory Glan-Thompson polarization analyzer with sub-degree precision is used. For preparing the elliptical or circular polarization states, a quarter wave-plate with the center wavelength of 1550 nm, useable within ±30 nm wavelength window, is used along with this polarization analyzer. A separate subsection 5.3.1 discusses the preparation of the polarization state of a beam, specifically the elliptical polarization state, using this fiber, polarization controller, and laser assembly. After preparation of the required polarization state, the direct end-coupling method as described in the section 3.3 of chapter 3 is applied to couple the polarized light from the fiber to the waveguide structure. The waveguide output beam is then collected by a 10x microscope objective and it focuses the beam at a 50% non-polarizing beam-splitter. The beam splitter splits this focused beam into two parts and one beam is directed into an infrared photo-detector connected to a Newport power meter. This power meter can measure as low as 20nW optical power intensity. With such power measurement capability, the power meter records the transmittance intensities emerging from the waveguide as a function of wavelength. A LabVIEW interface to the laser source and the power meter is used here to do the real-time measurements by driving the wavelength scan in the laser source and measure the optical intensity at the power meter

simultaneously. Sometimes, to analyze the polarization state of the waveguide output, a full 360° analyzer scan on the output intensity is performed with the Glan-Thompson polarizer. The other beam from the beam splitter is directed to an infrared Hamamatsu recording camera and monitors the output spot shape and intensity. The measurement set-up for optical characterization of the ridge waveguide and PC structure is shown in the schematic of Figure 5.7.

Generally, the above discussed optical transmittance and polarization measurements are done in the presence of an applied magnetic field parallel to the optical propagation which magnetized the ridge waveguide structures along their axes. To magnetize the waveguide structures, the sample is placed on an 8 mm by 25 mm rectangular neodymium bar-magnet

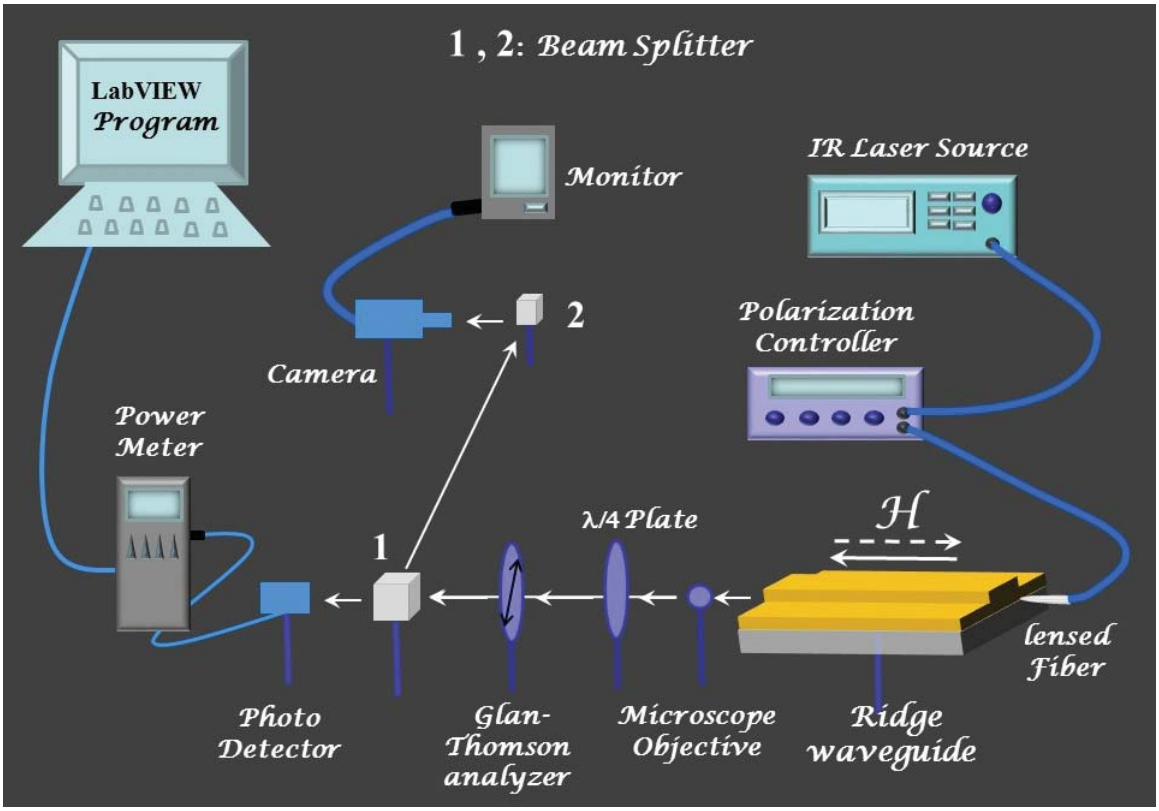

Figure 5.7 The optical transmittance spectrum of a ridge waveguide structure is recorded using a digital power meter and a 1480 –1580nm laser source. Polarization output from the lensed fiber is prepared using the rotating Glan-Thomson analyzer and a $\lambda/4$ plate in the absence of a sample. In transmission measurement, these two components are removed, but the ridge waveguide sample is mounted in line with the lensed fiber for direct-end coupling.

of 2 mm thick plate fitted to the sample stage. The return flux oriented collinear to the ridge waveguide axis (north and south poles collinear to the waveguide input and output facets) produces 300 Oe magnetic field and saturates the in-plane magnetization of the iron garnet film. If an experiment requires reversed or transverse magnetization, then this bar magnet is rotated to 180° or 90° with respect to the sample, while keeping the same orientation of the sample to the input beam as in the previous configuration.

5.3.1 Elliptical beam preparation

In the optical testing of the MO waveguide and the MPC waveguide, linear polarization states are prepared by using a polarization controller, a linear polarizer, and a beam-collimator. As discussed earlier in section 5.2, the optical beam from an IR tunable laser source first goes to a polarization controller, and then to a lensed fiber that is coupled to the output of the controller. From here, a beam collimator partially focuses the lensed fiber output to a Glan-Thompson polarization analyzer with 1:4000 power extinction capacity. In this configuration, the polarization controller box is adjusted in such a manner that it

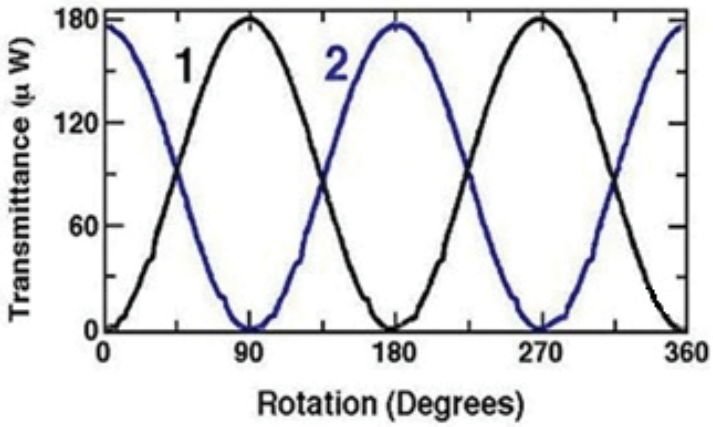

Figure 5.8 A 360° analyzer scans of TE (curve 1) and TM (curve 2) polarization states.

minimizes the laser beam intensity to ~35 nW (dark reading) for the analyzer axis either in vertical or horizontal direction. Thus produced polarization states can be confirmed by a total of 360° analyzer scan over the lensed fiber output beam intensity. Figure 5.8 shows a scan of TE and TM linear polarization states produced via rotating the Glan-Thomson

analyzer axis to 360° with an angular step of 0.1°. Here, the analyzer axis position was in vertical direction at the start of the scan.

In preparation of an elliptical polarization state, the quarter-wave-plate's fast axis orientation determines the elliptical orientation of the optical beam. To configure the input beam ellipticity (the ratio of the semi-minor to semi-major axes amplitudes of the polarization ellipse), the Glan-Thomson polarization analyzer is placed after the quarter-wave plate. In this configuration, the polarizer axis is allowed to make an angle θ with respect to the quarter wave plate fast axis in vertical or horizontal direction. Similar to preparing the linear polarization state, emergent transmitted light from these two optical components is then also minimized by using the polarization controller box. Thus, the elliptical polarization coming out of the aforementioned configuration acquires an ellipticity $\tan\theta$ and oriented $\frac{\pi}{2}-\theta$ to vertical or horizontal direction of the quarter wave-plate fast axis. Again, the conjugate helicity state of this polarization state is prepared similarly by rotating the polarization axis to $\pi-\theta$ angle, however keeping the direction of the quarter wave plate axis unchanged. Therefore, in this technique, one elliptical polarization state is prepared by suppressing the other. For example, a right handed vertical elliptical polarization state can be created only when the left-handed horizontal elliptical polarization state is destroyed.

After preparing the required elliptical polarization state by the above mentioned technique, an ellipticity check is done by a 360° analyzer axis scan over the lensed fiber output beam intensity, similar to the method employed for the linear polarization state confirmation. The measured ellipticity of a beam is given by the following expression:

$$Ellipticity = \sqrt{\frac{I_{\min}}{I_{\max}}}, \tag{5.15}$$

where $I_{\min}$ and $I_{\max}$ are the measured minimum and maximum intensities of the laser beam that denotes the semi-minor axis orientation of the elliptical polarization state. Figure 5.9 is a scan of 26° horizontal and vertical elliptical polarization states produced via rotating the Glan-Thomson analyzer axis to 360° with an angular step of 0.1°.

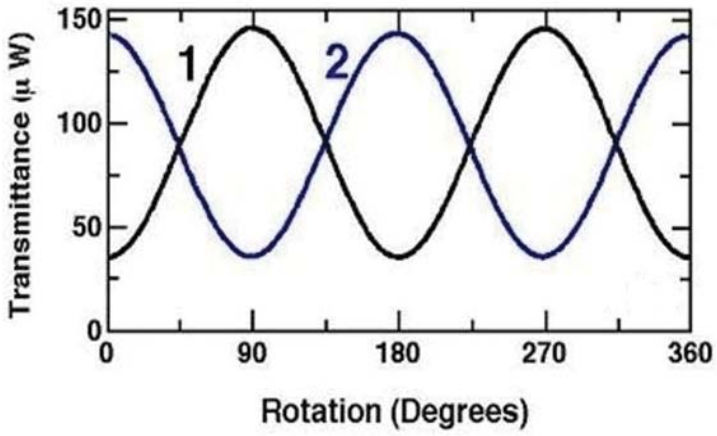

Figure 5.9 A 360° analyzer scan of 26° ellipse with semi-major axis orientation in horizontal (curve 1) and vertical (curve 2) directions.

To determine the helicity of the lensed fiber output, Stokes parameters are measured. From all the four Stokes parameters $S_j\,(j=0-3)$, the sign of S_3 determines the helicity of the propagating beam. In a Poincaré sphere representation, a beam with the polarization coordinate (s_1, s_2, s_3) for normalized Stokes parameters $s_j = \frac{S_j}{S_0}$ is located in the upper hemisphere if S_3 is positive and polarized counter-clockwise with respect to the source, or clockwise with respect to the detector (positive helicity). For a negative value of S_3, the beam carries the opposite (negative) helicity.

Experimentally, S_3 can be measured using a quarter-wave plate and a linear polarizer. The beam intensity $I(\theta,\varphi)$, where θ,φ are the linear polarizer axis and quarter-wave plate fast axis orientations, respectively, is first measured with just the linear polarizer at $\theta = 0°$ and 90°. Subsequently, it is measured by inserting the quarter-wave plate ($\varphi = 90°$) into the beam path with the linear polarizer set at $\theta = 45°$. S_3 is given by

$$S_3 = I(0°,0°) + I(90°,0°) - 2I(45°,90°). \tag{5.16}$$

5.4 Stop-Bands of normal modes from 1D MPCs

The experimental study of the magnetic tuning of stop bands in an elliptically birefringent

medium is performed by fabricating MPCs on the ridge waveguide structure. A monocrystalline bismuth-substituted-rare-earth iron-garnet film grown by the LPE technique on GGG substrates with (100) in plane direction is utilized for patterning. Measured FR from such a film with composition $Bi_{0.8}Gd_{0.2}Lu_{2.0}Fe_5O_{12}$ and 2.7 μm thickness was recorded to be 83°/mm. Here, FR measurement was done using a rotating polarizer and lock-in amplifier, across the thickness of the sample in un-patterned films at 1550 nm wavelength. The ridge waveguide structure with 6 μm wide and 600 nm ridge height are patterned on the film by standard photolithography followed by plasma etching. The typical length of a ridge waveguide is ~ 1.0 to 1.5 mm. PCs with 200 μm long Bragg gratings, 343.3 nm period, and 700 nm groove depth are focused-ion-beam-milled into these ridge waveguides. The PC structure is fabricated approximately 100 μm away from the output facet of the ridge waveguide. Waveguide input and output sides are polished down to a 0.3 μm-grain diamond lapping-film finish. Two samples are fabricated in $Bi_{0.8}Gd_{0.2}Lu_{2.0}Fe_5O_{12}$ film and three Bragg filters are used for stop band tuning test. All the testing yields mutually consistent results.

The prism coupler technique is utilized for determining the refractive indices of waveguide modes of the film and is conducted before surface patterning of the film. Four TE modes with refractive indices 2.2930, 2.2497, 2.1781, and 2.0765, respectively, were recorded from the film for its slab configuration. The TE and TM mode index difference, measured for the first four modes, are 0.0005, 0.0047, 0.0120 and 0.0210, respectively.

5.4.1 Normal mode response to a ridge waveguide

Applying a longitudinal magnetic field along the direction of the waveguide axis triggers optical gyrotropy at the telecommunication bandwidth in a MO ridge waveguide structure fabricated in an iron garnet film. Optical gyrotropy in conjugation with linear birefringence allows to couple a quasi-TE mode with a quasi-TM mode in such waveguide structure. Therefore, the normal modes of the MO waveguide become elliptically polarized with contrast to the quasi-TE and quasi-TM normal modes for its transverse magnetization configuration. Shape anisotropy, lattice mismatch strain and magnetic anisotropy play a role in establishing the elliptical birefringence in such a waveguide structure. In a gyrotropy

activated MO waveguide, orthogonal opposite-helicity states propagate at different phase speeds through the guide structure. Elliptically polarized inputs with matching elliptical shape and helicity with normal modes suffer minimal change in their states while travelling through the guide as discussed below.

Elliptical normal modes of a MO ridge waveguide structure can be calculated according to the theoretical formulation presented earlier in section 5.1. Here, the diagonal elements ε_{xx} and ε_{yy} of the dielectric permittivity tensor are approximated with the refractive index square of experimentally measured fundamental or higher order TE and TM modes of slab film. In a transversely magnetized ridge waveguide, fundamental TE and TM modes from the slab are considered normal modes of the structure. The elliptical polarization and mode indices for longitudinal magnetization are obtained by solving the dielectric permittivity eigenvalue problem in the presence of optical gyrotropy. This approach allows to calculate the theoretical elliptical normal mode of the MO waveguide in its longitudinal configuration. Based on this calculation, these polarization states are prepared later in order to test the optical response of the normal modes to the waveguide, using the principle described in subsection 5.3.1.

In the optical test, the ridge waveguide structures on a sample are magnetized, applying a saturation magnetic field of 300 Oe collinear with the waveguide axis in forward and backward directions. These waveguides are fabricated in $Bi_{0.8}Gd_{0.2}Lu_{2.0}Fe_5O_{12}$ films. The ridge waveguide structures selected to study the elliptical normal mode response are shown earlier in Figure 5.5(a). These waveguides are $6\ \mu m$-wide and do not have the Bragg gratings on them. Elliptical polarization states for testing these waveguides are prepared according to the normal mode theory in section 5.1 and using the optical setup shown in Figure 5.7. From the measurement it is found that an elliptical normal mode propagates with the minimal changes to its polarization state over the waveguide distance of ~1.2 mm.

According to the FR and the linear birefringence between the fundamental TE and TM modes in the $Bi_{0.8}Gd_{0.2}Lu_{2.0}Fe_5O_{12}$ film, the elliptical normal mode with ellipticity ~25.64° is prepared optically. The prepared input vertical elliptical normal mode (Stokes parameter, $s_3 = 0.48$) and its conjugate helicity mode ($s_3 = -0.48$) have the same ellipticity and are

shown in 360° analyzer scans in Figure 5.10(a), where 0° and 180° correspond to the orientation of the semi-minor axis. These elliptical polarizations are launched into a ~1.2 mm long waveguide structure for normal mode check purpose. The outputs of these modes presented in Figure 5.10(b) show that the elliptical normal mode travels through the waveguide with very minimal deviations of less than 8^{o} ($\Delta s_3 \leq 0.05$) in semi-major axis orientation over a 1.2 mm waveguide length. However, Figure 5.10(b) shows that the reversed helicity mode severely deviates from the input. Normal mode tests are done across the wavelength range 1525 nm±5 nm and these tests reveal that their polarization state remains largely wavelength independent.

In addition to the normal mode analysis, the normal mode is tested by reversing the

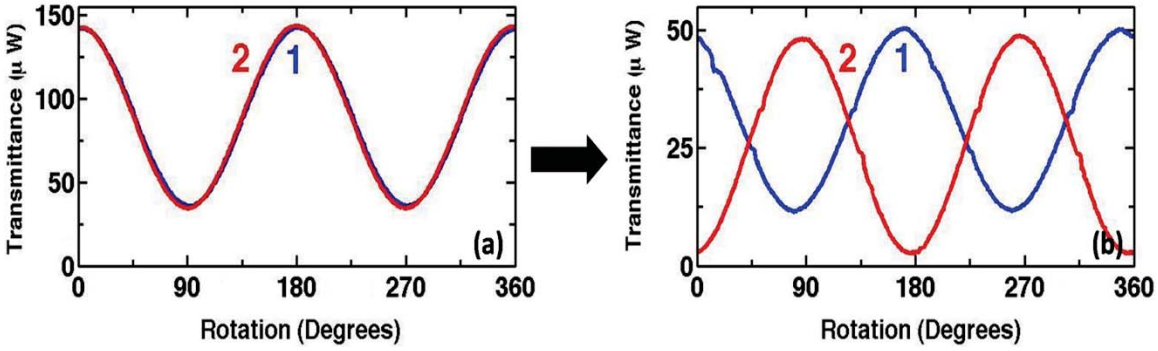

Figure 5.10 A 360° analyzer scans show that the elliptical normal mode (curve 1) and its conjugate helicity mode (curve 2) have a semi-major axis orientation overlap at the input (a) of a plain ~1.2 mm long waveguide, however they differ significantly at the output (b). The normal mode (curve1) maintains its elliptical shape and orientation. Reprinted figure with permission from: ref. [2] Fig. 5

magnetic field on the waveguide structures. Upon reversal of the magnetic field, the conjugate reversed helicity mode propagates through the waveguide with a minimal change to its original state, whereas the normal mode from the previous configuration changes significantly in its polarization state. This confirms that normal modes are in magnetization-direction and helicity dependent.

5.4.2 Impact of magnetization reversal on the normal mode stopband

In the subsection 5.4.1, the preparation of an optical beam to normal mode configurations

of a ridge waveguide is already described. With these elliptical normal mode polarization states, the transmittance spectrum from MPCs on the ridge waveguide are measured. For these optical transmittance measurements, MPCs that are sitting 100 μm away from the output facet of the waveguide are selected. Normal mode polarization states are launched from the feeder side of the ~1.2 mm long waveguide to the MPCs. The selected PBGs for normal mode transmittance measurements are the same PBGs where the stop bands for TE and TM modes in transverse magnetization appear from a MPC. This was shown earlier in the Figure 5.3 of the theory section 5.1 of this chapter. It was explained that stop bands occur due to the contra-directional coupling between the fundamental to higher order waveguide modes. In this subsection, normal mode transmittance for a fundamental forward-mode to second-order backscattered mode stop bands are chosen for demonstration purpose. For this purpose, the normal mode polarization states are prepared at the center-wavelength of the TE stop band with the method explained earlier. The normal modes prepared at this wavelength have very minimal deviation from their input polarization states across a wavelength range of ±20 nm from the center-wavelength. It shows that the stop band of horizontally oriented elliptical normal mode has larger detuning compared to its counterpart. This is due to the larger birefringence in the higher order normal modes.

Measured normal mode transmittance for a fundamental forward-mode to second-order backscattered mode stop bands are plotted in Figure 5.11. For the magnetization direction in light propagation direction, Figure 5.11(a) displays the stop bands that have been measured by the two elliptically-polarized normal mode beams over the TE and the TM stop bands (transverse magnetization). It is mentioned earlier in section 5.4.1 that magnetization reversal impacts the normal modes by changing the helicities of their conjugates. Therefore, when the normal mode helicities with magnetization reversal are changed simultaneously and thereby measured, the above mentioned stop bands remain largely unaltered in Figure 5.11(b).

Magnetization reversal affects the normal mode polarization states of a ridge waveguide by transmuting the normal modes into the hybrid modes in the feeder section of the waveguide. If the previous normal modes are allowed to measure the normal mode stop

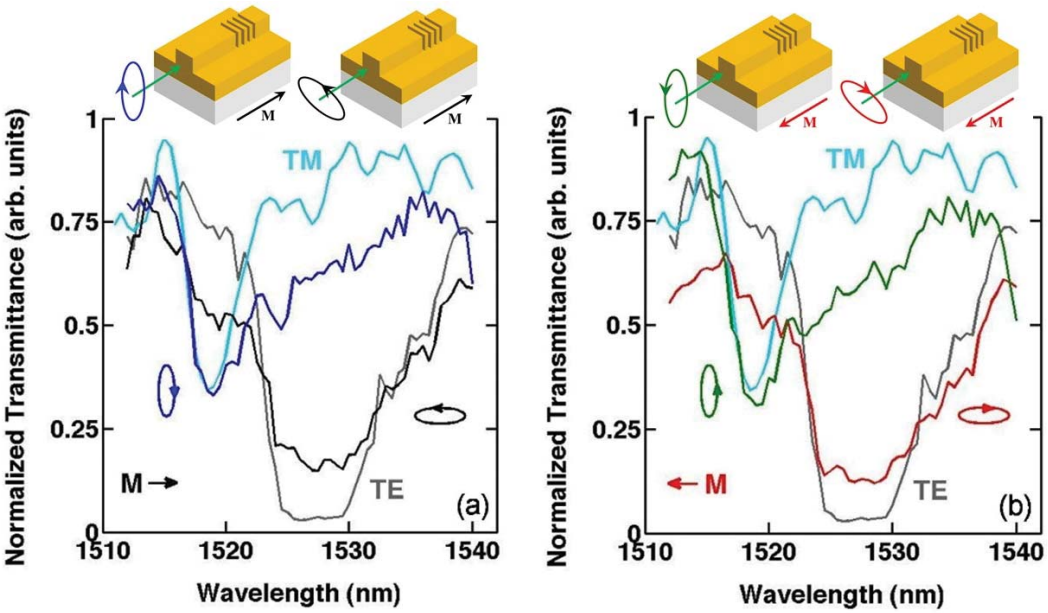

Figure 5.11 Forward fundamental to second order-mode back-reflected stop bands (normalized to the transmittance of a plain waveguide) for horizontally and vertically-oriented elliptical normal modes in a longitudinal magnetic field, (a) in beam propagation direction and (b) opposite to propagation direction. Magnetic field reversal converts the conjugate helicity modes to normal modes. TE and TM stop bands are in the plots for comparison. With kind permission from Springer Science and Business: ref. [3] Fig. 6.10

bands, it becomes apparent that these stop bands undergo very strong reconfigurations. These converted mode stop bands spectra were also recorded for the fundamental to second order back-reflected modes as it was done previously, and the stop band reconfiguration is plotted in Figure 5.12. In Figure 5.12(a) and Figure 5.12(b), the black and blue curves represent the transmittance profiles of the horizontal and vertically-oriented normal mode, respectively.

In those figures, the red (Figure 5.12(a)) and the green (Figure 5.12(b)) curves were obtained after magnetization reversal for the same horizontal and vertical inputs. In other words, very large spectral detuning of the stop bands due to the magnetization reversal is recorded in these measurements. Mode conversion into the reverse-helicity normal mode in the waveguide feeder section is almost complete, as the stop band shifts to the one corresponding to that mode.

From the above experimental measurements, Figure 5.13 shows that a change in magnetization direction together with the change of horizontal normal mode helicity from

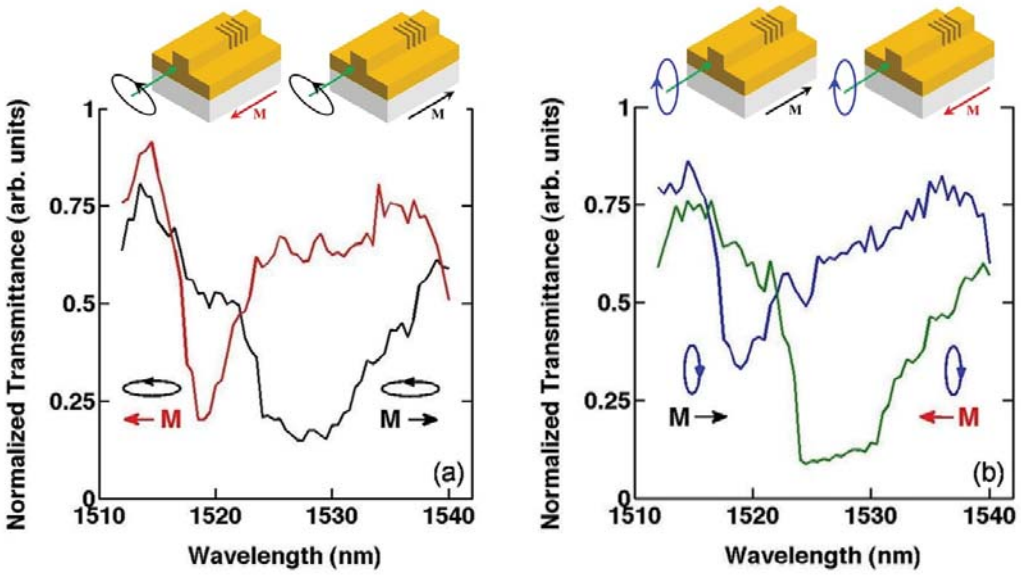

Figure 5.12 Forward fundamental to second order-mode back-reflected stop bands for elliptical normal-modes (black and blue curves) and their conjugate helicity modes (red and green curves), normalized to the transmittance of a plain waveguide. With kind permission from Springer Science and Business: ref. [3] Fig. 6.11

positive to negative and from negative to positive for the vertical normal mode together reestablishes the original spectral response to MPCs by the normal modes. This occurs to

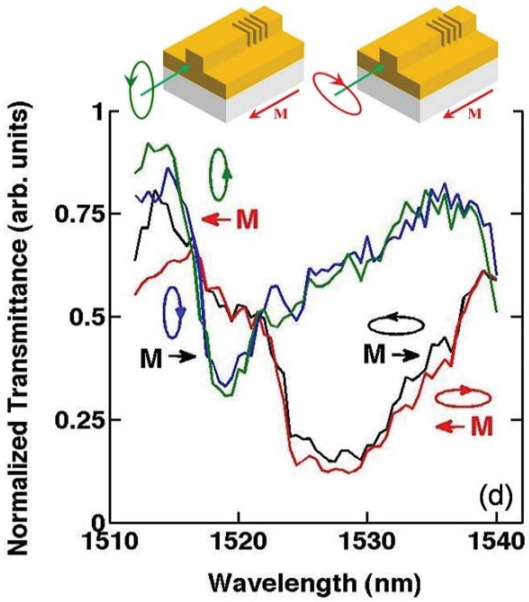

Figure 5.13 Simultaneous reversal of helicity (and magnetization) reproduces the forward fundamental to second order-mode back-reflected stop bands spectra for vertical and horizontal normal modes. With kind permission from Springer Science and Business: ref. [3] Fig. 6.11

regain their normal-mode character and yields unchanged stop bands. These measurements are performed for three different MPCs on different samples of $Bi_{0.8}Gd_{0.2}Lu_{2.0}Fe_5O_{12}$ film. Similar results are found from each of the sample.

These experimental results match well with stop band calculations based on the theoretical model presented in section 5.1, as shown in Figure 5.14. The model calculates these stop bands according to the experimental parameters such as stack number 600, lattice constant of a stack unit cell 343.7 nm, normal modes with 25.64°, layer 1 with thickness 45% of the period, 83°/mm Faraday rotation at 1550 nm wavelength, fundamental and second order waveguide TE and TM mode indices etc. The difference between experimental and modeled back-reflection contrast for vertically and horizontally-

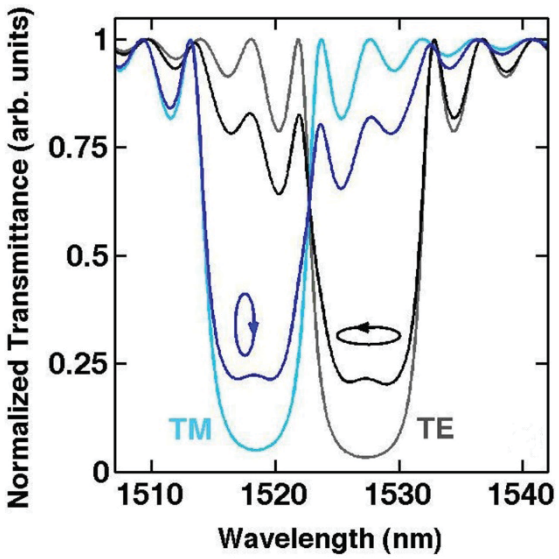

Figure 5.14 Calculated fundamental forward to second order-mode back-reflected stop bands for opposite helicity elliptical normal modes along with the TE and TM modes. With kind permission from Springer Science and Business: ref. [3] Fig. 6.11

oriented polarization states is ascribed to differences in grating coupling strengths in the waveguide, which are not accounted for in the theoretical model. Also, the model does not consider any feeder waveguide like in the experiment.

5.5 Bloch mode reconfiguration

Section 5.1 showed theoretically that magnetic field reversal in a gyrotropy activated MO waveguide structure reverses the helicity of the elliptical normal modes of the structure.

This affects the Bloch mode in the MPCs. The new Bloch mode upon magnetization reversal is given by the following equation:

$$E(z,t) = \hat{e}_{+}^{r,f} E_{01} \exp(i\omega n_{+}^{f}(z-z_n)/c) + \hat{e}_{+}^{r,b} E_{02} \exp(-i\omega n_{+}^{b}(z-z_n)/c)... \\ \hat{e}_{-}^{r,f} E_{03} \exp(i\omega n_{-}^{f}(z-z_n)/c) + \hat{e}_{-}^{r,b} E_{04} \exp(-i\omega n_{-}^{b}(z-z_n)/c), \quad (5.17)$$

Eq. (5.17) shows that upon magnetization reversal, the conjugate helicity modes $\hat{e}_{\pm}^{r,f,b}$ of the previous normal modes $\hat{e}_{\pm}^{f,b}$ take part in propagating a wave through the crystal structure.

This theoretical finding is tested by calculating transmittance spectra for a horizontally oriented elliptical normal mode. The normal mode is launched into the stack layers described in section 5.1 and the transmittance spectrum is calculated for different longitudinal magnetization directions. The theoretical plot in Figure 5.15(a) shows that transmittance spectra are slightly different from each other for different magnetizations of the structure. This difference in the transmittance spectrum of the elliptically polarized normal mode is attributed as the effect of the Bloch mode reconfiguration in MPCs

Experimentally, the effect of the Bloch mode reconfiguration on stop band restructuring is also tested by launching a horizontal elliptical normal mode to MPCs, which are ~$10\mu m$

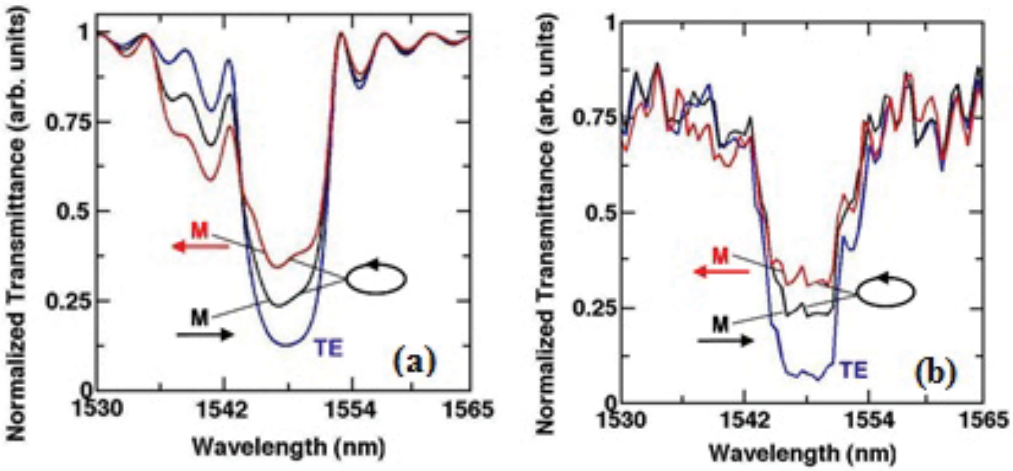

Figure 5.15 (a) The theoretical Bloch mode reconfiguration is tested by calculating a forward fundamental to second order-mode reflected stop band for a horizontal elliptical mode for two directions of a longitudinal magnetic field. Similarly (b) in experiment reconfiguration is tested for the same stop band by a normal mode and its conjugate helicity mode for a photonic crystal 10 μm away from the input side on the waveguide. With kind permission from Springer Science and Business: ref. [3] Fig. 6.11

away from the ridge waveguide input facet. The position of MPCs structure is chosen so that the effect of the mode hybridization in the feeder section is eliminated. The input normal mode for the transmittance spectrum measurement is identical with the theoretical normal mode. The transmittance spectrum of the normal mode for the forward and the backward pointing magnetization is shown in Figure 5.15(b). It is worth mentioning here that only in the forward direction of magnetization, the input mode has its normal mode character; otherwise, it does not. Figure 5.15(b) shows that the transmittance spectra for two different directions of magnetizations are spectrally different, as they are in theory. It confirms the Bloch mode reconfiguration in the MPCs upon magnetization reversal.

Chapter 6

Conclusion and Future Work

This dissertation documents the work performed on magnetic garnet films grown by liquid-phase epitaxy, either by the reduction of their thickness to ultra-thin dimensions, or by patterning them to ridge waveguide structure incorporating photonic crystals (PCs). Geometrical changes to such films lead to new fundamental understandings about their magneto-optic behavior. These new understandings can be applied to non-reciprocal and spintronic based devices to enhance their performance. This chapter discusses key findings about the work presented in chapter 4 and chapter 5 and the possible directions of future research.

6.1 Conclusion

The key finding from the Faraday rotation and transmission measurements is that the specific Faraday rotation increases monotonically as the $Bi_{0.8}Gd_{0.2}Lu_2Fe_5O_{12}$ film thickness is reduced below ~100 nm. Enhancement in circular dichroism and absorbance over a broad wavelength range in the ultra-violet and visible regimes are observed in the ultra-thin films. Experimental findings indicate that these effects and the corresponding enhancement in magneto-optic response in sub-100 nm LPE garnet films are linked to longer-lived electronic excitation in the diamagnetic transitions and modifications in the Bi-O vibrational frequencies, possibly due to surface effects. These enhanced-response thin magneto-optic films may find potential application in devices like optical circulators and optical isolators.

Magneto-optic study on the PCs incorporated ridge waveguide structure fabricated from the same $Bi_{0.8}Gd_{0.2}Lu_2Fe_5O_{12}$ film highlights that there can be magnetic and optical control on the transmittance from such film. The magnetization reversal induces a change in the optical transmission from PCs structure, and this change is caused by the transmutation of the normal into a non-normal mode in the waveguide structure upon magnetization reversal.

6.2 Future Works

Fundamental studies of (1) the role of surface to volume effects and quantum confinement, (2) the role of surface reconstruction in these phenomena, and (3) the role of free surfaces and interfacial effects near the film-substrate interface in boosting the magneto-optic response in iron garnet films are proposed for future work. The primary aim of these studies would be to identify and characterize the physical mechanism(s) responsible for the observed monotonic increase in specific Faraday rotation in sub-100 nm-thick films and a corresponding monotonic change in their magnetic circular dichroism (MCD).

The specific research approach will use to investigate these questions consists of the following:

1) **Photoluminescence.** The purpose of these experiments will be to investigate changes in linewidth with film-thickness of the electronic transitions responsible for the Faraday rotation. Prior investigations provide indirect evidence that the linewidth of these transitions changes in ultra-thin films relative to thicker films. Evidence for these changes is based on fitting theoretical models to magnetic circular dichroism data. By conducting a photoluminescence study, direct evidence of this effect may be obtained. Such a study will verify and provide detailed information about the excited-state lifetime in these oxides. These data will be correlated with surface reconstruction studies on the same samples in order to understand the role of the surface in these phenomena.

2) **Investigation of quantum confinement and surface to volume effects** through a study of magnetic garnet films at the nanoscale. Here it is suggested to study Faraday rotation, MCD, and low-temperature photoluminescence in films thinner than the 19 nm-thick and above studied so far. This study will seek to further eliminate bulk effects and isolate two-dimensional contributions to the Faraday rotation in these films.

3) **Study of surface reconstruction in these magnetic garnet films through TEM and AFM.** These studies will be supplemented by X-ray diffraction analysis and compared with known bulk crystallographic structures.

4) **The effect of crystallographic orientation on Faraday rotation at the nanoscale** will be investigated by comparing the Faraday rotation, MCD, and micro-Raman response in (100) and (111)-oriented films. These experiments will shed further light on the effect of surface reconstruction on the magneto-optic response.

6) **Absorption**. These tests will provide information on the electronic transition processes responsible for the Faraday rotation.

Reference List

1. Levy, M., et al., *Large magneto-optic enhancement in ultra-thin liquid-phase-epitaxy iron garnet films.* Applied Physics Letters, 2015. **107**(1): p. 011104.
2. Chakravarty, A., et al., *Elliptical normal modes and stop band reconfiguration in multimode birefringent one-dimensional magnetophotonic crystals.* Physical Review B, 2011. **84**(9): p. 094202.
3. Levy, M., et al., *Magneto-Photonic Bragg Waveguides, Waveguide Arrays and Non-reciprocal Bloch Oscillations*, in *Magnetophotonics*. 2013, Springer. p. 135-161.
4. Dissanayake, N.K., et al., *Gyrotropic band gap optical sensors.* Applied Physics Letters, 2010. **96**(18): p. 181105.
5. Wu, Z., et al., *Gyrotropic photonic crystal waveguide switches.* Applied Physics Letters, 2010. **96**(5): p. 051125.
6. Shoji, Y., et al., *Magneto-optical isolator with silicon waveguides fabricated by direct bonding.* Applied Physics Letters, 2008. **92**(7): p. 071117.
7. Rachford, F., et al., *Magnetization and FMR studies of crystal-ion-sliced narrow linewidth gallium-doped yttrium iron garnet.* Journal of Applied Physics, 2000. **87**(9): p. 6253-6255.
8. Geller, S. *Crystal and static magnetic properties of garnets*. in *Proc. of the International School of Physics" Enrico Fermi", Course LXX*. 1978.
9. Zvezdin, A.K. and V.a.c.A. Kotov, *Modern magnetooptics and magnetooptical materials*. 1997: CRC Press.
10. Scott, G.B. . in *Proc. of the International School of Physics" Enrico Fermi", Course LXX*. 1978.
11. Wittekoek, S., et al., *Magneto-optic spectra and the dielectric tensor elements of bismuth-substituted iron garnets at photon energies between 2.2-5.2 eV.* Physical review B, 1975. **12**(7): p. 2777.

12. Sung, S.-Y., X. Qi, and B.J. Stadler, *Integrating yttrium iron garnet onto nongarnet substrates with faster deposition rates and high reliability.* Applied Physics Letters, 2005. **87**(12): p. 121111-121111-3.
13. Dillon, G.F. in *Proc. of the International School of Physics" Enrico Fermi", Course LXX*. 1978.
14. Wemple, S., et al., *Optical properties of epitaxial iron garnet thin films.* Physical Review B, 1974. **9**(5): p. 2134.
15. Fratello, V.J. and R. Wolfe, *Epitaxial garnet films for nonreciprocal magneto-optic devices.* Handbook of Thin Films, 2000. **4**.
16. Ando, K., et al., *Growth-induced optical birefringence in LPE-grown Bi-based iron garnet films.* Japanese Journal of Applied Physics, 1983. **22**(10A): p. L618.
17. Algra, H., J. Robertson, and H. Dötsch, *The incorporation of Ga in LPE-grown La, Ga: YIG films.* Applied physics, 1980. **22**(2): p. 189-191.
18. Eschenfelder, A.H., *Magnetic bubble technology*. Vol. 14. 2012: Springer Science & Business Media.
19. Hansen, P., et al., *Magnetic and magneto-optical properties of bismuth-substituted lutetium iron garnet films.* Physical review B, 1985. **31**(9): p. 5858.
20. Dionne, G.F., *Magneto-Optical Spectra*, in *Magnetic Oxides*. 2009, Springer. p. 355.
21. Allen, G.A. and G.F. Dionne, *Application of permittivity tensor for accurate interpretation of magneto-optical spectra.* Journal of applied physics, 1993. **73**(10): p. 6130-6132.
22. Hansteen, F., et al., *Optical and magnetooptical properties of bismuth and gallium substituted iron garnet films.* Thin Solid Films, 2004. **455**: p. 429-432.
23. Berzhansky, V., et al., *Magneto-optics of nanoscale Bi: YIG films.* Applied optics, 2013. **52**(26): p. 6599-6606.
24. Inoue, M., et al., *Magneto-optical properties of one-dimensional photonic crystals composed of magnetic and dielectric layers.* Journal of applied physics, 1998. **83**(11): p. 6768-6770.

25. Steel, M., M. Levy, and R. Osgood, *Photonic bandgaps with defects and the enhancement of Faraday rotation.* Journal of lightwave technology, 2000. **18**(9): p. 1297.
26. Kahl, S. and A.M. Grishin, *Magneto-optical rotation of a one-dimensional all-garnet photonic crystal in transmission and reflection.* Physical Review B, 2005. **71**(20): p. 205110.
27. Levy, M. and R. Li, *Polarization rotation enhancement and scattering mechanisms in waveguide magnetophotonic crystals.* Applied physics letters, 2006. **89**(12): p. 121113.
28. Fitzpatrick, G.L., et al., *Magneto-optic/eddy current imaging of aging aircraft: A new NDI technique.* Materials Evaluation;(United States), 1993. **51**(12).
29. Schramm Jr, H.F., et al., *Method for marking, capturing and decoding machine-readable matrix symbols using magneto-optic imaging techniques*. 1998, Google Patents.
30. Johansen, T., et al., *Direct observation of the current distribution in thin superconducting strips using magneto-optic imaging.* Physical Review B, 1996. **54**(22): p. 16264.
31. Fumagalli, P., et al., *Quantitative determination of the local Kerr rotation by scanning near-field magneto-optic microscopy.* Applied physics letters, 1998. **72**(22): p. 2803-2805.
32. Michler, P., et al., *A quantum dot single-photon turnstile device.* Science, 2000. **290**(5500): p. 2282-2285.
33. Hadfield, R.H., *Single-photon detectors for optical quantum information applications.* Nature photonics, 2009. **3**(12): p. 696-705.
34. Sugawara, M., et al., *Recent progress in self-assembled quantum-dot optical devices for optical telecommunication: temperature-insensitive 10 Gb s− 1 directly modulated lasers and 40 Gb s− 1 signal-regenerative amplifiers.* Journal of Physics D: Applied Physics, 2005. **38**(13): p. 2126.

35. Akiyama, T., et al., *Nonlinear gain dynamics in quantum-dot optical amplifiers and its application to optical communication devices.* Quantum Electronics, IEEE Journal of, 2001. **37**(8): p. 1059-1065.
36. Šolc, I., *A new kind of double refracting filter.* Czechoslovak Journal of Physics, 1954. **4**(1): p. 65-66.
37. Yeh, P., *Electromagnetic propagation in birefringent layered media.* JOSA, 1979. **69**(5): p. 742-756.
38. Mekis, A., et al., *High transmission through sharp bends in photonic crystal waveguides.* Physical Review Letters, 1996. **77**(18): p. 3787.
39. Steel, M. and R. Osgood Jr, *Polarization and dispersive properties of elliptical-hole photonic crystal fibers.* Lightwave Technology, Journal of, 2001. **19**(4): p. 495-503.
40. Göppl, M., et al., *Coplanar waveguide resonators for circuit quantum electrodynamics.* Journal of Applied Physics, 2008. **104**(11): p. 113904.
41. Salamon, Z., H.A. Macleod, and G. Tollin, *Coupled plasmon-waveguide resonators: a new spectroscopic tool for probing proteolipid film structure and properties.* Biophysical journal, 1997. **73**(5): p. 2791.
42. Regener, R. and W. Sohler, *Loss in low-finesse Ti: LiNbO3 optical waveguide resonators.* Applied Physics B, 1985. **36**(3): p. 143-147.
43. Hodgkinson, I., *Inorganic chiral optical materials.* Advanced materials, 2001. **13**(12-13): p. 889-897.
44. Macleod, H.A., *Thin-film optical filters*. 2010: CRC Press.
45. Lub, J., et al., *Stable Photopatterned Cholesteric Layers Made by Photoisomerization and Subsequent Photopolymerization for Use as Color Filters in Liquid-Crystal Displays.* Advanced Materials, 2003. **15**(17): p. 1420-1425.
46. Lakhtakia, A., et al., *Sculptured-thin-film spectral holes for optical sensing of fluids.* Optics communications, 2001. **194**(1): p. 33-46.
47. Liu, Y.J., et al., *High-speed optical humidity sensors based on chiral sculptured thin films.* Sensors and Actuators B: Chemical, 2011. **156**(2): p. 593-598.

48. Nozaki, K., et al., *Sub-femtojoule all-optical switching using a photonic-crystal nanocavity.* Nature Photonics, 2010. **4**(7): p. 477-483.
49. Beggs, D.M., et al., *Ultrashort photonic crystal optical switch actuated by a microheater.* Photonics Technology Letters, IEEE, 2009. **21**(1): p. 24-26.
50. Wang, F. and A. Lakhtakia, *Defect modes in multisection helical photonic crystals.* Optics express, 2005. **13**(19): p. 7319-7335.
51. Kim, S., et al., *Highly efficient photonic crystal-based multichannel drop filters of three-port system with reflection feedback.* Optics express, 2004. **12**(22): p. 5518-5525.
52. Song, M.H., et al., *Defect-mode lasing with lowered threshold in a three-layered hetero-cholesteric liquid-crystal structure.* 2006.
53. Schmidtke, J., W. Stille, and H. Finkelmann, *Defect mode emission of a dye doped cholesteric polymer network.* Physical review letters, 2003. **90**(8): p. 083902.
54. Wu, J.H., et al., *Tunable high-Q photonic-bandgap Fabry-Perot resonator.* JOSA B, 2005. **22**(8): p. 1770-1777.
55. McPhail, D., M. Straub, and M. Gu, *Electrical tuning of three-dimensional photonic crystals using polymer dispersed liquid crystals.* Applied Physics Letters, 2005. **86**(5): p. 051103.
56. Kosmidou, E.P., E.E. Kriezis, and T.D. Tsiboukis, *Analysis of tunable photonic crystal devices comprising liquid crystal materials as defects.* Quantum Electronics, IEEE Journal of, 2005. **41**(5): p. 657-665.
57. Figotin, A., Y.A. Godin, and I. Vitebsky, *Two-dimensional tunable photonic crystals.* Physical Review B, 1998. **57**(5): p. 2841.
58. Alagappan, G., et al., *One-dimensional anisotropic photonic crystal with a tunable bandgap.* JOSA B, 2006. **23**(1): p. 159-167.
59. Busch, K. and S. John, *Liquid-crystal photonic-band-gap materials: the tunable electromagnetic vacuum.* Physical Review Letters, 1999. **83**(5): p. 967.

60. Wang, F., A. Lakhtakia, and R. Messier, *On piezoelectric control of the optical response of sculptured thin films.* Journal of Modern Optics, 2003. **50**(2): p. 239-249.
61. Wang, F. and A. Lakhtakia, *Magnetically controllable intra-Brillouin-zone band gaps in one-dimensional helicoidal magnetophotonic crystals.* Physical Review B, 2009. **79**(19): p. 193102.
62. Chen, H., et al., *A simple route to a tunable electromagnetic gateway.* New Journal of Physics, 2009. **11**(8): p. 083012.
63. Xu, C., et al., *Semiconductor-based tunable photonic crystals by means of an external magnetic field.* Physical Review B, 2003. **68**(19): p. 193201.
64. Takeda, H. and K. Yoshino, *Tunable photonic band schemes in two-dimensional photonic crystals composed of copper oxide high-temperature superconductors.* Physical Review B, 2003. **67**(24): p. 245109.
65. Yoshino, K., et al., *Temperature tuning of the stop band in transmission spectra of liquid-crystal infiltrated synthetic opal as tunable photonic crystal.* Applied Physics Letters, 1999. **75**(7): p. 932-934.
66. Park, W. and J.-B. Lee, *Mechanically tunable photonic crystals.* Optics and Photonics News, 2009. **20**(1): p. 40-45.
67. Serebryannikov, A.E. and A. Lakhtakia, *Optical characteristics of a two-dimensional dielectric photonic crystal immersed in a coherent atomic gas.* JOSA B, 2012. **29**(3): p. 328-334.
68. Kahl, S. and A.M. Grishin, *Enhanced Faraday rotation in all-garnet magneto-optical photonic crystal.* Applied Physics Letters, 2004. **84**(9): p. 1438-1440.
69. Levy, M. and A.A. Jalali, *Band structure and Bloch states in birefringent one-dimensional magnetophotonic crystals: an analytical approach.* JOSA B, 2007. **24**(7): p. 1603-1609.
70. Levy, M., et al., *Bandgap formation and selective suppression of Bloch states in birefringent gyrotropic Bragg waveguides.* Optics express, 2008. **16**(17): p. 13421-13430.

71. Jalali, A.A. and M. Levy, *Local normal-mode coupling and energy band splitting in elliptically birefringent one-dimensional magnetophotonic crystals.* JOSA B, 2008. **25**(1): p. 119-125.
72. Stanciu, C., et al., *All-optical magnetic recording with circularly polarized light.* Physical review letters, 2007. **99**(4): p. 047601.
73. Bertaut, F. and F. Forrat, *Structures of ferrimagetic ferrites of rare earths.* Compt. rend, 1956. **242**: p. 382.
74. Geller, S. and M. Gilleo, *The crystal structure and ferrimagnetism of yttrium-iron garnet, Y 3 Fe 2 (FeO 4) 3.* Journal of Physics and Chemistry of Solids, 1957. **3**(1): p. 30-36.
75. Gilleo, M. and S. Geller, *Magnetic and Crystallographic Properties of Substituted Yttrium-Iron Garnet, 3 Y 2 O 3· x M 2 O 3·(5− x) Fe 2 O 3.* Physical Review, 1958. **110**(1): p. 73.
76. Bonnet, M., et al., *Refinement of the structure of yttrium iron garnet (YIG). A case of severe extinction and absorption.* Acta Crystallographica Section B: Structural Crystallography and Crystal Chemistry, 1975. **31**(9): p. 2233-2240.
77. Dionne, G.F., *Simple derivation of four-level permittivity relations for magneto-optical applications.* Journal of applied physics, 2005. **97**(10): p. 10F103.
78. Yariv, A. and P. Yeh, *Optical waves in crystals*. Vol. 10. 1984: Wiley, New York.
79. Kamino, T., et al., *A FIB micro-sampling technique and a site specific TEM specimen preparation method*, in *Introduction to Focused Ion Beams*. 2005, Springer. p. 229-245.
80. Chan, C.C., et al., *Optical studies of the surface effects from the luminescence of single GaN/InGaN nanorod light emitting diodes fabricated on a wafer scale.* Applied Physics Letters, 2013. **102**(11): p. 111906.

Publications & Achievements

Journal

1. Miguel Levy, **A. Chakravarty,** H.-C. Huang, R. M. Osgood, Jr. 'Large magneto-optic enhancement in ultra-thin garnet films'**, Appl. Phys. Lett.** 107, 011104 (2015).
2. **Ashim Chakravarty**, Miguel Levy, Amir A. Jalali, Zhuoyuan Wu, and Alexander M. Merzlikin, 'Elliptical normal modes and stop band reconfiguration in multimode birefringent one-dimensional magnetophotonic crystals', **Phys. Rev. B** 84, 094202 (2011).
3. Neluka Dissanayake, Miguel Levy, **A. Chakravarty**, P. A. Heiden, N. Chen, and V. J. Fratello, 'Magneto-photonic crystal optical sensors with sensitive covers', **Appl. Phys. Lett.** 99, 091112 (2011).

Conference

1. N. Dissanayake, M. Levy, A. Chakravarty, A. A. Jalali, and V. J. Fratello, 'Polarization Rotation Based Optical Sensor in Magneto-Photonic Crystals', Oral presentation, **F2010 symposium MRS**, Boston, November (2010).

Book Chapter

1. Miguel Levy, **Ashim Chakravarty**, Pradeep Kumar and Xiaoyue Huang, 'Magnetophotonic Bragg Waveguides, Waveguide Arrays and Nonreciprocal Bloch Oscillations', Publisher: **Springer** (April 2013).

Appendix 1

Permission for chapter 4

AIP PUBLISHING LLC LICENSE
TERMS AND CONDITIONS

All payments must be made in full to CCC. For payment instructions, please see information listed at the bottom of this form.

License Number	3664930790236
Order Date	Jul 09, 2015
Publisher	AIP Publishing LLC
Publication	Applied Physics Letters
Article Title	Large magneto-optic enhancement in ultra-thin liquid-phase-epitaxy iron garnet films
Author	Miguel Levy,A. Chakravarty,H.-C. Huang, et al.
Online Publication Date	Jul 6, 2015
Volume number	107
Issue number	1
Type of Use	Thesis/Dissertation
Requestor type	Author (original article)
Format	Print and electronic
Portion	Excerpt (> 800 words)
Will you be translating?	No
Title of your thesis / dissertation	Geometry Induced Magneto-Optic Effects in LPE Grown Magnetic Garnet Films
Expected completion date	Aug 2015
Estimated size (number of pages)	120
Total	0.00 USD

Terms and Conditions

AIP Publishing LLC -- Terms and Conditions: Permissions Uses

AIP Publishing LLC ("AIPP"") hereby grants to you the non-exclusive right and license to use and/or distribute the Material according to the use specified in your order, on a one-time basis,

for the specified term, with a maximum distribution equal to the number that you have ordered. Any links or other content accompanying the Material are not the subject of this license.

1. You agree to include the following copyright and permission notice with the reproduction of the Material:"Reprinted with permission from [FULL CITATION]. Copyright [PUBLICATION YEAR], AIP Publishing LLC." For an article, the copyright and permission notice must be printed on the first page of the article or book chapter. For photographs, covers, or tables, the copyright and permission notice may appear with the Material, in a footnote, or in the reference list.
2. If you have licensed reuse of a figure, photograph, cover, or table, it is your responsibility to ensure that the material is original to AIPP and does not contain the copyright of another entity, and that the copyright notice of the figure, photograph, cover, or table does not indicate that it was reprinted by AIPP, with permission, from another source. Under no circumstances does AIPP, purport or intend to grant permission to reuse material to which it does not hold copyright.
3. You may not alter or modify the Material in any manner. You may translate the Material into another language only if you have licensed translation rights. You may not use the Material for promotional purposes. AIPP reserves all rights not specifically granted herein.
4. The foregoing license shall not take effect unless and until AIPP or its agent, Copyright Clearance Center, receives the Payment in accordance with Copyright Clearance Center Billing and Payment Terms and Conditions, which are incorporated herein by reference.
5. AIPP or the Copyright Clearance Center may, within two business days of granting this license, revoke the license for any reason whatsoever, with a full refund payable to you. Should you violate the terms of this license at any time, AIPP, AIP Publishing LLC, or Copyright Clearance Center may revoke the license with no refund to you. Notice of such revocation will be made using the contact information provided by you. Failure to receive such notice will not nullify the revocation.
6. AIPP makes no representations or warranties with respect to the Material. You agree to indemnify and hold harmless AIPP, AIP Publishing LLC, and their officers, directors, employees or agents from and against any and all claims arising out of your use of the Material other than as specifically authorized herein.
7. The permission granted herein is personal to you and is not transferable or assignable without the prior written permission of AIPP. This license may not be amended except in a writing signed by the party to be charged.
8. If purchase orders, acknowledgments or check endorsements are issued on any forms containing terms and conditions which are inconsistent with these provisions, such inconsistent terms and conditions shall be of no force and effect. This document, including the CCC Billing and Payment Terms and Conditions, shall be the entire agreement between the parties relating to the subject matter hereof.

This Agreement shall be governed by and construed in accordance with the laws of the State of New York. Both parties hereby submit to the jurisdiction of the courts of New York County for purposes of resolving any disputes that may arise hereunder.

Questions? customercare@copyright.com or +1-855-239-3415 (toll free in the US) or +1-978-646-2777.

Permission for chapter 5

SPRINGER LICENSE
TERMS AND CONDITIONS

This is a License Agreement between Ashim Chakravarty ("You") and Springer ("Springer") provided by Copyright Clearance Center ("CCC"). The license consists of your order details, the terms and conditions provided by Springer, and the payment terms and conditions.

All payments must be made in full to CCC. For payment instructions, please see information listed at the bottom of this form.

License Number	3677890818803
License date	Jul 28, 2015
Licensed content publisher	Springer
Licensed content publication	Springer eBook
Licensed content title	Magneto-Photonic Bragg Waveguides, Waveguide Arrays and Non-reciprocal Bloch Oscillations
Licensed content author	Miguel Levy
Licensed content date	Jan 1, 2013
Type of Use	Thesis/Dissertation
Portion	Figures
Author of this Springer article	Yes and you are the sole author of the new work
Order reference number	None
Original figure numbers	Figures 6.1, 6.3, 6.8, 6.9, 6.10, 6.11, 6.12
Title of your thesis / dissertation	Geometry Induced Magneto-Optic Effects in LPE Grown Magnetic Garnet Films
Expected completion date	Aug 2015
Estimated size(pages)	120
Total	0.00 USD

Terms and Conditions

Introduction
The publisher for this copyrighted material is Springer Science + Business Media. By clicking "accept" in connection with completing this licensing transaction, you agree that the following terms and conditions apply to this transaction (along with the Billing and Payment terms and conditions established by Copyright Clearance Center, Inc. ("CCC"), at the time that you opened your Rightslink account and that are available at any time athttp://myaccount.copyright.com).

Limited License
With reference to your request to reprint in your thesis material on which Springer Science and Business Media control the copyright, permission is granted, free of charge, for the use indicated in your enquiry.

Licenses are for one-time use only with a maximum distribution equal to the number that you identified in the licensing process.

This License includes use in an electronic form, provided its password protected or on the university's intranet or repository, including UMI (according to the definition at the Sherpa website: http://www.sherpa.ac.uk/romeo/). For any other electronic use, please contact Springer at (permissions.dordrecht@springer.com or permissions.heidelberg@springer.com).

The material can only be used for the purpose of defending your thesis limited to university-use only. If the thesis is going to be published, permission needs to be re-obtained (selecting "book/textbook" as the type of use).

Although Springer holds copyright to the material and is entitled to negotiate on rights, this license is only valid, subject to a courtesy information to the author (address is given with the article/chapter) and provided it concerns original material which does not carry references to other sources (if material in question appears with credit to another source, authorization from that source is required as well).

Permission free of charge on this occasion does not prejudice any rights we might have to charge for reproduction of our copyrighted material in the future.

Altering/Modifying Material: Not Permitted
You may not alter or modify the material in any manner. Abbreviations, additions, deletions and/or any other alterations shall be made only with prior written authorization of the author(s) and/or Springer Science + Business Media. (Please contact Springer at (permissions.dordrecht@springer.com or permissions.heidelberg@springer.com)

Reservation of Rights
Springer Science + Business Media reserves all rights not specifically granted in the combination of (i) the license details provided by you and accepted in the course of this

licensing transaction, (ii) these terms and conditions and (iii) CCC's Billing and Payment terms and conditions.

Copyright Notice:Disclaimer
You must include the following copyright and permission notice in connection with any reproduction of the licensed material: "Springer and the original publisher /journal title, volume, year of publication, page, chapter/article title, name(s) of author(s), figure number(s), original copyright notice) is given to the publication in which the material was originally published, by adding; with kind permission from Springer Science and Business Media"

Warranties: None

Example 1: Springer Science + Business Media makes no representations or warranties with respect to the licensed material.

Example 2: Springer Science + Business Media makes no representations or warranties with respect to the licensed material and adopts on its own behalf the limitations and disclaimers established by CCC on its behalf in its Billing and Payment terms and conditions for this licensing transaction.

Indemnity
You hereby indemnify and agree to hold harmless Springer Science + Business Media and CCC, and their respective officers, directors, employees and agents, from and against any and all claims arising out of your use of the licensed material other than as specifically authorized pursuant to this license.

No Transfer of License
This license is personal to you and may not be sublicensed, assigned, or transferred by you to any other person without Springer Science + Business Media's written permission.

No Amendment Except in Writing
This license may not be amended except in a writing signed by both parties (or, in the case of Springer Science + Business Media, by CCC on Springer Science + Business Media's behalf).

Objection to Contrary Terms
Springer Science + Business Media hereby objects to any terms contained in any purchase order, acknowledgment, check endorsement or other writing prepared by you, which terms are inconsistent with these terms and conditions or CCC's Billing and Payment terms and conditions. These terms and conditions, together with CCC's Billing and Payment terms and conditions (which are incorporated herein), comprise the entire agreement between you and Springer Science + Business Media (and CCC) concerning this licensing transaction. In the event of any conflict between your obligations established by these terms and conditions

and those established by CCC's Billing and Payment terms and conditions, these terms and conditions shall control.

Jurisdiction
All disputes that may arise in connection with this present License, or the breach thereof, shall be settled exclusively by arbitration, to be held in The Netherlands, in accordance with Dutch law, and to be conducted under the Rules of the 'Netherlands Arbitrage Instituut' (Netherlands Institute of Arbitration).***OR:***

All disputes that may arise in connection with this present License, or the breach thereof, shall be settled exclusively by arbitration, to be held in the Federal Republic of Germany, in accordance with German law.

Other terms and conditions:

v1.3

Questions? customercare@copyright.com or +1-855-239-3415 (toll free in the US) or +1-978-646-2777.

Permission for chapter 5

AMERICAN PHYSICAL SOCIETY ORDER DETAILS
Jul 09, 2015
Order Number 501027163
Order date Jul 09, 2015
Licensed content publisher American Physical Society
Licensed content publication Physical Review B
Licensed content title Elliptical normal modes and stop band reconfiguration in multimode birefringent one-dimensional magnetophotonic crystals
Licensed copyright line ©2011 American Physical Society
Licensed content author Ashim Chakravarty et al.
Licensed content date Sep 12, 2011
Volume number 84
Type of Use Thesis/Dissertation
Requestor type Student
Format Print, Electronic
Portion chapter/article
Rights for Main product
Duration of use Life of current/future editions
Creation of copies for the
Disabled no
With minor editing privileges yes
For distribution to Worldwide
In the following language(s) Original language of publication
With incidental promotional use no
The lifetime unit quantity of new product 0 to 499
The requesting person/organization is: First Author in the article
Order reference number None

Title of your thesis /dissertation Geometry Induced Magneto-Optic Effects in LPE Grown Magnetic Garnet Films

Appendix 2

The intensity of polarized light that passes through a polarizer is proportional to the square of the cosine of the angle between the electric field of the polarized light and the angle of the polarization analyzer.

$$I=I_0\text{Cos}^2\theta \tag{A1.1}$$

Now, the electric field amplitude of a monochromatic plane wave of angular frequency ω traveling in the z direction from a polarizer to the analyzer can be described as

$$E = E_0 \,\text{Cos}\left(\omega t - kz + \delta\right), \tag{A1.2}$$

where δ is the phase lag between optical components at any instant of time 't'.

If the analyzer is sitting at z=0, then the electric field amplitude of the wave can be expressed as

$$E = E_0 \,\text{Cos}\left(\omega t + \delta\right). \tag{A1.3}$$

Therefore, Eq. A1.1 also be expressed as

$$E^2 = E_0^2 \,\text{Cos}^2(\omega t + \delta), \tag{A1.4}$$

where $I = E^2$, $I_0 = E_0^2$, and $\omega t + \delta = \theta$.

Eq. A1.1 can be expressed in terms of plane wave form as

$$I = {I_0}/{2} + \left({I_0}/{2}\right)\text{Cos}\,2\theta = {I_0}/{2} + \left({I_0}/{2}\right)\text{Cos}\left[2\left(\omega t + \delta\right)\right]. \tag{A1.5}$$

In summary, the intensity measurement of a plane wave propagating through a polarizer and an analyzer yields frequency doubling of the measured intensity. This measurement also measures double the phase lag between these two optical components.

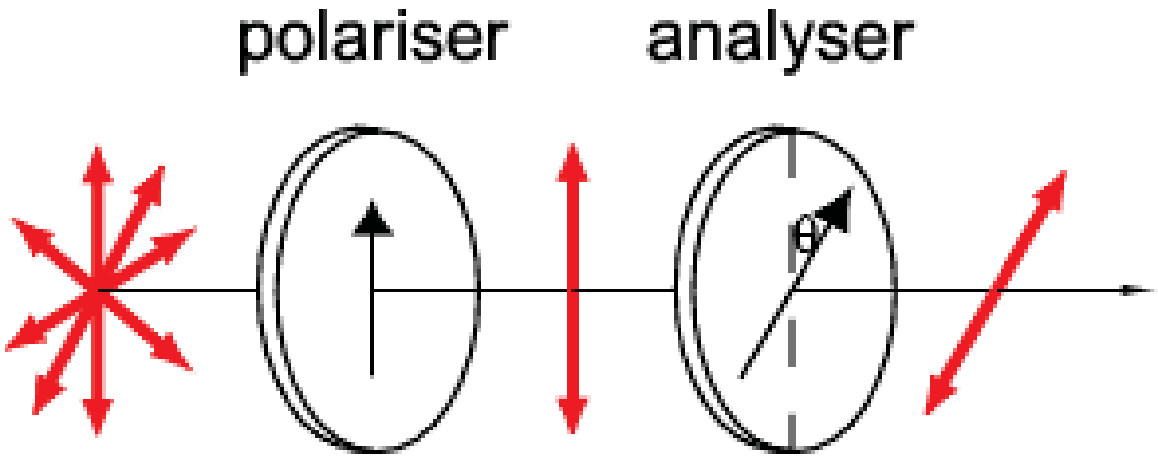

Figure A2.1 Malus's law can be explained using the propagation of a monochromatic plane wave through a polarizer and an analyzer.

Appendix 3

1) Elemental Number Density Method

Film density of the film $Bi_{0.8}Gd_{0.2}Lu_2Fe_5O_{12}$ with GGG substrate used by RBS analysis to determine the composition of the film can be calculated using atomic densities of their constituents. Table 4.1 shows atomic mass, mass density and atomic number density of each element that present in the film and the substrate. Here, Atomic number density of an element can be calculated using the following formula

$$n_s = \frac{N_A d_s}{m_s}$$

where n_s, d_s, and M_s are atomic number density, mass density, and atomic mass of an element respectively. Here, N_A is the Avogadro's constant 6.023×10^{23} mol^{-1}.

Table A3-1: Number density of different elements of $Bi_{0.8}Gd_{0.2}Lu_2Fe_5O_{12}$ film and $Gd_3Ga_5O_{12}$

Elements	Bi	Gd	Ga	Lu	Fe	O
Atomic mass, M_s (u)	208.98	157.25	69.723	174.96	55.84	15.99
Density, d_s (g/cm^3)	9.78	7.90	5.91	9.84	7.87	1.49
n_s ($\times10^{22}$ $atoms/cm^3$)	2.81	3.02	5.11	3.38	8.49	5.63

Therefore, atomic number density of the $Bi_{0.8}Gd_{0.2}Lu_2Fe_5O_{12}$ film and $Gd_3Ga_5O_{12}$ substrate is calculated as

$$n_{film} = \frac{1}{20}[0.8n_{\mathrm{Bi}} + 0.2n_{\mathrm{Gd}} + 2n_{\mathrm{Lu}} + 5n_{\mathrm{Fe}} + 12n_{\mathrm{O}}] = 5.8721 \times 10^{22}\mathrm{atoms/cm^3}$$

$$n_{Sub} = \tfrac{1}{20}[3n_{\mathrm{Gd}} + 5n_{\mathrm{Ga}} + 12n_{\mathrm{O}}] = 5.1072 \times 10^{22}\mathrm{atoms/cm^3}\ .$$

Now, if a film with composition $Bi_{0.4}Gd_{1.6}Lu_{1.0}Fe_{2.5}Ga_{2.5}O_{12}$ is sandwiched between the $Bi_{0.8}Gd_{0.2}Lu_2Fe_5O_{12}$ film and $Gd_3Ga_5O_{12}$ substrate, then the atomic number density of such interfacial film is

$$n_{ifilm} = \frac{1}{20}[0.4n_{\mathrm{Bi}} + 1.6n_{\mathrm{Gd}} + 1.0n_{\mathrm{Lu}} + 2.5n_{\mathrm{Fe}} + 2.5n_{\mathrm{Ga}} + 12n_{\mathrm{O}}] = 5.5448 \times 10^{22}\mathrm{atoms/cm^3}.$$

Since the GGG's mass density is known to be as $7.08\mathrm{g/cm^3}$, hence the atomic number density of GGG also can be calculated using average mass calculation method. Average mass of GGG is

$$M_{GGG} = \tfrac{1}{20}[3 \times M_{\mathrm{Gd}} + 5 \times M_{\mathrm{Ga}} + 12 \times M_0] = 50.618\ u\ .$$

Hence, the atomic number density of GGG is calculated as

$$n_{GGG} = \frac{6.023 \times 10^{23} \times 7.08}{50.618}\mathrm{atoms/cm^3} = 8.4244 \times 10^{22}\mathrm{atoms/cm^3}.$$

It can be seen later that this number density value of GGG matches the number density value coming from the unit cell method.

2) Unit Cell Method

Most of the magnetic garnet films and the GGG substrate belong to the Ia3d space group and therefore they have cubic crystal structure. A crystal structure belong to such space group has 160 atoms in the unit cell. Hence, the atomic number density of the garnets can be calculated easily provided the lattice constant of the unit cell is known. Table 4.2 shows lattice constants of different garnet films and the GGG substrate. In the table, third row

calculates the atomic number density of different garnets by taking account the number of atoms in the garnet unit cell.

Table A3-2: Atomic number density of magnetic garnets calculated from the lattice constant.

Garnets	YIG	BIG	LuIG	GdIG	GGG	YGG
Lattice constant (nm)	1.2367	1.2621	1.2283	1.2471	1.2383	1.2274
Unit Cell Volume (nm^3)	1.8914	2.0104	1.8532	1.9396	1.8988	1.8491
Offset from YIG cell volume (nm^3)	0	0.119	-0.0382	0.0482	0.0074	-0.0423
No. of unit cells ($\times 10^{20}$per cm^3)	5.2869	4.9741	5.3961	5.1557	5.2665	5.5408
Atomic number density ($\times 10^{22}$atoms/cm^3)	8.4592	7.9586	8.6338	8.2491	8.4264	8.6528

Now, using Table 4.2 and the atomic composition of a garnet unit cell, cell volume of the $Bi_{0.8}Gd_{0.2}Lu_2Fe_5O_{12}$ film is calculated here. The unit cell volume and the atomic number density of the $Bi_{0.8}Gd_{0.2}Lu_2Fe_5O_{12}$ film are calculated as

$$U_V = 1.8914 + \frac{1}{24}[6 \times U_{\text{BIG-YIG}} + 2 \times U_{\text{GdIG-YIG}} + 16 \times U_{\text{LuIG-YIG}}] = 1.8997 \text{ nm}^3$$

$$n_{film} = 8.4225 \times 10^{22} \text{atoms/cm}^3.$$

Similarly, unit cell volume of $Bi_{0.4}Gd_{1.6}Lu_{1.0}Fe_{2.5}Ga_{2.5}O_{12}$ interfacial film and its atomic number density are given by

$$U_V = 1.8914 + \frac{1}{24}[3 \times U_{\text{BIG-YIG}} + 13 \times U_{\text{GdIG-YIG}} + 8 \times U_{\text{LuIG-YIG}}] + \frac{1}{40}[20 \times U_{\text{YGG-YIG}}] = 1.8985\ \text{nm}^3.$$

$$n_{ifilm} = 8.4277 \times 10^{22} \text{atoms/cm}^3.$$

Appendix 4

MATLAB Code for Transmittance Spectra Calculation

```
%Transmission1
clc, clear all
format long

fprintf('ENTER 1 IF APPLIED MAGNETIC FIELD IS FORWARD\n')
fprintf('ENTER 2 IF APPLIED MAGNETIC FIELD IS BACKWARD\n')
fprintf('ENTER 3 IF APPLIED MAGNETIC FIELD IS TRANSVERSE\n\n')
M=input('FIELD = ');
fprintf('\n')

if M==3
     F=0; wl=0; g=F;
    else
F=input('Faraday rotation from the sample (in degree/mm)= ');
wl=input('Wavelength Faraday rotation measured at (in nm)= ');
fprintf('\n')
end

% Defining Refractive Indicies for LAYER 1 & 2
% LAYER 1
fprintf('FORWARD & BACKWARD PROPAGATING MODE IN LAYER 1\n')
disp('Enter the refractive indices for forward mode')
n1f_xx=input('n1f_xx= ');
n1f_yy=input('n1f_yy= ');
disp('Enter the refractive indices for backward mode')
n1b_xx=input('n1b_xx= ');
n1b_yy=input('n1b_yy= ');

% LAYER 2
fprintf('\n')
fprintf('FORWARD & BACKWARD PROPAGATING MODE IN LAYER 2\n')
disp('Enter the refractive indices for forward mode')
n2f_xx=input('n2f_xx= ');
n2f_yy=input('n2f_yy= ');
disp('Enter the refractive indices for backward mode')
n2b_xx=input('n2b_xx= ');
n2b_yy=input('n2b_yy= ');

if M==1
    g=F;
elseif M==2
    g=-F;
end
% Defining Permittivity Tensors for LAYER 1 & 2
% LAYER 1 Forward mode
e1f=zeros(2,2);
```

```
e1f(1,1)=(n1f_xx)^2;
e1f(2,2)=(n1f_yy)^2;
e1f_xy=((n1f_xx+n1f_yy)/2)*(g/180)*wl*10^(-6);
e1f(1,2)=1i*e1f_xy;
e1f(2,1)=-1i*e1f_xy;
% Backward mode
e1b=zeros(2,2);
e1b(1,1)=(n1b_xx)^2;
e1b(2,2)=(n1b_yy)^2;
e1b_xy=((n1b_xx+n1b_yy)/2)*(g/180)*wl*10^(-6);
e1b(1,2)=1i*e1b_xy;
e1b(2,1)=-1i*e1b_xy;

% LAYER 2 Forward mode
e2f=zeros(2,2);
e2f(1,1)=(n2f_xx)^2;
e2f(2,2)=(n2f_yy)^2;
e2f_xy=((n2f_xx+n2f_yy)/2)*(g/180)*wl*10^(-6);
e2f(1,2)=1i*e2f_xy;
e2f(2,1)=-1i*e2f_xy;
% Backward mode
e2b=zeros(2,2);
e2b(1,1)=(n2b_xx)^2;
e2b(2,2)=(n2b_yy)^2;
e2b_xy=((n2b_xx+n2b_yy)/2)*(g/180)*wl*10^(-6);
e2b(1,2)=1i*e2b_xy;
e2b(2,1)=-1i*e2b_xy;

% Displaying Permittivity Tensors for LAYER 1 & 2
% LAYER 1
fprintf('\n')
fprintf('Permittivity tensor Forward mode in layer 1\n\n')
disp(e1f)
fprintf('Permittivity tensor Backward mode in layer 1\n\n')
disp(e1b)

% LAYER 2
fprintf('\n')
fprintf('Permittivity tensor Forward mode in layer 2\n\n')
disp(e2f)
fprintf('\n')
fprintf('Permittivity tensor Forward mode in layer 2\n\n')
disp(e2b)

% Defining Birefringence dependent Refractive Indices
% n+,n- & alpha parameter for LAYER 1 & 2
% LAYER 1 Forward mode
e1f_bar=(e1f(1,1)+e1f(2,2))/2;
delta1f=(e1f(2,2)-e1f(1,1))/2;
gamma1f=sqrt(delta1f^2+e1f_xy^2);
n1fp=sqrt(e1f_bar+gamma1f);
n1fm=sqrt(e1f_bar-gamma1f);
alpha1f=0.5*acos(e1f_xy/gamma1f);
% Backward mode
```

```
e1b_bar=(e1b(1,1)+e1b(2,2))/2;
delta1b=(e1b(2,2)-e1b(1,1))/2;
gamma1b=sqrt(delta1b^2+e1b_xy^2);
n1bp=sqrt(e1b_bar+gamma1b);
n1bm=sqrt(e1b_bar-gamma1b);
alpha1b=0.5*acos(e1b_xy/gamma1b);

% LAYER 2 Forward mode
e2f_bar=(e2f(1,1)+e2f(2,2))/2;
delta2f=(e2f(2,2)-e2f(1,1))/2;
gamma2f=sqrt(delta2f^2+e2f_xy^2);
n2fp=sqrt(e2f_bar+gamma2f);
n2fm=sqrt(e2f_bar-gamma2f);
alpha2f=0.5*acos(e2f_xy/gamma2f);
% Backward mode
e2b_bar=(e2b(1,1)+e2b(2,2))/2;
delta2b=(e2b(2,2)-e2b(1,1))/2;
gamma2b=sqrt(delta2b^2+e2b_xy^2);
n2bp=sqrt(e2b_bar+gamma2b);
n2bm=sqrt(e2b_bar-gamma2b);
alpha2b=0.5*acos(e2b_xy/gamma2b);

% Storing Datas to files
alpha=[alpha1f; alpha1b; alpha2f; alpha2b];
nref=[n1fp; n1fm; n1bp; n1bm; n2fp; n2fm; n2bp; n2bm];
save TmatrixRIdata.txt nref -ascii -double
save TmatrixAlphadata.txt alpha -ascii -double

fprintf('1ST PART FOR TRANSMITTANCE SPECTRUM IS COMPLETED.\n\n')
fprintf('NEXT, RUN PROGRAM Transmission2 FROM DIRECTORY.\n\n')
```

```
% Transmission2
clc, clear all
format long

% Reading data file from Transmission1
nr=load('TmatrixRIdata.txt');
al=load('TmatrixAlphadata.txt');

% Crystal Parameters
p=input('CRYSTAL PERIOD(in nm)=');
fprintf('\n')
fprintf('LAYER1+LAYER2=1UNIT CELL\n')
fprintf('Total number of unit cells light will pass\n')
n=input('through (Enter integer value)=');
fprintf('\n')
fprintf('FROM PERIOD\n')
d=input('layer 1 covers (in percentage)=');
dn=100-d;
fprintf('Layer 2 covers %3.2f percent.\n\n',dn)
% Entering input wavelength interval
fprintf('WAVELENGTH RANGE FOR TRANSMITTANCE SPECTRUM\n')
wlF=input('Starting Wavelength(in nm)=');
```

```
l=input('Wavelength Increment(in nm)=');
wlL=input('Final Wavelength(in nm)=');
R=wlF:l:wlL;
wl=R.^-1;
m=length(wl);
save Wavelengthcount.txt m -ascii
fprintf('\n')

% Defining Dynamical matrices for Layer 1 & 2
% Layer 1
al1=[cos(al(1)); cos(al(2)); sin(al(1)); sin(al(2))];
D1=zeros(4,4);
% 1st Row
D1(1,1)=al1(1); D1(1,2)=al1(2);
D1(1,3)=-al1(3); D1(1,4)=-al1(4);
% 2nd Row
D1(2,1)=nr(1)*al1(1); D1(2,2)=-nr(3)*al1(2);
D1(2,3)=-nr(2)*al1(3); D1(2,4)=nr(4)*al1(4);
% 3rd Row
D1(3,1)=al1(3); D1(3,2)=al1(4);
D1(3,3)=al1(1); D1(3,4)=al1(2);
% 4th Row
D1(4,1)=nr(1)*al1(3); D1(4,2)=-nr(3)*al1(4);
D1(4,3)=nr(2)*al1(1); D1(4,4)=-nr(4)*al1(2);

% Layer 2
al2=[cos(al(3)); cos(al(4)); sin(al(3)); sin(al(4))];
D2=zeros(4,4);
% 1st Row
D2(1,1)=al2(1); D2(1,2)=al2(2);
D2(1,3)=-al2(3); D2(1,4)=-al2(4);
% 2nd Row
D2(2,1)=nr(5)*al2(1); D2(2,2)=-nr(7)*al2(2);
D2(2,3)=-nr(6)*al2(3); D2(2,4)=nr(8)*al2(4);
% 3rd Row
D2(3,1)=al2(3); D2(3,2)=al2(4);
D2(3,3)=al2(1); D2(3,4)=al2(2);
% 4th Row
D2(4,1)=nr(5)*al2(3); D2(4,2)=-nr(7)*al2(4);
D2(4,3)=nr(6)*al2(1); D2(4,4)=-nr(8)*al2(2);

% Product of inv(D1) & D2 and inv(D2) & D1
D1_2=D1\D2;
D2_1=D2\D1;

% Defining ellipticity and polarization angle
% input light in Cartesian
fprintf('ENTER INPUT LIGHT INFO\n')
z_1=input('X component of light=');
z_2=input('Y component of light=');

fprintf('\n')
fprintf('IN CARTESIAN CO-ORDINATE INPUT LIGHT IS\n')
z=[z_1; z_2];
```

```
disp(z)

% Cartesian to Elliptical
A=1/sqrt(2)*[(al1(1)+al1(3)) (al1(1)-al1(3)); 1i*((al1(1)-al1(3)))...
     -1i*(al1(1)+al1(3))];
L=A\z;
% Ei(1) and Ei(3) input Fields
Ei(1,1)=L(1);
Ei(2,1)=1i*L(2);
fprintf('\n')
fprintf('IN ELLIPTICAL CO-ORDINATE INPUT LIGHT IS\n')
disp('z=')
disp(Ei)

% Transfer Matrix Calculation
opt=fopen('TOutput.txt','w');
for k=1:m
% Propagation Matrices for layer 1 & 2
nd1=2*pi*p*wl(k)*(d/100)*1i*[nr(1); -nr(3); nr(2); -nr(4)];
nd2=2*pi*p*wl(k)*(dn/100)*1i*[nr(5); -nr(7); nr(6); -nr(8)];
% Layer 1
Pr1=zeros(4,4);
Pr1(1,1)=exp(nd1(1)); Pr1(2,2)=exp(nd1(2));
Pr1(3,3)=exp(nd1(3)); Pr1(4,4)=exp(nd1(4));
% Layer 2
Pr2=zeros(4,4);
Pr2(1,1)=exp(nd2(1)); Pr2(2,2)=exp(nd2(2));
Pr2(3,3)=exp(nd2(3)); Pr2(4,4)=exp(nd2(4));

Pr_1=Pr1;
Pr_2=Pr2;

% Transfer Matrix
T1=Pr_1*D1_2;
T2=Pr_2*D2_1;
T=T1*T2;
Tn=T^n;
% Dividing Transfer matrix into 4 column matrices
J1=Tn(:,1); J2=Tn(:,2); J3=Tn(:,3); J4=Tn(:,4);

% Calculation of Transmitted light
S21=J1(2); S22=J2(2); S23=J3(2); S24=J4(2);
S41=J1(4); S42=J2(4); S43=J3(4); S44=J4(4);
S02=-[S21 S23; S41 S43];
EI=[Ei(1,1); Ei(2,1)];
S2=S02*EI;
S4=[S22 S24; S42 S44];
ER=S4\S2;

% Transmitted Field
S11=J1(1); S12=J2(1); S13=J3(1); S14=J4(1);
S31=J1(3); S32=J2(3); S33=J3(3); S34=J4(3);
S1=[S11 S13; S31 S33]; S3=[S12 S14; S32 S34];
ET=S1*EI+S3*ER;
```

```
% Saving into files
fprintf(opt,'%g\t %2.16f\t %2.16f\t %2.16f\t %2.16f\n',...
    R(k),real(ET(1)),imag(ET(1)), real(ET(2)),imag(ET(2)));
end
fclose(opt);

fprintf('\n')
fprintf('2ND PART FOR TRANSMITTANCE SPECTRUM IS COMPLETED.\n\n')
fprintf('NEXT, RUN PROGRAM Transmission3 FROM DIRECTORY.\n\n')
```

```
%Transmission3
clc, clear all
format long

% Reading Data generated by program Transmission2
ipt=fopen('TOutput.txt','r');
m=load('Wavelengthcount.txt');

M=zeros(m,5);
for k=1:m
M(k,:)=fscanf(ipt,'%f',5);
end
fclose(ipt);

% Reading wavelength range
wl=M(:,1);

% Transmitted Field
% ET(1) Field
Et11=M(:,2);
Et12=1i*M(:,3);
% ET(3) Field
Et31=1i*M(:,5);
Et32=M(:,4);

% Transmittance Initialization
T11=zeros(m,1);
T13=zeros(m,1);
T33=zeros(m,1);
T=zeros(m,1);
for j=1:m
ET1=([Et11(j,1); Et12(j,1)]);
ET3=([Et31(j,1); Et32(j,1)]);
T11(j,:)=ET1'*ET1;
T13(j,:)=abs(ET1'*ET3);
T33(j,:)=ET3'*ET3;
T(j,:)=ET1'*ET1+ET3'*ET3;
end

plot(wl,T,'-b','linewidth',3)
```